Passive Microwave Remote Sensing of Snow Layers Using Novel Wideband Radiometer Systems and RFI Mitigation

by

Maryam Salim

A dissertation submitted in partial fulfillment
of the requirements for the degree of
Doctor of Philosophy
(Electrical and Computer Engineering)
in The University of Michigan
2021

Doctoral Committee:

Associate Research Scientist Dr. Roger D. De Roo, Co-Chair
Professor Kamal Sarabandi, Co-Chair
Professor Anthony W. England
Associate Professor Mark Flanner
Professor Joel T. Johnson, The Ohio State University
Associate Research Scientist Dr. Adib Nashashibi

Maryam Salim

maryamsa@umich.edu

ORCID iD: 0000-0002-0180-6255

Dedicated to my beloved mother

And

In the memory of my grandfather, who instilled the love of science in me and was always encouraging with his unwavering faith in me...

ACKNOWLEDGEMENTS

It would not be possible to write this dissertation without the help and support of several kind people all the way, only some of whom it is possible to acknowledge here.

Firstly, I would like to express my deep and sincere gratitude to my supervisors Prof. Kamal Sarabandi and Dr. Roger De Roo for their invaluable encouragement, care, patience, guidance, and for providing me with an excellent atmosphere to conduct research and learn several skills throughout my Ph.D. studies. I would also like to thank the National Aeronautics and Space Administration (NASA) for funding this project.

I am deeply grateful for my thesis committee members; Prof. Anthony England, Prof. Mark Flanner, Prof. Joel T. Johnson, and Dr. Adib Nashashibi, for the collaborations we had, and their valuable comments to improve the thesis.

I would like to take this opportunity to express my heartfelt gratitude to Ms. Angela Farrehi for all her emotional support, help, and for being the great source of motivation and encouragement throughout this journey.

I would like to thank the associate dean for academic affairs, Prof. Michael Wellman, and chair of ECE graduate affairs, Prof. Heath Hofmann for their valuable support in

my Ph.D. studies. I would also like to thank all the ECE staff, especially Ms. Anne Rhoades, Ms. Kristen Thornton, and Mr. Jose-Antonio Rubio for their kindness and their ability to lift my spirit in the ups and downs of Ph.D. journey.

I would like to extend my gratitude to all current and former radiation laboratory (Radlab) and space research laboratory (SPRL) colleagues, especially, Dr. Amr Ebrahim, Dr. Line Van Nieuwstadt, Dr. Behzad Yektakhah, and Dr. Mohammad Mousavi for the insightful technical discussions during my PhD studies.

I would also want to thank all my teachers from my early stages at school till my undergraduate and graduate years. I want to especially thank Dr. Majid Nemati, Dr. Ali Pourziad, Dr. Ahmadali Ashrafian, and Prof. Levent Gurel for making electromagnetics enjoyable for me and always being great mentors.

Many thanks to all my old and new friends, especially Dr. Mahsa Ebrahimpouri, Dr. Mehrzad Samadi, Dr. Alireza Sadeghi, Mr. Sina Abedini, Ms. Negin Musavi, Dr. Omar Abdelatty, Ms. Yasaman Esfahlani, Dr. Farshad Harirchi, Ms. Shiva Sheikhalipour, Ms. Nazanin Jafari, Mr. Mohammad Mobayen, Mr. Iman Deznabi, Ms. Nooshin Faramarzi, Mr. Dariush Kari, and Dr. Rajeswari Balasubramaniam, for always being there for me and being the major source of support during recent years that I have been thousands of miles away from my family.

Finally, I would like to express my deepest gratitude to my beloved family, my mom Fatemeh, my auntie Somra, my sisters Niloufar and Mina, and my beautiful niece Melika for their unconditional love, unwavering support and for putting up with my absence during these years.

TABLE OF CONTENTS

LIST OF FIGURES

Figure

LIST OF TABLES

Table

LIST OF ABBREVIATIONS

ACF autocorrelation function

ADS advanced design system

AMSR2 advanced microwave scanning radiometer-2

BRDF bidirectional refection distribution functions

DBA distorted Born approximation

ENBW equivalent noise bandwidth

FD-WiBAR frequency domain wideband autocorrelation radiometry

FPGA field-programmable gate array

FPI Fabry-Perot interferometer

FSR free spectral range

ICA infinite cylinder approximation

InSAR interferometric synthetic aperture radar

KRC Keweenaw research center

LNA low noise amplifier

NISAR NASA-ISROSynthetic aperture radar

NMM3D numerical Maxwell model of 3D

PALS passive and active L-band Sensor

Radlab radiation laboratory

RF radio frequency

RFI radio frequency interference

RTE radiative transfer equations

SMAP soil moisture active and passive

SMAPVEX12 SMAP Validation Experiment 2012

SMOS soil moisture and ocean salinity

SNR signal to noise ratio

SPRL space research laboratory

SWE snow water equivalent

TDA thin disk approximation

TD-WiBAR time domain wideband autocorrelation radiometry

UWBRAD ultra-wideband software-defined radiometer

VWC vegetation water content

WiBAR wideband autocorrelation radiometry

ABSTRACT

Climate change can reduce the availability of water resources in many regions, and it will affect agriculture, industry, and energy supply. Snowpack monitoring is important in water resource management as well as flood and avalanche protection. The rapid melting process due to global warming changes the snowpacks' annual statistics, including the extent, and the snow water equivalent (SWE) of seasonal snowpacks, which results in non-stationary annual statistics that should be monitored in nearly daily intervals.

The development of advanced radiometric sensors capable of accurately measuring the snowpack thickness and SWE is needed for the long-term study of the snowpack parameters' statistical changes. Passive microwave radiometry provides a means for measuring the microwave emission from a scene of snow and ice. A Wideband Autocorrelation Radiometer (WiBAR) operating from 1-2 GHz measures spontaneous emission from snowpack at long wavelengths where the scattering is minimized, but the snow layer coherent effects are preserved. By using a wide bandwidth to measure the spacing between frequencies of constructive and destructive interference of the emission from the soil under the snow, it can reveal the microwave travel time through the snow, and thus the snow depth.

However, narrowband radio frequency interference (RFI) in the WiBAR's frequency of operations reduces the ability of the WiBAR to measure the thickness accurately. In addition, the current WiBAR system is a frequency domain, FD-WiBAR, system that uses a field-portable spectrum analyzer to collect the data and suffers from

high data acquisition time which limits its applications for spaceborne and airborne technologies.

In this work, a novel frequency tunable microwave comb filter is proposed for RFI mitigation. The frequency response of the proposed filter has a pattern with many frequencies band-pass and band rejection that preserves the frequency span while reducing the RFI. Moreover, we demonstrate time-domain WiBAR, TD-WiBAR, which presented as an alternative method for FD-WiBAR, and is capable of providing faster data acquisition. A new time-domain calibration is also developed for TD-WiBAR and evaluated with the frequency domain calibration.

To validate the TD-WiBAR method, simulated laboratory measurements are performed using a microwave scene simulator circuit. Then the WiBAR instrument is enhanced with the proposed comb filter and showed the RFI mitigation in time-domain mode on an instrument bench test.

Furthermore, we analyze the effects of an above snow vegetation layer on brightness temperature spectra, particularly the possible decay of wave coherence arising from volume scattering in the vegetation canopy. In our analysis, the snow layer is assumed to be flat, and its upward emission and surface reflectivities are modeled by a fully coherent model, while an incoherent radiative transfer model describes the volume scattering from the vegetation layer.

We proposed a unified framework of vegetation scattering using radiative transfer (RT) theory for passive and active remote sensing of vegetated land surfaces, especially those associated with moderate-to-large vegetation water contents (VWCs), e.g., forest field. The framework allows for modeling passive and active microwave signatures of the vegetated field with the same physical parameters describing the vegetation structure. The proposed model is validated with the passive and active L-band sensor (PALS) acquired in SMAPVEX12 measurements in 2012, demonstrating the applicability of this model.

CHAPTER I

Introduction

1.1 Motivation and Objectives

The potential future impacts of climate change are of great interest. Its impacts on ecosystems and it can potentially affect the capacity of natural systems to maintain the existing hydrological cycles and the available water resources on land. It can reduce the availability of water resources in many regions, and it will affect agriculture, industry, and energy supply. Therefore, to improve our predictive capability a systematic observation and analysis of the variables which affect the climate on a global and regional basis are necessary (*Serreze et al.*, 2000; *Waitt et al.*, 1983).

Cryospheric elements like snow cover are an indicator of global warming and play an essential role in providing water supplies for numerous parts of the globe. The rapid melting process due to global warming changes the snowpacks' annual statistics, including extent, and snow water equivalent (SWE) of seasonal snowpack, which results in non-stationary annual statistics that should be monitored in nearly daily intervals. Accurate remote sensing information on SWE and snowpack thickness serve as important markers of the availability of water resources.

Different remote sensing techniques are presented in the literature to estimate the distribution of SWE globally and for specific regions (*Kokhanovsky et al.*, 2005; *Peltoniemi et al.*, 2005; *Kinar and Pomeroy*, 2009).

Ground-based techniques for characterizing snow have been discussed in (*Kokhanovsky et al.*, 2005; *Peltoniemi et al.*, 2005). These techniques include measurements of bidirectional refection distribution functions (BRDF) of snow in specific areas (*Peltoniemi et al.*, 2005), measurements of snow reflections in visible and near-infrared (*Kokhanovsky et al.*, 2005), and techniques for determining SWE by an acoustic pulse based on the idea of sending and receiving acoustic waves into the snow (*Kinar and Pomeroy*, 2009). Snow sensors are buried underneath the snow cover is another technique to characterize SWE (*Milly et al.*, 2008). However, these techniques are limited to specific areas.

Therefore, remotely sensing techniques such as measuring the snowpack's brightness temperature from which the snow thickness and SWE can be retrieve for analyzing the long-term changes of statiscs of the snowpack's properties (*Milly et al.*, 2008). To provide accurate resource monitoring, improvements in methods for remote sensing of snow properties are required.

Satellite remote sensing sensors have the ability to measure SWE over extended areas (*Leinss et al.*, 2015). interferometric synthetic aperture radar (InSAR) techniques are examples of mapping of SWE with high resolution (*Guneriussen et al.*, 2001). Thus, the determination of SWE is then extracted from the measurement of the radar which is a challenging problem. In addition, active sensors, such as radars require high power which makes the instrument very expensive for airborne and space borne.

On the other hand, passive remote sensing sensors, i.e. radiometers, do not include a transmit system, therefore radiometers are more cost-efficient systems than active systems,i.e. radars, for measuring the characteristics of snow and ice layers.

1.2 Microwave Radiometry

Microwave radiometry provides useful observation of the Earth's biosphere, such as atmosphere, ocean, and land surfaces. Passive microwave radiometry with frequencies

between 300 MHz and 30 GHz can have considerable penetration in snow/ice and vegetation layers. Measurements at long wavelengths minimize volume scattering effects, and the sensitivity to the surface roughness within the snowpack. Radiometers at long wavelength can provide information about material's properties, such as its temperature and dielectric properties by measuring the electromagnetic energy radiated by a material (*Mousavi et al.*, 2018).

Conventionally remote sensing measurements of snow water equivalent (SWE) and the snowpack thickness were based on the scatter darkening technique. This method considers the volumetric scattering of the snow grains at high frequencies (19-37 GHz). It relies on observing the snowpack at two different frequencies, with scatter darkening is stronger at the higher frequency. Using empirical formulation, the SWE and snowpack thickness which is specific to the regions are then calculated (*Guneriussen et al.*, 2001; *Tsang et al.*, 2007). Unlike the scatter darkening approach to the passive microwave remote sensing of snow depth which uses algorithms to interpret the data, microwave radiometry is a technique that implements the data acquisition and its post processing processing algorithm by directly measuring the microwave emission from a scene of snow and ice.

Radiometry is carried out in long wavelength range and over a wide frequency band, which minimizes scattering and enhances coherent effects of the slab geometry. This is the primary advantage of radiometry. Such instruments are exemplified by the $0.5-2.0$ GHz ultra-wideband software-defined radiometer (UWBRAD) (*Andrews et al.*, 2018) and the Wideband Autocorrelation Radiometer (WiBAR) *England* (2013). The WiBAR concept has been verified at X-band *Mousavi et al.* (2018) and recently, a new prototype has been built to operate at $1.0-3.0$ GHz.

1.3 Wideband Autocorrelation Radiometer

Wideband autocorrelation radiometry (WiBAR) is a technique wherein the electromagnetic propagation time across a layered media, such as snowpack or lake ice, can be remotely sensed.

Thermal emission from the ground under the snowpack propagates up through the snowpack to the receiver. At sufficiently long wavelengths, when the upper and lower surfaces of the snowpack are smooth, additional paths result from the reflection of the upward traveling wave from first the upper and then the lower surface of the snowpack. As a result, the thermal emission from a layer of snow can experience multiple reflections in the layer. These waves are identical at the antenna, except for their amplitude and the time lag associated with the extra transit of the snowpack.

For sufficiently long wavelengths, the snow grains that cause the scattering are sufficiently deep in the Rayleigh region to be of minor importance. Unlike scatter darkening technique, where the microscopic properties of snow dominate the signal, and the desired macroscopic properties are secondary, for WiBAR, snow depth and snow density, however, the most important parameters determining the signal, (and that is how the radiometer can measure SWE). In addition, the microscopic properties, responsible for the scattering, reduce the signal strength but do not alter the quantification of the accumulation. The bandwidth of the radiometer determines the minimum vertical extent that is observable. A wide bandwidth (several gigahertz) is desired for the relatively shallow snow covers encountered on Earth.

Figure. 1.1 shows a three layered structure of soil-snow-air, where the direct and the delayed ray are captured by the radiometer. The delayed ray experienced more attenuation due to more absorption and scattering in the snowpack layer.

Before traveling to the radiometer's antenna, the delayed ray travels twice in the snow layer with a one-way transit time in the pack of τ_{snow}. Thus the delayed ray

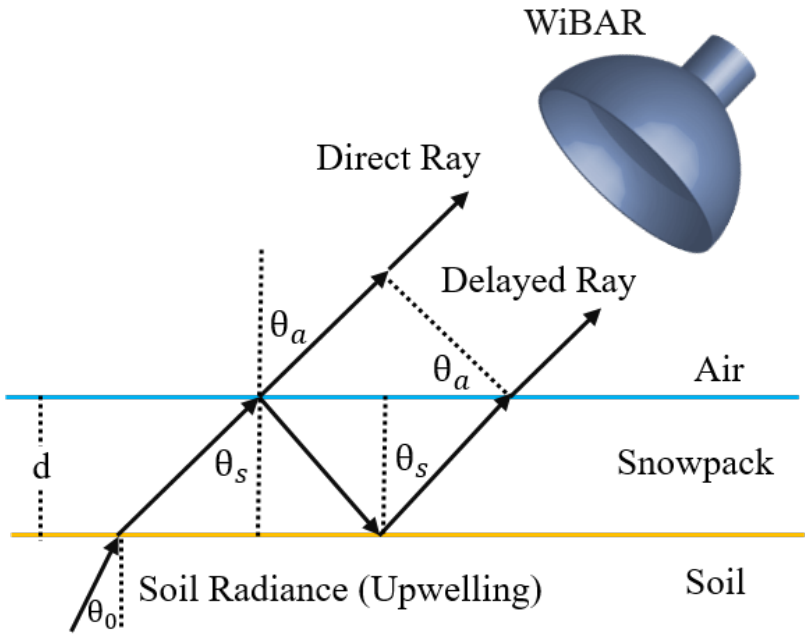

Figure 1.1: WiBAR concept consist of a layer of ice/snow on top of ground. The direct path of the emission of the underlying layer as well as the delayed ray are shown by solid arrows.

arrives to the radiometer's antenna with a delay of $\tau_d = 2\tau_{snow} - \tau_a$ relative to the direct ray (*Mousavi et al.*, 2018). where τ_a is the traveling time of direct ray in the air:

$$\tau_d = 2\tau_{snow} - \tau_a \tag{1.1}$$

$$\tau_a = \frac{2d \tan\theta_s \sin\theta_a}{c} \tag{1.2}$$

$$\tau_{snow} = (\frac{d}{cos\theta_s})(\frac{n_{snow}}{c}) \tag{1.3}$$

The incidence angle, θ_a and the angle θ_s are related by Snell's law $n_{snow}.\sin\theta_s = \sin\theta_a$. The microwave propagation time, τ_d, through the pack is:

$$\tau_d = \frac{2d}{c}\sqrt{n_{snow}^2 - \sin^2\theta_a} \tag{1.4}$$

where d is the thickness of the layer, c is the speed of light in free space, n_{snow} is

the refractive index of the slab, and θ_a is the incidence angle (*Evans*, 1965; *Mousavi et al.*, 2016b, 2019, 2016a).

An estimate of the refractive index of the dry snowpack can be obtained by from the empirical relationship:

$$n_{snow} = \begin{cases} \sqrt{1 + 1.9\rho_s} \ for \ \rho_s \leq 0.5 \ g.cm^{-3} \\ \\ \sqrt{0.51 + 2.88\rho_s} \ for \ \rho_s \geq 0.5 \ g.cm^{-3} \end{cases} \tag{1.5}$$

where ρ_s is the density of dry snowpack. The delay time can be estimated by performing an inverse fast Fourier transform (IFFT) of the emissivity spectrum $e(f)$ to produce an autocorrelation function (ACF).

The SWE then can be calculated by balancing the mass of water and ice of the snowpack:

$$\rho_w SWE = \rho_i \int v_1 dz \tag{1.6}$$

where ρ_w is the density of liquid water and ρ_i is the density of fresh water ice . Using equations 1.3 and 1.6, the time delay can be calculated as a function of SWE (*Nejati*, 2014).

However, many challenges need to be addressed to advance the future airborne and spaceborne operation of WiBAR. Some of these challenges and the proposed solutions are presented in this dissertation.

1.4 Technical Challenges

1.4.1 RFI

The radio frequency spectrum is heavily used for different applications like radio navigation, television broadcast, mobile communications, and a host for other applications (*Johnson et al.*, 2021). The absence of significant spectrum reserved for passive microwave measurements, results in presence of narrowband radio frequency interference (RFI) in the WiBAR's frequency of operation. RFI reduces the ability of the WiBAR to measure the layer's thickness accurately by raising the noise floor of the autocorrelation function.

In Fig. 1.2a the measured spectrum of a layer of ice with the thickness of 36.8 cm, which has been collected during the winter of 2016 is shown. Figure. 1.2b depicts the simulated RFI, which is modeled by impulse functions of varying amplitudes distributed in the measured spectrum. Figure 1.3 shows the ACF result for both cases of the spectrum with and without RFI. The time delay is detectable when there is no RFI on the spectrum. However, RFI increases the noise level of the ACF, and the peak of ACF is not detectable in the second scenario.

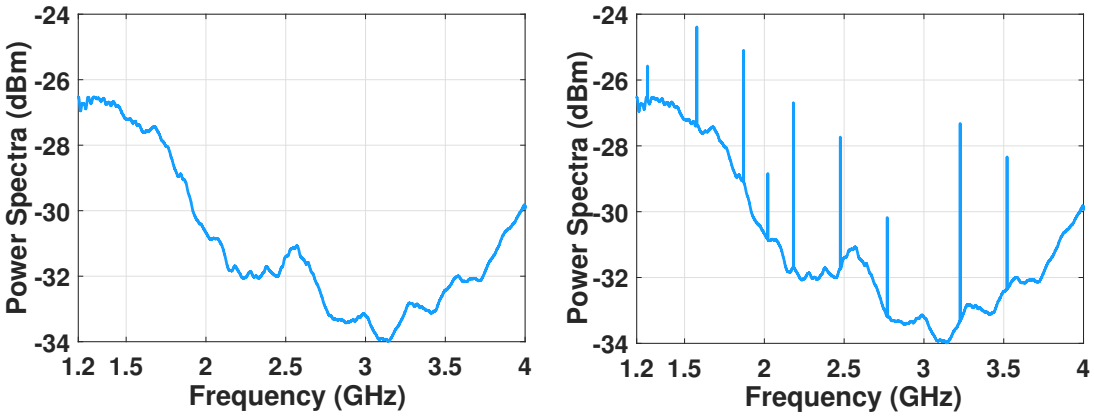

(a) (b)

Figure 1.2: a) The measured spectrum of the 36.8 cm thick ice layer of Douglas lake in 2016. b) Measured spectrum with simulated RFI added to it.

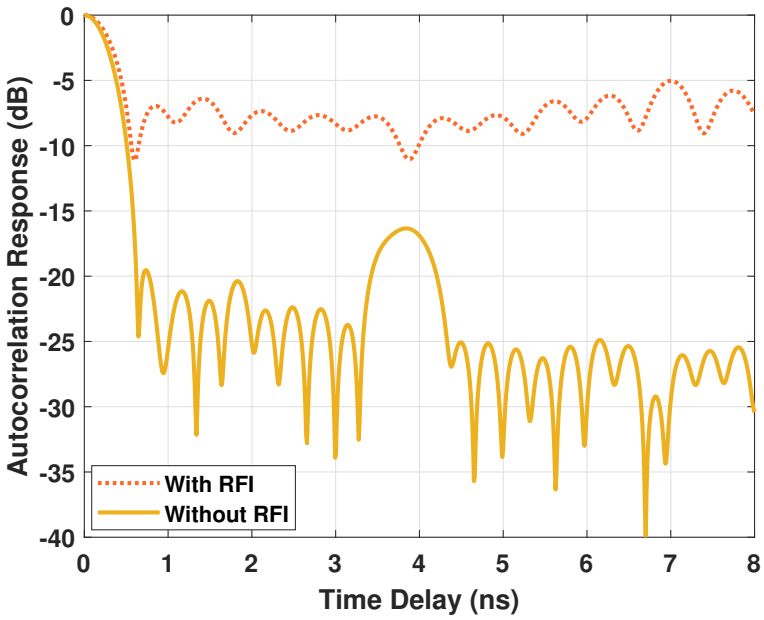

Figure 1.3: ACF of the lake ice with a thickness of 36.8 cm using frequency domain calibrations for cases in which the spectrum includes a simulated RFI and without RFI.

While there is no universal RFI mitigation method, RFI suppression may be implemented as part of the data processing. For example the frequency of operation of ultra-wideband software-defined radiometer, UWBRAD, is 0.5-2 GHz, and it has the capability of identifying and mitigating RFI through software-defined algorithms in real-time and post-processing of the acquired data (*Andrews et al.*, 2018).

Although the WiBAR technique requires a wide frequency span at long wavelengths, it does not require an equivalent noise bandwidth (ENBW) as high as its frequency span. In this dissertation a new microwave frequency tunable comb filter (*Salim et al.*, 2020) is proposed to mitigate the RFI. The comb filter's response and the passbands locations can be easily tuned over the frequency band by changing the loop phase using a phase shifter which makes the filter suitable for RFI mitigation purposes.

1.4.2 Receiver Design and Calibration

In the frequency domain approach of WiBAR, the receiver is a field-portable spectrum analyzer, which produces a number of frequency samples in the spectrum. The acquired data is post-processed to obtain the autocorrelation function. To eliminate the dependency of the spectrum on the receiver's gain and noise temperature, the power spectrum of the target is calibrated using two approximate emissivities of unity and zero, a matched load and a cold-FET, respectively.

However, this method suffers from high data acquisition time, which limits the applications of WiBAR for spaceborne or airborne platforms. The time-domain WiBAR, TD-WiBAR, is an alternative approach that uses a digital oscilloscope instead of a spectrum analyzer for data collection and thus TD-WiBAR requires a new calibration method. This dissertation proposed a TD-WiBAR calibration, and we designed the TD-WiBAR instrument and tested it. In addition, the WiBAR instrument is enhanced with the proposed comb filter for RFI mitigation.

1.4.3 Vegetation Canopy Over the Snow Layer

Instruments like WiBAR measure the microwave emission from a scene of snow and ice over a wide and low frequency band where volume scattering within the snow/ice layer is negligible. Experiments have demonstrated that such wideband brightness temperature spectra can show oscillatory features. These features arise from coherent interference among the direct upward emission and its replicas from multiple reflections, are related to the layer thickness of snow or ice, and can be affected by interface roughness or any above snow vegetation canopy.

It is noteworthy that such oscillatory patterns can be affected by the inhomogeneous scene, the interface roughness (*Sanamzadeh et al.*, 2017) and the above snow vegetation canopy. The scene inhomogeniety, as exemplified by variations in layer thickness within the radiometer footprint, is possible to average and smooth out the coherent

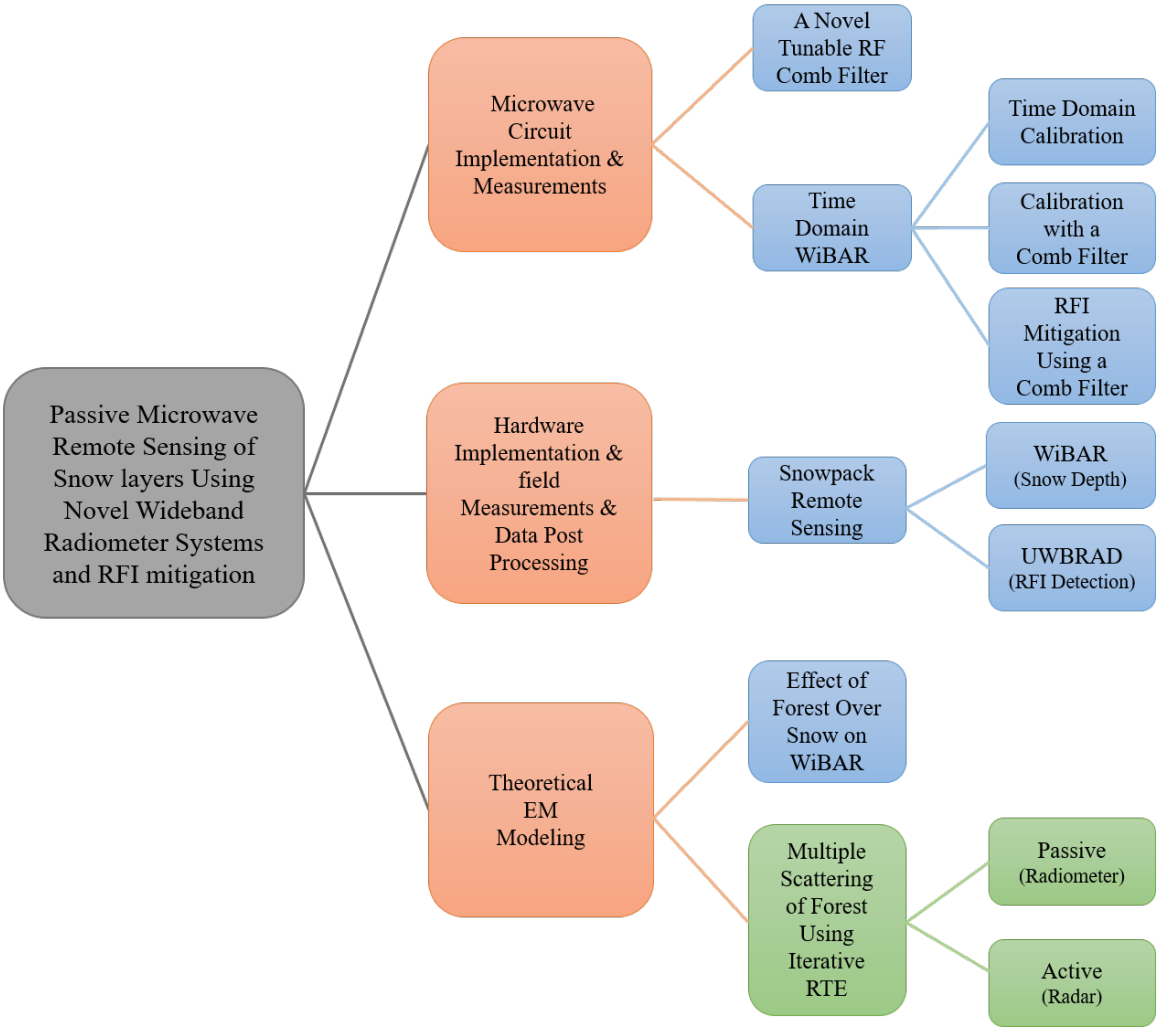

Figure 1.4: Overview of the topics that are covered in this dissertation.

wave interference patterns. The interface roughness, which is common in all natural interfaces, can cause polarization and angular coupling of microwave emissions, and succeedingly weaken or destroy the wave coherence when the scale of roughness is comparable to wavelength. In this dissertation we analyze the effects of an above snow vegetation layer on brightness temperature spectra, particularly the possible decay of wave coherence arising from volume scattering in the vegetation canopy.

1.5 Dissertation Overview

In Chapter II a new filter is proposed to suppress radio frequency interference (RFI) in microwave remote sensing instruments, particularly a WiBAR. RFI increases the noise floor and results in a decreased signal to noise ratio (SNR) of the WiBAR delay peak. The proposed filter operates like a Fabry-Perot interferometer (FPI) in optics and has the frequency response of a comb filter with many evenly spaced alternating pass and stop bands. The frequencies of these bands are varied with an electrically adjustable phase shifter. The design of a comb filter with an Airy finesse value of 20 has been verified by simulation and measurement.

Chapter III presents a new calibration for time-domain wideband autocorrelation radiometry (TD-WiBAR). The time-domain model of WiBAR is faster than the FD-WiBAR but requires its own calibration. We proposed a new calibration and then investigated a WiBAR set-up in the laboratory with data collected from a simulation circuit using a Keysight Spectrum Analyzer. The data are further post-processed for the time and frequency domain calibration. In addition, the available radio frequency interference (RFI) in the frequency operation of WiBAR increases the noise floor and results in a decreased signal-to-noise ratio (SNR) delay peak in the autocorrelation function of the WiBAR from which the snow depth is extracted. In this chapter, we enhanced WiBAR with a comb filter with the frequency response with many evenly spaced alternating pass and stop bands for RFI suppression. We set up a WiBAR with a comb filter in the laboratory with a simulation circuit to create a polluted spectrum with RFI to show the mitigation of RFI in the received signal using the new instrument.

Chapter IV presents a study of snowpack thermal emissions at long wavelengths and over a wide frequency band. Brightness temperature measurements of a snow layer are reported and used to estimate the travel time through the layer. The

ultra-wideband software-defined radiometer (UWBRAD) and the wideband autocorrelation radiometer (WiBAR) were deployed at the Keweenaw Research Center (KRC) from February 2020 to May 2021 to demonstrate these techniques. Results on snowpack brightness temperature and thickness measurements are presented and discussed.

In chapter V, the effects of an above snow vegetation layer on brightness temperature spectra, particularly the possible decay of wave coherence arising from volume scattering in the vegetation canopy is analyzed.

In Chapter VI, a unified framework of vegetation scattering using radiative transfer theory for passive and active remote sensing of vegetated land surfaces, especially those associated with moderate to large vegetation water contents (VWCs), e.g., forest, is presented. The framework allows for modeling passive and active microwave signatures of the vegetated field with the same physical parameters describing the vegetation structure. Radiative transfer equations are solved by a numerical iterative approach for both passive and active configurations. This approach allows for inclusion of higher order scattering which represents multiple scattering. In fields like forests with large VWCs, associated with large scattering albedo and optical thickness, multiple scattering effects are critical. In the active iterative approach, cyclical terms are identified and backscattering enhancement is included by doubling contributions from cyclical terms. The method is applied to aspen trees in forest fields to compute the brightness temperatures and backscattering coefficients for passive and active remote sensing configurations, respectively. In the passive configuration, for forest field with VWC of 15 kg/m^2, the deviation between zeroth-order brightness temperature, i.e., the tau-omega model results, and multiple scattering results around 40° observation angle can be as large as 50 K for vertical polarization and 35 K for horizontal polarization. The proposed approach is thus suitable for vegetation scattering with large VWCs. Furthermore, the proposed model is validated with the passive and

active L-band sensor (PALS) acquired in SMAPVEX12 measurements in 2012, which demonstrates the applicability of this model.

Chapter VII provides conclusion and recommendations for future work.

CHAPTER II

A Novel Frequency Tunable RF Comb Filter

2.1 Introduction

Wideband autocorrelation radiometry (WiBAR) is a recently developed microwave radiometric technique to directly measure the thickness of low-loss dielectric slabs such as lake ice or seasonal snow on the ground (*Mousavi et al.*, 2018). Some of the thermal emission from the layer under the slab experiences multiple reflection within the slab prior to propagating to the WiBAR antenna. The receiver of a WiBAR measures the transit time of the bouncing signal in the slab by calculating the complex autocorelation of the emission. This technique requires a wide frequency span (F_s) for a fine temporal resolution, but it does not need a large equivalent noise bandwidth (ENBW). However, the presence of narrow band radio frequency interference (RFI) signals, ubiquitous in the WiBAR's frequency of operation (L-band), degrades its ability to correctly measure the slab thickness by raising the autocorrelation function noise floor.

A comb filter could provide the wide frequency span while rejecting the worst of the RFI in that span. This comb filter is a microwave circuit analog of a Fabry-Perot interferometer (FPI) in optics. The simplest form of FPI is made up of two metal film reflectors. The FPI can be tuned by changing the space between the reflectors (*Mahapatra and Mattoo*, 1986; *Vail et al.*, 1995). The proposed microwave comb

filter consists of two directional couplers connected in a loop with transmission lines. The directional couplers play the role of reflectors in a FPI, and the spacing of the passbands depends on the length of the transmission lines in the loop (*Coale*, 1956; *Wing*, 1959). Recently, there have been studies on single-notch tunable filters over a wide frequency band (*Ko et al.*, 2015; *Cheng and Rebeiz*, 2012; *Psychogiou et al.*, 2015; *Tang and Chen*, 2015). (*Sorocki et al.*, 2016) have proposed fixed-frequency traveling wave filters using cascaded directional couplers. In this chapter, a new configuration of a directional filter is presented in which frequency selectivity is achieved in the pass band output by changing the filter's loop phase. The resulting comb filter has a tunable passband without frequency conversion (*Salim et al.*, 2020).

2.2 Theory of Comb Filter

Directional filters are usually used for combining or separating signals of different frequencies in communication systems. For providing band-pass and band-stop operations, different methods like traveling wave loop resonators, half wavelength resonators, and differential band rejection filters are used.

A traveling wave directional filter is characterized by a four port network, illustrated in Fig. 2.1a. One port is always isolated from the input port, and the input port is assumed reflectionless. The input power emerges from the output port with the frequency response of band-pass filter and the rest of the power emerges from another port with the frequency response of a band-rejection filter (*Coale*, 1956; *Walker*, 1978).

The traveling wave directional filter is constructed of two directional couplers connected by a transmission line loop as in Fig. 2.1b. The microwave propagation velocity divided by the electrical length of the two transmission lines between the couplers (including the couplers) determines the spacing between passbands, analogous to how the Free Spectral Range (FSR) of an FPI is the round trip transit time between

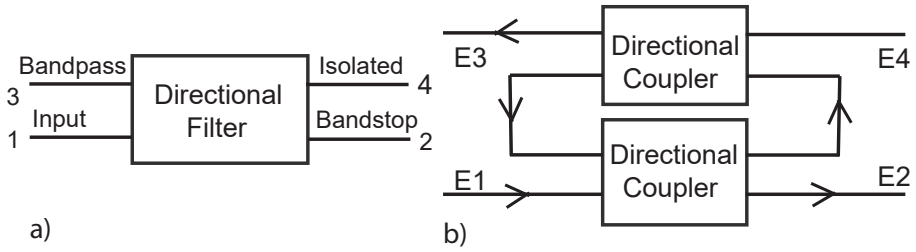

Figure 2.1: Schematic of a traveling wave filter. a) The band of interest is coupled from port 1 to port 3, and the rest of the frequency band is transmitted to port 2. b) The filter consists of two directional couplers and transmission lines.

reflectors. The traveling-wave loop filter scattering matrix elements are given by

$$S_{21} = \frac{(1-c_1^2)^{1/2} - (1-c_2^2)^{1/2} g_l e^{-j\phi_l}}{1-(1-c_1^2)^{1/2}(1-c_2^2)^{1/2} g_l e^{-j\phi_l}} \tag{2.1}$$

$$S_{31} =$$

1-(1-c$_1^2$)$^{1/2}$(1 − c_2^2)$^{1/2}$$g_l e^{-j\phi_l}$

(2.2)

and $S_{41} = 0$, where c_1^2 and c_2^2 are the power coupling factor of the couplers, ϕ_l is the loop phase, g_l is the loop voltage gain and g_{lu} (ϕ_{lu}) is that portion of the loop gain (phase) in the path from port 1 to port 3. When both halves of the loop are the same, $g_{lu} = g_l^{1/2}$ and $\phi_{lu} = \phi_l/2$. The loop gain g_l must not exceed unity, lest the filter oscillate. Center frequencies of the comb filter passbands occur when $\phi_l = 2n\pi$, where n is a whole number indicating the number of wavelengths around the loop (*Coale*, 1956).

Maximum $|S_{31}|$ requires the same coupling factors for both couplers, i.e. $c_1 = c_2 = c$. The minimum $|S_{31}|$ occurs when ϕ is an odd multiple of π. For $g_l \approx 1$, $\min|S_{31}| = (1/2)c^2$. That is, the filter rejection, in dB, is twice the coupling plus

6 dB. The Airy finesse, F_A, of a FPI is defined as its passband spacing divided by the full width at half-maximum bandwidth, FWHM, of its resonances. The Airy finesse value is given by

$$F_A = \frac{\pi}{2} \Bigg/ \sin^{-1}\left(\frac{1-\left((1-c_1^2)(1-c_2^2)g_l\right)^{1/2}}{2\left((1-c_1^2)(1-c_2^2)g_l\right)^{1/4}}\right) \tag{2.3}$$

and thus is determined solely by the coupling and the loop loss, and is independent of the electrical length of the filter loop. The basic principles of the proposed comb filter can be observed from the effect of variation of the loop gain and loop phase of the structure.

Fig. 2.2 depicts a simulation of the filter response to the change of loop gain and phase of a comb filter made from two 20 dB couplers with a loop travel time of 1.5 ns. Increasing the loss from 0 dB to 2 dB, as in Fig. 2.2a, results in a decrease of the peak of the passband by nearly 30 dB. Fig. 2.2b shows the effect that a change of the loop phase has on the filter's response. A 360° change of the phase (as by a phase shifter) sweeps the passbands over the filter's passband spacing. For example, a change of 20 degrees results in a 37 MHz frequency shift of the response of this filter with its 667 MHz passband spacing.

2.3 Circuit Design

Our application requires a tunable comb filter operating from 1 to 2 GHz, a FSR smaller than 25 MHz, and rejection as high as practicable. Other parameters of the comb filter, such as insertion loss and noise figure, can be accommodated by the design of the rest of the receiver.

The coupling of the directional couplers affects many performance parameters of the comb filter, and so should be selected first. To maximize the passband transmission, the two couplers will have the same coupling factors. We chose two

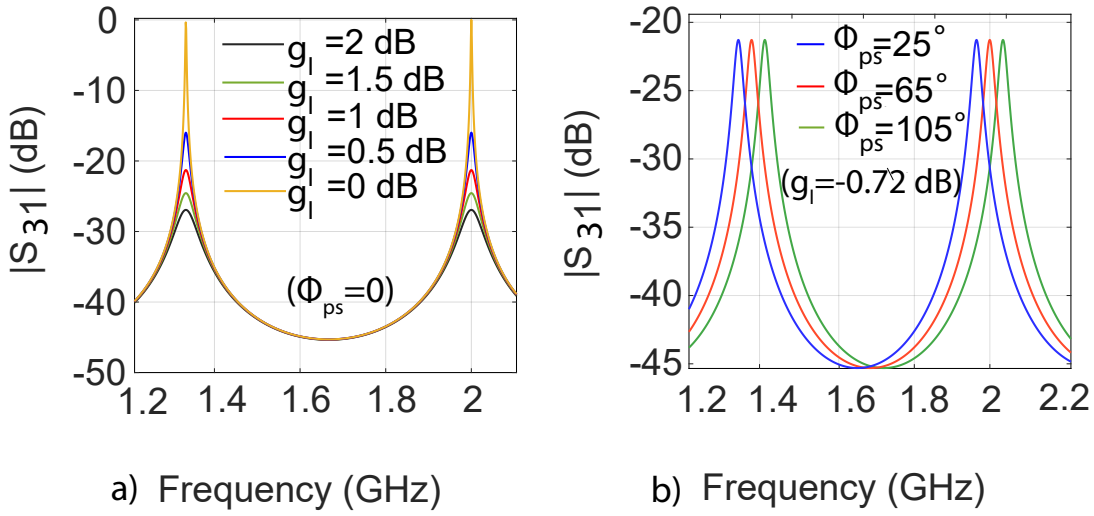

Figure 2.2: The variation of the comb filter's transmission coefficient as given by (2) w.r.t. a) change of loop gain ($\Phi_{ps} = 0$). The filter's response is very sensitive to a slight change of loop gain. b) change of loop phase ($g_l = -0.72$ dB). Loop phase variation results in a frequency shift of the pattern. Φ_{ps} is the phase shifter setting.

$-20\log_{10}(c)$=20 dB couplers so that the assumption of negligible return loss remained valid, resulting in a maximum rejection of 46 dB and maximum possible finesse of over 300. Our application requires temporal correlations imposed by our filter exceed 12 ns, so the component providing the majority of our loop phase is a 3 m long semi-rigid coaxial cable. Tuning can be provided by an adjustable length of transmission line, or a phase shifter. Electronically tuning a variable length of line requires a rather complex switching network, so we opted for an electronic phase shifter. Since the phase shift of the phase shifter is constant with respect to frequency, as opposed to proportional with a line stretcher, the passband spacing remains constant as the filter is tuned. To take full advantage of the comb filter's ability to be tuned, the phase shifter should provide 360° of tuning in at least as many steps as the comb filter finesse.

A long transmission line can have a significant phase variation (0.24°/GHz/foot (*Smith-Berry*, 2020)) over a temperature change from 0° to 25°C, resulting in 1.8 MHz shift of a passband. The phase shifter can correct this temperature range. These

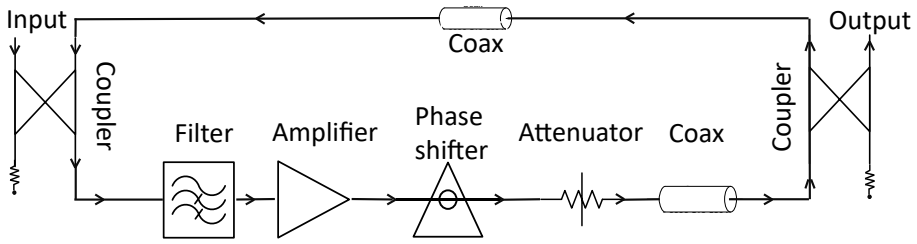

Figure 2.3: Schematic block diagram of the comb filter. Couplers are the essential parts of the filter. The phase shifter is used for frequency scanning and, with help of the amplifier and attenuator, the loop gain is just under unity. The open loop gain and phase were measured on a network analyzer with the comb filter input and output terminated, and the loop broken at the left side upper coaxial cable.

components, especially the phase shifter, introduce unavoidable losses into the loop (see Table 2.1). These losses (5 dB) reduce the finesse of the comb filter to about 10.5. To restore the loop gain, we incorporate into the loop a low-noise amplifier with flat gain as a function of frequency. The amplifier also provides directivity, attenuating waves travelling backward around the loop caused by reflections.

The inclusion of an amplifier results in a loop gain that exceeds unity. To prevent oscillation, we incorporate a step attenuator to reduce the maximum loop gain back to near, but less than, 0 dB. We selected an electronically adjustable attenuator for this task, partly for its ability to adjust to fractions of a dB of attenuation, partly for expected variations in the insertion loss of the phase shifter, and partly for a complete characterization of the comb filter. A fixed attenuator of an appropriate value could be used in place of the step attenuator.

In our application, we will be monitoring the output power and performing an autocorrelation on the output signal, and these measurements can be used to confirm that oscillations do not exist. Finally, a high-pass filter is included to avoid oscillation at out-of-band frequencies. The corner frequency corresponds to the lowest frequency of desired operation. Figure 2.3 shows the block diagram of resulting comb filter.

2.4 Hardware Implementation

2.4.1 Measurement Setup and Results

A comb filter made entirely from commercial off-the-shelf (COTS) components that is set up with tunable loop gain and loop phase is shown in Fig. 2.4. The variable step attenuator is tuned so that the loop gain is just below one. Table 3.1 shows the amount of loss for each component. A low noise amplifier provides 16 dB of gain, the phase shifter's loss is 3.5 dB, the summation of the losses of the cables, the high pass filter, and the through ports of couplers are 2.5 dB.

The circuit has a measured output-referenced third-order intercept points (OIP3) ranging from -10 to -20 dBm for the passbands. While low, as a result of the loop's OIP3 being reduced by the output coupler's coupling, this is sufficient for microwave radiometry. The power consumption by all of the active components is 1.4 W.

	Components	Manufacturer	Number	S_{21} (dB)
A	High Pass Filter	Mini Circuits	VHF-740	-1
B	Low Noise Amplifier	Mini Circuits	ZX60-P105LN+	16
C	Phase Shifter	Vaunix	LPS-202	-3.5
D	Attenuator	Mini Circuits	ZVVA-3000	-10
E	Coupler	P1dB	P1CP-SAF-R502G	-0.5
F	Cable	P1dB	P141CJ30	-1

Table 2.1: Power transmission of the comb filter's components.

The measured frequency response of the comb filter as a result of changes in the phase of the loop is shown in Fig. 2.5. A phase shift of 360° results in a shift of one FSR. Other parameters like finesse and FSR are unaffected by the phase shifter setting. The frequency tuning feature of the comb filter makes it suitable for RFI suppression, since the RFI mitigation is complicated by the fact that the interference typically occurs in narrow bandwidths at seemingly random frequencies. By changing the loop phase, any desired frequency can be either passed or rejected. For the

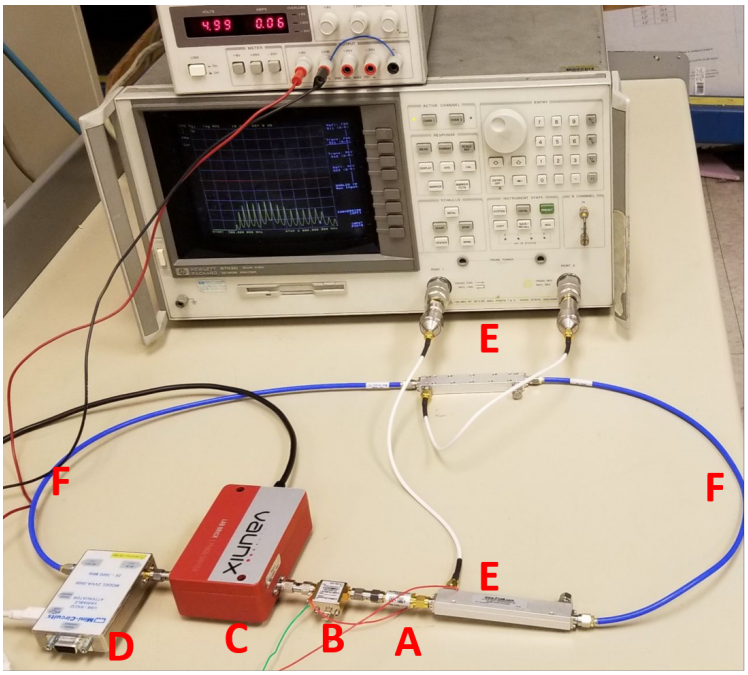

Figure 2.4: Microwave measurement set up of the comb filter. The response is measured with HP Network analyzer series 8753D.

WiBAR's application, we will maximize RFI mitigation by adjusting the comb filter phase to minimize output power.

This comb filter has an Airy finesse of 20 which indicates a large free spectral range with a small resonant bandwidth. The equivalent noise bandwidth (ENBW) of the filter is defined as the bandwidth of a brick-wall filter that produces same integrated noise power as that of an actual filter. The ENBW is 2.8 MHz at the 1.655 GHz pass band. The rejection bandwidth of the filter is around 108 MHz between the 1.5 and 1.6 GHz pass bands.

2.4.2 Comparison of Simulation and Measurement Results

The simulation of the comb filter is done in Advanced Design System (ADS) using full S-parameters measured for the components in Table 2.1 and performed for a one meter long cable (Fig. 2.6).

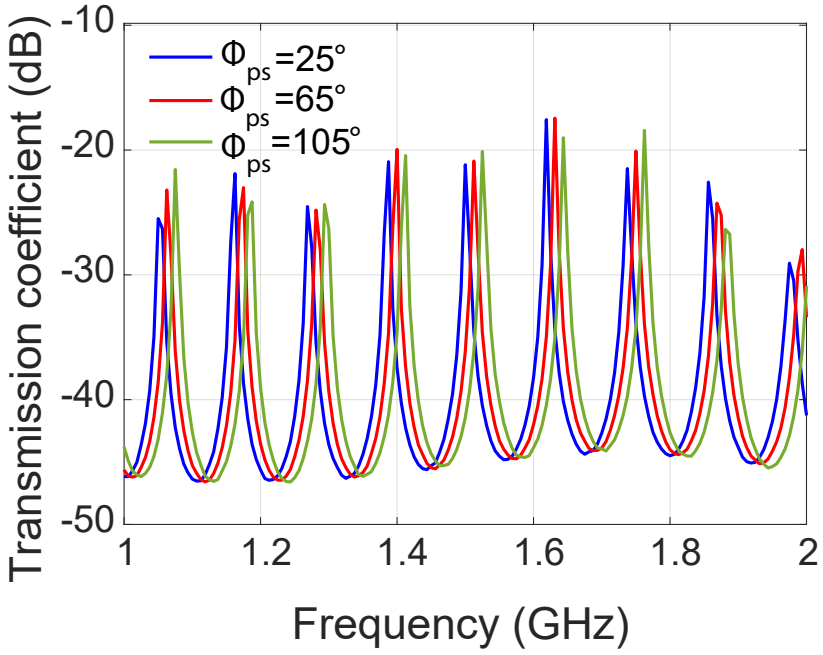

Figure 2.5: Measured bandpass response for different phase adjuster settings.

Figure 2.7 presents the simulated transmission coefficient for the comb filter using ADS, compared with experimental results. As shown in the figure, when the electrical length of the loop changes, a different number of peaks will be accommodated within the filter. The change in the FSR between the measurement and simulation results is due to accumulated phase errors at the connectors that are not considered in the ADS simulations.

2.4.3 Variance of Insertion Loss at Pass-band

The filter pass-bands exhibit a variance in their measured insertion losses. According to (2.2), the output voltage of the filter depends on the gain and phase of the open-loop circuit. Figure 2.8 a, b shows the measured gain and phase (as phase delay, ϕ/ω) of the open loop circuit. Figure 2.8 c shows the comparison of the measurements of the closed-loop filter with the open-loop circuit. The open-loop measurements are transformed with (2.2). The variance in the insertion loss of the

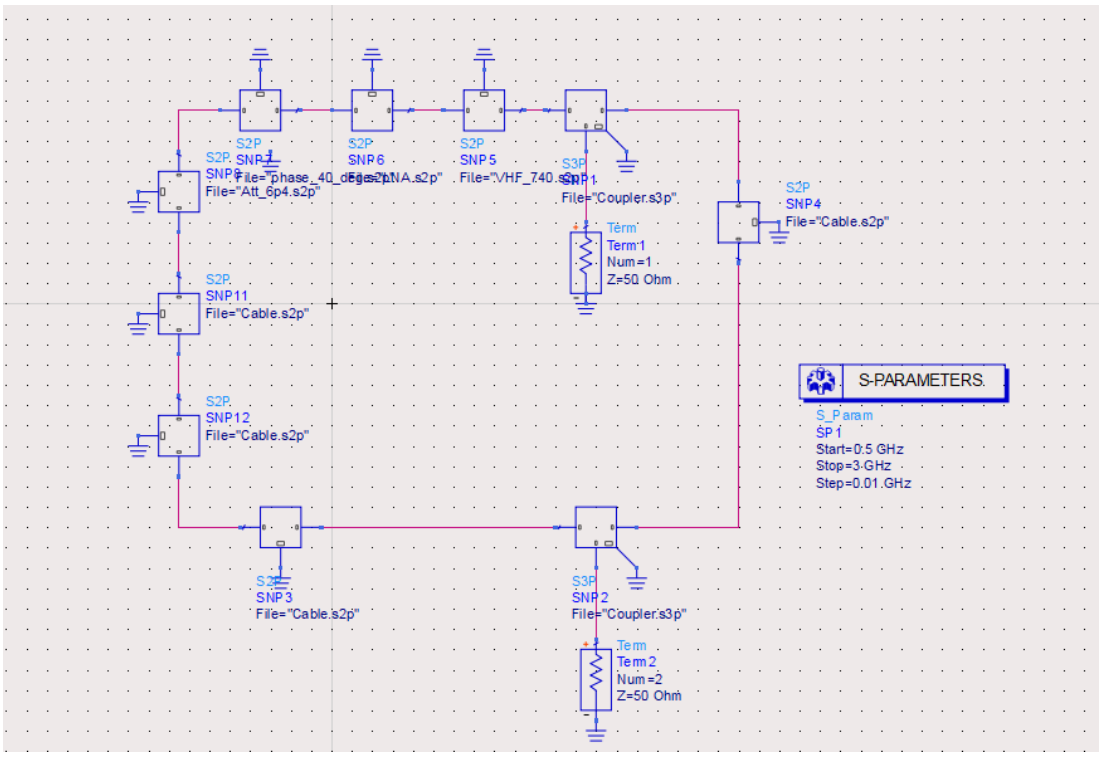

Figure 2.6: Schematic of the simulated comb filter in ADS.

pass bands of the filter is due to small variations in the open-loop gain over frequency.

2.4.4 Noise Figure

Output noise can be calculated using a cascaded network, resulting in a lowest calculated noise figure of 16.1 dB for a pass band, consistent with the measured noise figure in Fig. 2.9. Using an amplifier with the minimum necessary gain will beneficially impact the noise figure by minimizing the attenuation added to the loop. Judicious ordering of the components in the loop can have a minor impact on the filter noise figure and on the filter insertion loss.

In any event, the impact of this high noise figure can be reduced by sufficient low-noise amplification of the signal of at least 10dB more than this NF prior to the comb filter.

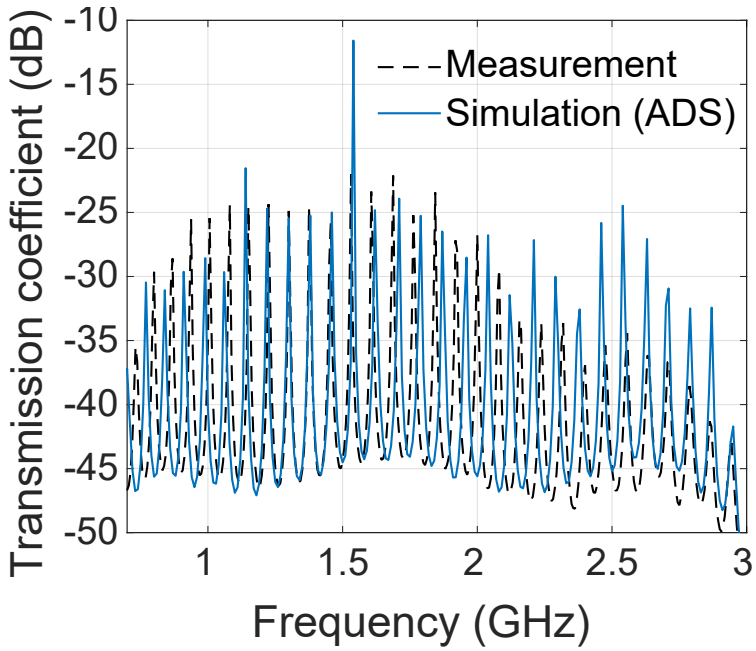

Figure 2.7: Comparison of the measured and simulated transmission coefficient for the comb filter with one meter long cable. Simulation is done using advanced designed system (ADS). Solid and dashed lines represent the simulation and measurement results of (S_{21}).

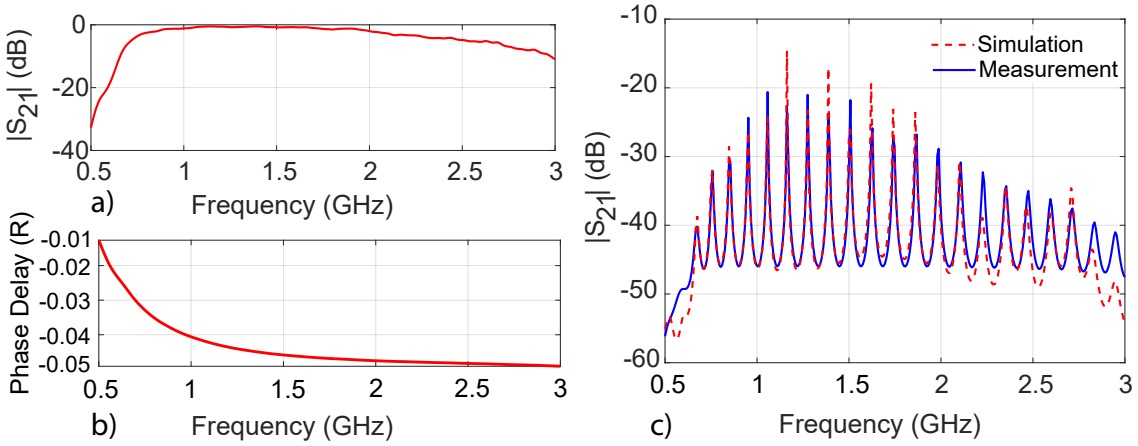

Figure 2.8: a) Measured gain of the open-loop. b) Measured phase delay of the open-loop. c) Comparison of the comb filter transmission coefficient measurement and prediction from Equ. 2.2 using the open-loop gain and phase.

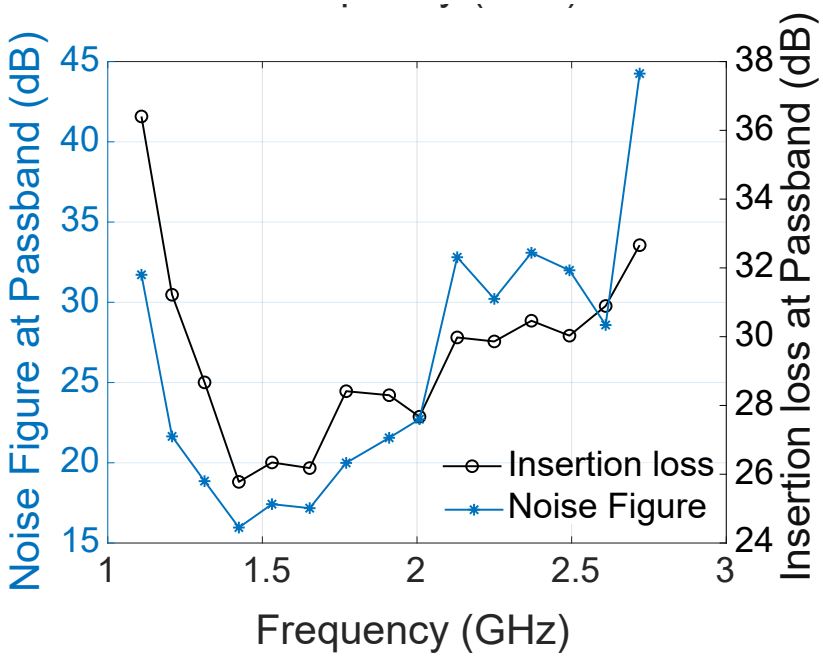

Figure 2.9: Measured noise figure and gain of the comb filter at pass band frequencies. The measurements are done using Keysight CXA signal analyzer series N9000B.

2.5 Conclusion

In summary, a new frequency tunable comb filter for RFI suppression is proposed. RFI in wideband autocorrelation radiometry results in an increased noise floor in the observation.

The proposed new comb filter has a spectrum with alternating pass and rejection bands which make it a suitable filter for WiBAR RFI mitigation. The theory for an ideal comb filter is based on the Fabry-Perot interferometer in optics. The basic concept of the proposed filter is the same as traveling wave filter which consists of transmission lines and two identical directional couplers in which the resonance occurs in the form of traveling wave instead of a standing wave.

Theoretical analyses of the circuit design has been provided giving insight into behavior of the frequency response of the comb filter with respect to the gain and

phase of the loop. Adding a phase shifter to the loop of the filter can can provide tunability for scanning through frequency in order to place the worst RFI in the rejection bands.

By inserting a low noise amplifier and step attenuator, the loop gain of the filter is optimized. We present a filter with Airy finesse value of 20 which combines a large free spectral range with a small resonant bandwidth.

The experimental results show good agreement with theory and simulation results. Next, we will evaluating the impact of comb filter on the performance of wideband autocorrelation radiometry.

CHAPTER III

Time Domain Wideband Autocorrelation Radiometry

3.1 Introduction

Wideband autocorrelation radiometry (WiBAR) offers a direct method to remotely measure the microwave propagation time difference of multipath microwave emission from low-loss layered surfaces, like snowpack and icepack. This technique measures the spacing between frequencies of constructive and destructive interference of the emission from the soil under the snow, which can reveal the microwave travel time through the snow, and thus the snow depth.

The current WiBAR instrument operates in the frequency domain and uses a field-portable spectrum analyzer as the receiver of the radiometer. However, the small instantaneous bandwidth yields a high data acquisition time. To address this issue, we introduced the time-domain WiBAR which replaces the field-portable spectrum analyzer with an oscilloscope for data acquisition. Large instantaneous bandwidth of time-domain WiBAR results in fast data acquisition.

In this chapter, we present a new calibration for time-domain WiBAR. The new time-domain calibration can be used in both frequency-domain and time-domain WiBAR (*Salim et al.*, 2020a). Furthermore, we enhanced the WiBAR instrument

with the comb filter in chapter II to mitigate the RFI in the frequency range of WiBAR. The laboratory set-up of the WiBAR sensor with a comb filter to mitigate the RFI in time-domain mode is demonstrated in this chapter.

3.2 Theory of WiBAR

The concept of wideband autocorrelation radiometry (WiBAR) has been proposed as a radiometric technique for the remote sensing of snow and ice layers (*England*, 2013). Figure 3.1 depicts the theory of WiBAR. Down-welling radiance from the sky and thermal emission from the soil under the snowpack, up-welling radiance, propagate up through the snowpack to the receiver. Down-welling and up-welling signals can be approximated as white noise band-limited by the bandwidth of the radiometer. At the upper interface, the power splits into two, which travel toward the radiometer's antenna. Part of the power transmitted across the upper interface toward the radiometer's antenna constitutes the direct ray. The part of the power reflected from the upper interface is the delayed ray. The observing antenna can receive both these waves, which are identical except for their amplitude and the time lag associated with the extra transit through the layer. The time lag which is the indication of the thickness of the layer is:

$$\tau_d = \frac{2d}{c}\sqrt{n_{snow}^2 - \sin^2\theta_a} \tag{3.1}$$

where d is the thickness of the layer, c is the speed of light in free space, n_{snow} is the refractive index of the slab, and θ_a is the incidence angle (*Evans*, 1965).

The receiver of the frequency domain WiBAR includes an antenna and a spectrum analyzer that is producing the power spectrum of the observation layer which is given

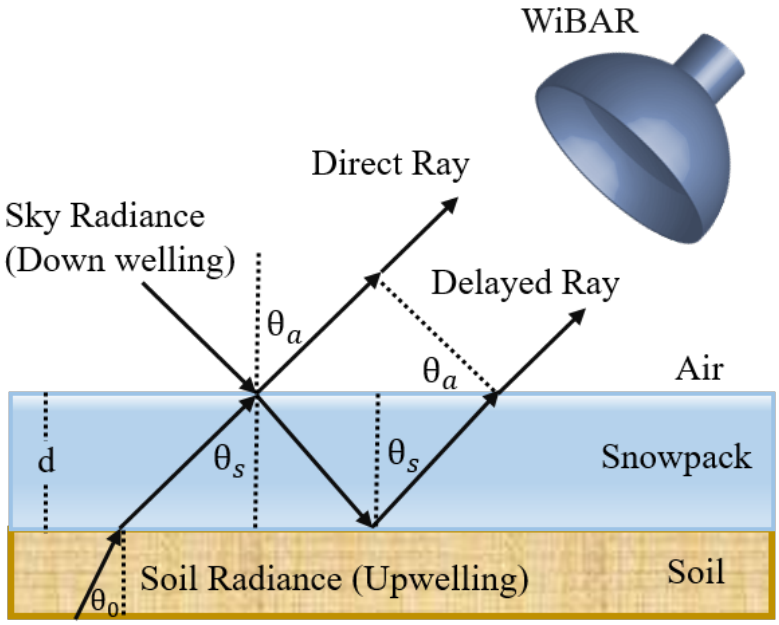

Figure 3.1: WiBAR sensed snowpack microwave travel time through the pack with thickness d. The delayed ray is delayed by $\tau_d = 2\tau_s - \tau_a$, relative to the direct ray.

by Eq. 3.2.

$$\begin{aligned} P_{scene}(f) &= K_B T_{SYS}(f) B_n G(f) \\ &= K_B (e_{scene}(f) T_{scene} + T_{REC}(f)) B_n G(f) \end{aligned} \tag{3.2}$$

where K_B is Boltzmann's constant, $T_{SYS}(f)$ is the receiver system temperature, B_n is the noise bandwidth, and $G(f)$ is the radiometer's gain. The system temperature is the sum of the receiver noise temperature, $T_{REC}(f)$, and the emissivity of the scene, $e(f)$, multiplied by the physical temperature of the scene, T_{scene}. To remove the dependency of the spectrum on the receiver gain and noise temperature, the power spectrum of the scene is calibrated using two approximate emissivities of unity and zero namely a matched load and a cold-FET, respectively. Equation 3.3 is the Frequency domain WiBAR calibration.

$$e(f) = \frac{P_{scene}(f) - P_{cold-FET}(f)}{P_{load}(f) - P_{cold-FET}(f)} \tag{3.3}$$

The autocorrelation function (ACF) of the emission, which can be achieved by the inverse fast Fourier transform of the spectrum is presented in 3.14.

$$\Phi_{scene}(\tau) = \int e_{scene}(f) w(f) e^{-j2\pi f\tau} df \tag{3.4}$$

where $w(f)$ is a window function for improving the sensitivity of the system. In the autocorrelation function of the frequency domain WiBAR, in addition to a large peak at zero lag, which is the correlation of the direct ray with itself, there is a lag peak due to the correlation of the delayed ray with the direct ray. This non-zero lag peak of the ACF has a local maximum at $\tau = \tau_d$ which indicates the time delay of the propagation inside the layer.

Figure 3.2 shows the measured spectrum of the ice layer of Doughlas lake with 36.6 cm thickness using the spectrum analyzer in frequency domain WiBAR and the corresponding autocorrelation response function of the measured spectrum. The second peak which occurs at 3.9 ns is the time delay of the microwave transition time in the ice layer.

3.3 Time Domain Calibration of WiBAR

The frequency-domain WiBAR suffers from high data acquisition time which limits its applications for spaceborne and airborne technologies. Time-domain WiBAR is an alternative method that uses a fast analog-to-digital converter feeding an autocorrelator implemented in a field-programmable gate array (field-programmable gate array (FPGA)) instead of the spectrum analyzer, resulting in faster data acquisition. The real part of the ACF is directly acquired by collecting a time series of voltages,

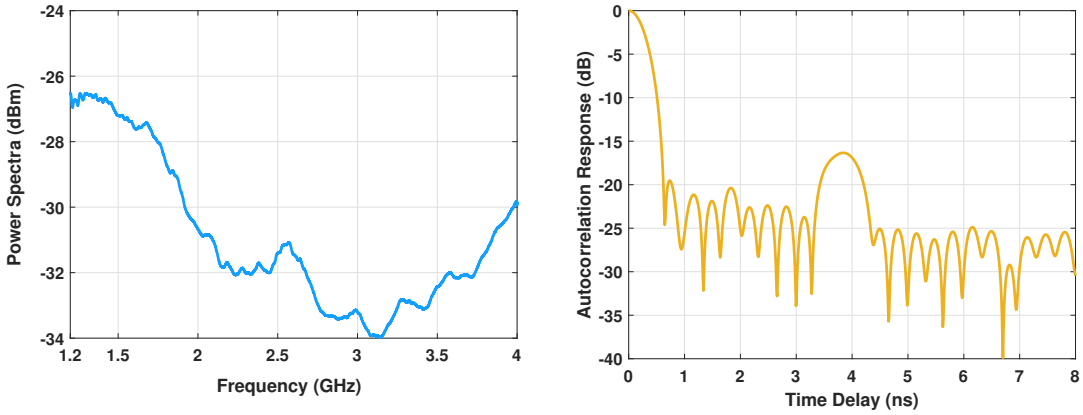

(a) (b)

Figure 3.2: a) The measured spectrum of the 36.8 cm thick ice layer of Douglas lake in 2016. b) ACF of the lake ice with a thickness of 36.8 cm using frequency domain calibrations for cases in which the spectrum.

$V(t)$, and correlating them at different time lags, τ. The imaginary part of the ACF is created from the real part using the Hilbert transform.

$$\Re e\left\{\Phi(\tau)\right\} = \frac{1}{N}\sum_{t=1}^{N} V(t)V(t+\tau) \tag{3.5}$$

However, TD-WiBAR requires a new calibration method which is presented here.

The autocorrelation function in the frequency domain wideband autocorrelation radiometry (FD-WiBAR) can be achieved by the inverse fast Fourier transform of the power spectrum:

$$\Phi_{Scene}(\tau) = \int S_{scene}(f)w(f)e^{-j2\pi f\tau}df \tag{3.6}$$

where $S_{scene}(f)$, is the power spectrum of the layer which is a derivative of the output power with respect to the frequency which is the same as the output power of the radiometer divided by the noise bandwidth of the receiver Eq. 3.7.

$$S_{scene}(f) = \frac{d}{df}P_{scene}(f) = \frac{P_{scene}(f)}{B_n} \tag{3.7}$$

According to Eq. 3.2, the autocorrelation response is a function of noise temperature and gain of the system, which are dependent on frequency. In order to be able to eliminate the dependency of the autocorrelation function on the receiver's noise temperature in Eq 3.8, we subtract the non-normalized ACF response of the scene and a reference, $e_{ref}(f)$.

$$\Phi_{Scene}(\tau) - \Phi_{ref}(\tau) = \int K_B(e_{scene}(f)T_{scene} + T_{ref})G(f)w(f)e^{-j2\pi f\tau}df \tag{3.8}$$

Similar to Eq 3.8 taking the difference of the non-normalized ACF response of two distinct references, Eq 3.9, can remove the dependency of the spectrum on gain Eq 3.10.

$$\Phi_{ref2}(\tau) - \Phi_{ref1}(\tau) = \int K_B(T_{ref2} + T_{ref1})G(f)w(f)e^{-j2\pi f\tau}df \tag{3.9}$$

$$\int G(f)w(f)e^{-j2\pi f\tau}df = \frac{\Phi_{ref2}(\tau) - \Phi_{ref1}(\tau)}{K_B(T_{ref2} - T_{ref1})} \tag{3.10}$$

Using Eq 3.8 the frequency-domain ACF can be reproduced:

$$\Phi(\tau) = \frac{1}{K_B T_{scene}}(\Phi_{Scene}(\tau) - \Phi_{ref}(\tau) + T_{ref}K_B \int G(f)w(f)e^{-j2\pi f\tau}df) \tag{3.11}$$

Then by substituting the Eq.3.10 into Eq 3.11, the non-normalized time-domain ACF can be achieved, which has no dependency on noise temperature and gain of the system Eq. 3.12.

$$\Phi_{TD-Cal}(\tau) = \Phi_{Scene}(\tau) - \Phi_{ref}(\tau) + T_{ref}\frac{\Phi_{ref2}(\tau) - \Phi_{ref1}(\tau)}{T_{ref2} - T_{ref1}} \tag{3.12}$$

To make the value of the ACF zero at zero lag, the T_{ref0} is defined according to Eq. 3.8:

$$T_{ref0} = T_{scene} \frac{\int e_{scene}(\tau) G(f) w(f) e^{-j2\pi f\tau} df}{\int G(f) w(f) e^{-j2\pi f\tau} df} \tag{3.13}$$

Substituting the integrals in the numerator and denominator of the Eq. 3.13:

$$T_{ref0} = (T_{ref2} - T_{ref1}) \frac{\Phi_{Scene}(0) - \Phi_{ref}(0)}{\Phi_{ref2}(0) - \Phi_{ref1}(0)} + T_{ref} \tag{3.14}$$

In the absence of the slab, the expected value of ACF should be zero. Equation 3.15 represents the ACF with zero contribution at all lags including zero in the absence of the multipath layer.

$$\begin{aligned} \Phi_0(\tau) &= \Phi_{TD-Cal}(\tau) \\ &= \Phi_{Scene}(\tau) - \Phi_{ref}(\tau) - \frac{T_{ref} - T_{ref0}}{T_{ref2} - T_{ref1}} (\Phi_{ref2}(\tau) - \Phi_{ref1}(\tau)) \\ &= \Phi_{Scene}(\tau) - \Phi_{ref}(\tau) - \frac{\Phi_{Scene}(0) - \Phi_{ref}(0)}{\Phi_{ref2}(0) - \Phi_{ref1}(0)} (\Phi_{ref2}(\tau) - \Phi_{ref1}(\tau)) \end{aligned} \tag{3.15}$$

Equation 3.16 presents the new normalized time-domain calibration which the differences of the raw ACFs in the numerators and denominators eliminate the dependence of the receiver noise figure. Also, the autocorrelation peak at zero lag is removed from the ACF response.

$$\Phi'_0(\tau) = \frac{\Phi_{Scene}(\tau) - \Phi_1(\tau)}{\Phi_{Scene}(0) - \Phi_1(0)} - \frac{\Phi_2(\tau) - \Phi_1(\tau)}{\Phi_2(0) - \Phi_1(0)} \tag{3.16}$$

where Φ_1 and Φ_2 representing the references of ColdFET and load. The advantage of

this new time-domain calibration is it can be applied to the data collected by a network analyzer, which we showed in this chapter, and it can be applied to time-domain measurements directly.

3.4 Calibration Uncertainties

There are some assumptions in the derivation of the time-domain calibration which cause the variability of the autocorrelation response. The proposed time-domain calibration did not consider the effect of a number of samples and variation of gain over the frequency band.

The number of samples collected per measurement can directly affect the variation of the system's temperature, T_{sys}, over the frequency. In addition, the receiver gain, $G(f)$, has random variations over the frequency. Also, if the amplifier's temperature changes, the amplifier's gain will change over all the frequency bands. The gain of the amplifier can be modeled as $G(f) = G(T_{amp})g(f)$ and since the temperature variation of the amplifier is random, $G(T_{amp})$ and $g(f)$ are random functions, assuming the amplifiers are not compressing.

3.5 Verification of TD-Calibration with FD-Calibration

We investigated a WiBAR setup in the laboratory with data collected from a simulation circuit using a Keysight Spectrum Analyzer. The data are further post processed for the time and frequency domain calibration to show the accuracy of the new time domain calibration.

3.5.1 Circuit Design of the Laboratory Setup of the WiBAR

A block diagram of the simple microwave circuit model of the WiBAR Sensor is shown in Fig. 3.3. In this instrument, the autocorrelation function (ACF) is generated

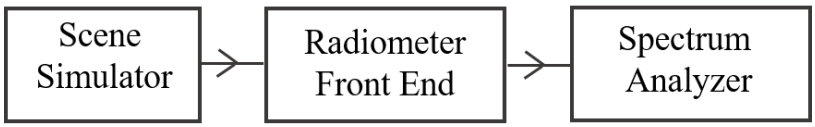

Figure 3.3: Block diagram simulated set-up of the simple WiBAR instrument.

by an inverse Fourier transform of the power spectral density from 0.5 to 2.5 GHz acquired with a Keysight spectrum analyzer. Thus, we can test the time-domain WiBAR calibration performance even though we are using a spectrum analyzer as the receiver.

The radiometer shown in Fig. 3.4 front-end includes a low noise amplifier, power amplifiers, and a calibration switch to ambient load and a cold-FET load (*Frater and Williams*, 1981).

A scene simulator is a microwave circuit that simulates layered media as depicted in Fig. 3.4. The upper directional coupler models the snow-air interface. The lower directional coupler models the soil-snow interface. The input of a low-noise amplifier (cold-FET) generates sub-ambient noise, simulating the sky's emission. The rotation of the signal inside the loop is similar to multiple internal reflections inside the layered media. The terminations represent the ambient source of Planck radiation, like the soil below the snowpack.

The signal splits into two paths; one part representing transmission in the air toward the radiometer receiver enters the spectrum analyzer. The other part of the signal rotates in the loop, representing the internal reflection at the snow-air interface, and remains inside the layer. The time delay is the microwave transit time inside the transmission lines, determined by the length of the line between couplers. The relative magnitude of the delayed ray to the direct ray is controlled with the coupling factors and fine-tuned with attenuators.

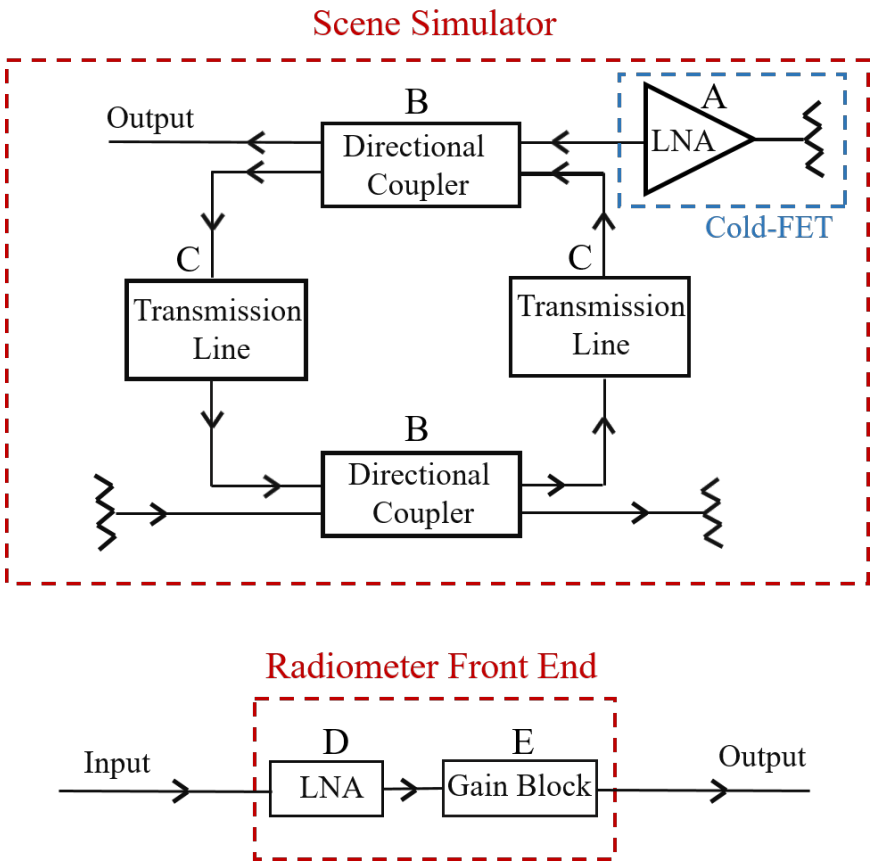

Figure 3.4: Schematic diagram of scene simulator including two directional couplers, coaxial cables, LNA, and match loads and front-end radiometer including LNA and gain block.

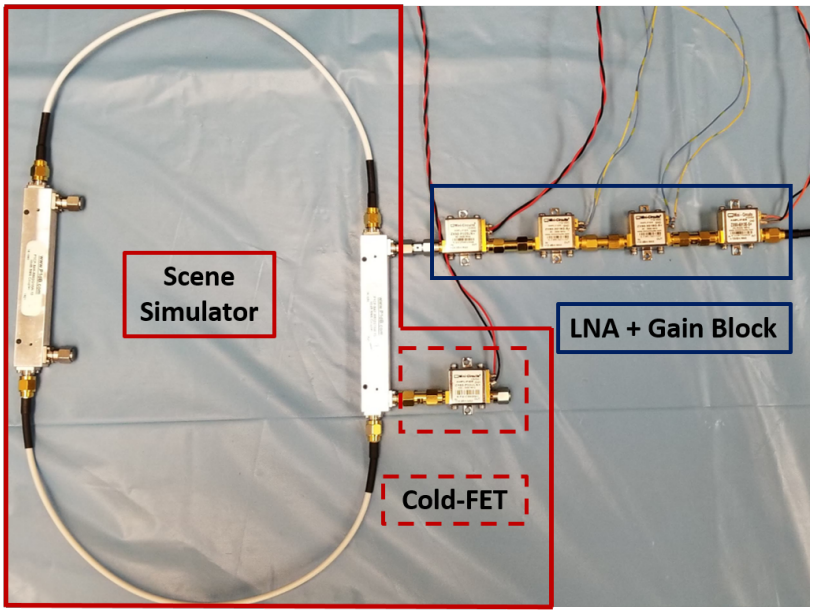

Figure 3.5: Simulated set-up of the simple WiBAR instrument in laboratory.

3.5.2 Hardware Implementations and Measurement Results

The proposed model has been implemented and tested in the lab. Figure 3.5 shows the set-up of the microwave circuit of WiBAR. The scene simulator includes two 10 dB couplers, and coaxial cables of 31 cm, and one ultra-low noise amplifier, representing the sky. We used an LNA and a gain block in the radiometer front-end. Table 3.1 shows the amount of loss and specifications for each component.

	Components	Manufacture	Number	S_{21} (dB)
A	Ultra Low Noise Amplifier	Mini Circuits	ZX60-P33ULN	16
B	Coupler	P1dB	P1CP-SAF-R502G	-0.5
C	Cable	P1dB	P141CJ30	-1
D	Low Noise Amplifier	Mini Circuits	ZX60-P105LN+	16
E	Gain Block	Mini Circuits	ZX60-3018G-S+	40

Table 3.1: Power transmission of the components' simulated set-up.

Figure 3.6 shows the measurement results of the spectrum for the scene simulator, load, and cold-FET. The cold source is generated by the input of the ultra-low noise amplifier, *Frater and Williams* (1981), then amplified with the chain of amplifiers

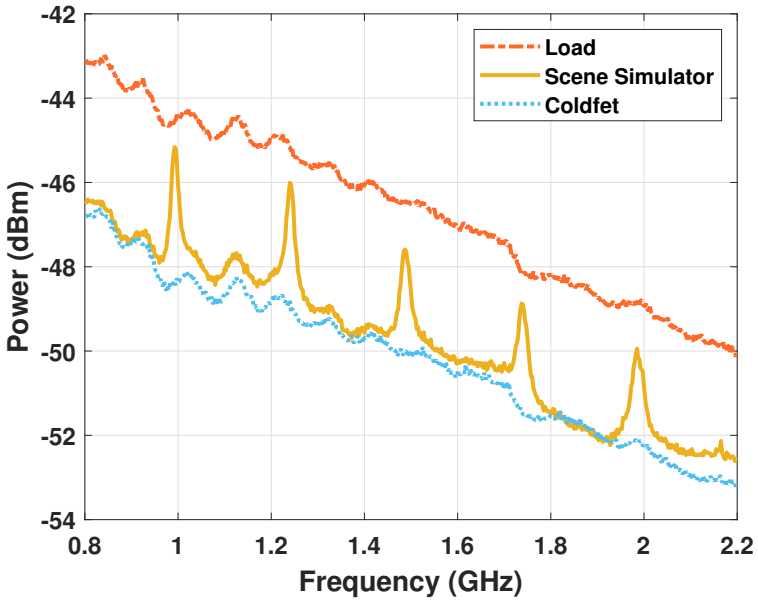

Figure 3.6: Measurement results at the output of the RF front end, with the load, cold-FET, and scene simulator as input to the RF front end. Measurements are done using a Keysight spectrum analyzer. The 250 MHz spacing between the scene simulator peaks corresponds to a 4 ns trip around the scene simulator loop.

indicates the approximate emissivity of zero. The 250 MHz spacing between the scene simulator peaks corresponds to a 4 ns trip around the scene simulator's loop.

The thermal noise of the load, which is proportional to the ambient temperature, is amplified by a chain of amplifiers that represents the reference with the approximate emissivity of unity. The autocorrelation response of time and frequency domain calibration for measured power spectrum is shown in Fig. 3.7.

The time delay at 4 ns is detectable in the ACF for both TD and FD calibrations, and the two calibrations are in good agreement. The TD-WiBAR calibration is constructed such that the ACF peak at zero lag is removed from the ACF, which has an additional advantage in that side lobes of the impulse response does not contribute to the noise floor, potentially masking weak signals. The large peak near 8 ns is the correlation of the direct ray with a doubly-delayed ray that went around the scene simulator loop twice.

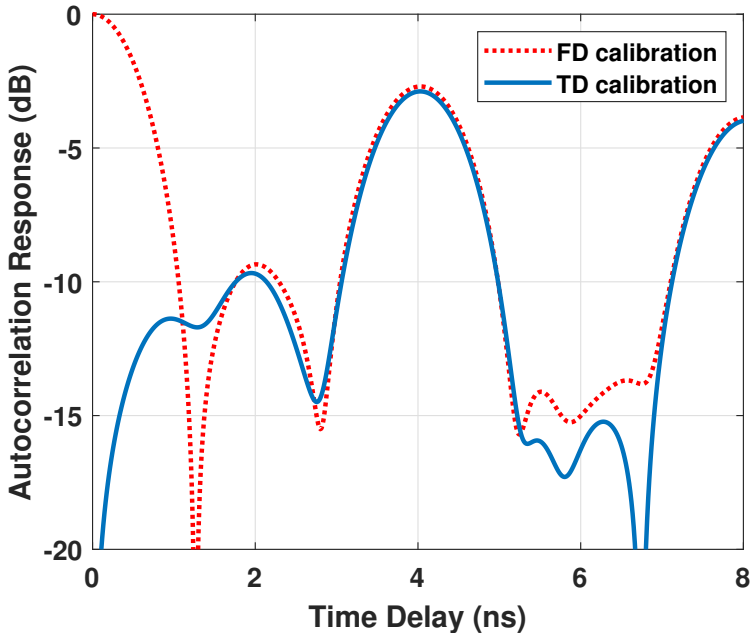

Figure 3.7: ACF of the secne simulator with two 10 dB couplers and coaxial cables of 50 cm using FD and TD calibrations.

3.6 Time domain Calibration of WiBAR Enhanced with a Comb Filter

In this section we calibrated a WiBAR setup with a comb filter on a test bench.

3.6.1 Simulation Results of WiBAR Calibration with the Ideal Comb Filter

A schematic diagram of the ideal comb filter is shown in Fig. 3.8. The comb filter is a four port microwave circuit analog of a Fabry-Perot interferometer (FPI) in optics. The directional couplers in the comb filter play the role of reflectors in a FPI, and a phase shifter in the loop of the filter makes it tunable (*Mahapatra and Mattoo*, 1986; *Coale*, 1956; *Salim et al.*, 2020).

The frequency response of an ideal new comb filter, which has a flat pass-band response, with many evenly spaced alternating pass and stop bands, is shown in

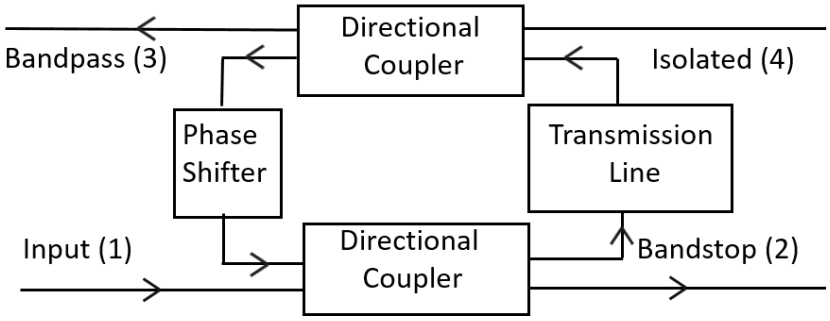

Figure 3.8: Schematic diagram of the new ideal comb filter which consists of two directional couplers, phase shifter, and transmission lines.

Fig. 3.9.

Figure 3.10 and figure 3.11 show the autocorrelation function for both TD-WiBAR and FD-WiBAR for a 36.8 cm thick ice on Douglas Lake, MI. The time delay at 6.5 ns is detectable in the ACF for both TD and FD calibrations and the two calibrations are in good agreement. Implementing the comb filter for RFI mitigation does not affect the calibration.

3.6.2 Circuit Design of the WiBAR Setup with the Comb Filter

A block diagram of the simple microwave circuit model of the WiBAR Sensor with a comb filter is shown in Fig. 3.12. In this instrument, the autocorrelation function (ACF) is generated by an inverse Fourier transform of the power spectral density from 0.5 to 2.5 GHz acquired with a Keysight spectrum analyzer. Thus, we can test the performance of the TD-WiBAR calibration with a comb filter using a spectrum analyzer as the receiver. In this demonstration of the WiBAR calibration RFI is not added.

The radiometer front-end includes a low noise amplifier, power amplifiers, and a calibration switch to ambient load and a cold-FET load (*Frater and Williams*, 1981). A scene simulator is a microwave circuit that simulates layered media as depicted in Fig. 3.4.

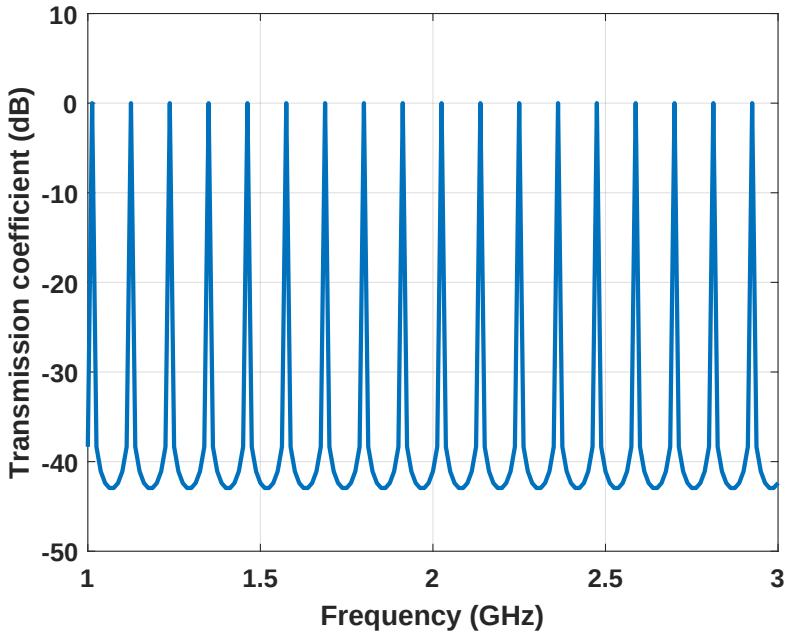

Figure 3.9: Transmission coefficient of an ideal comb filter w.r.t. to frequency. The filter is made from two 20 dB couplers, and loop length of 2.66m, and has a loop gain of unity.

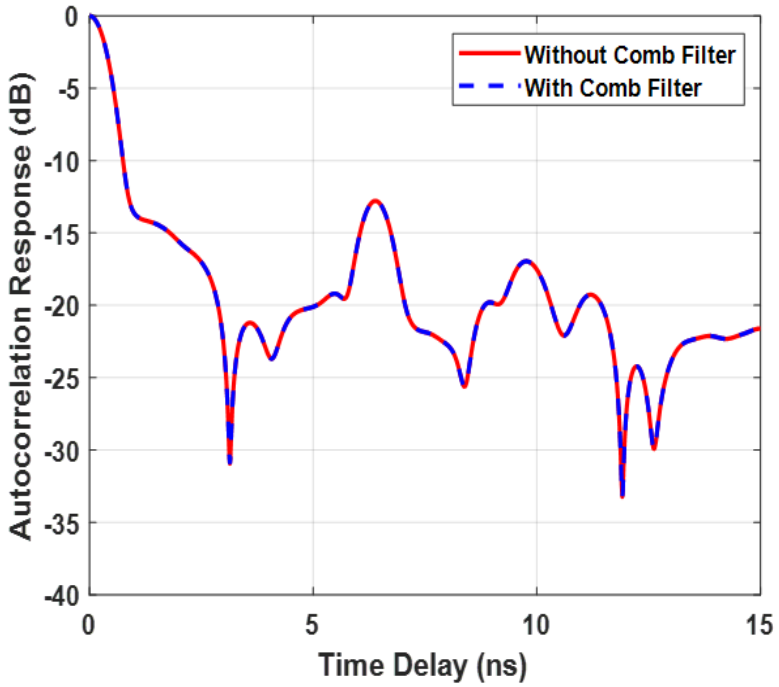

Figure 3.10: ACF of the lake ice with a thickness of 36.8 cm using FD-calibrations for cases in which the WiBAR includes a comb filter and without comb filter.

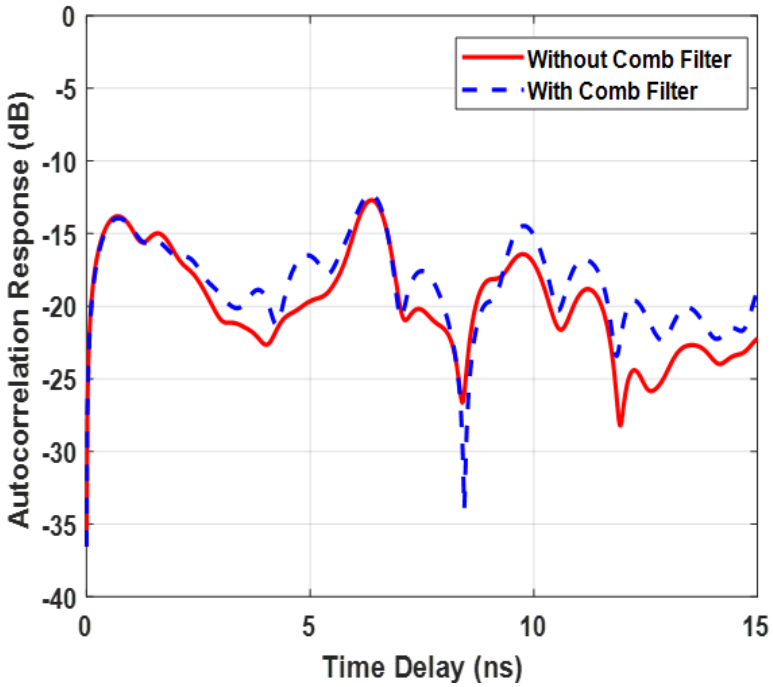

Figure 3.11: ACF of the lake ice with a thickness of 36.8 cm using TD-calibrations for cases in which the WiBAR includes a comb filter and without comb filter.

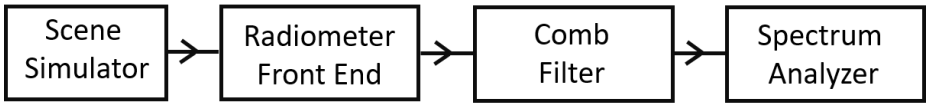

Figure 3.12: Block diagram simulated set-up of the simple WiBAR instrument Enhanced with a comb Filter.

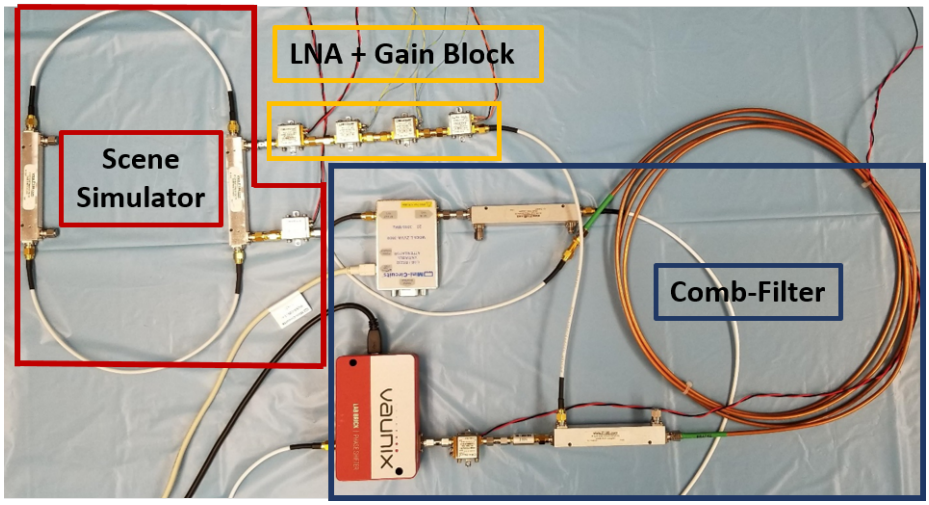

Figure 3.13: Laboratory set-up of the WiBAR with a scene simulator, radiometer front-end, and a comb filter for RFI mitigation.

Figure 3.13 shows the set-up of the microwave circuit of WiBAR. The scene simulator includes two 10 dB couplers, P1dB-P1CP-SAF-R502G, and coaxial cables of 31 cm and a low noise amplifier, Mini-Circuits ZX60-P33ULN+, representing the sky. We used a Mini-Circuits ZX60-P105LN+ as the LNA in the radiometer front-end and a comb filter with a 3 m long semi-rigid coaxial cable.

3.6.3 Hardware Implementations and Measurement Results

In Fig. 3.6 the measurement results of the spectrum for the scene simulator, load, and cold-FET without comb filter is shown. Then we added the comb filter to the set-up and repeated the measurements. In Fig. 3.14, measurement results of the three targets with a comb filter are shown.

The autocorrelation response of time and frequency domain calibration for measured power spectrum with and without comb filter is shown in Fig. 3.15.

The time delay at 4 ns is detectable in the ACF for both TD and FD calibrations, and the two calibrations are in good agreement. These results show that implementing the comb filter for RFI mitigation does not affect either the FD or TD calibration,

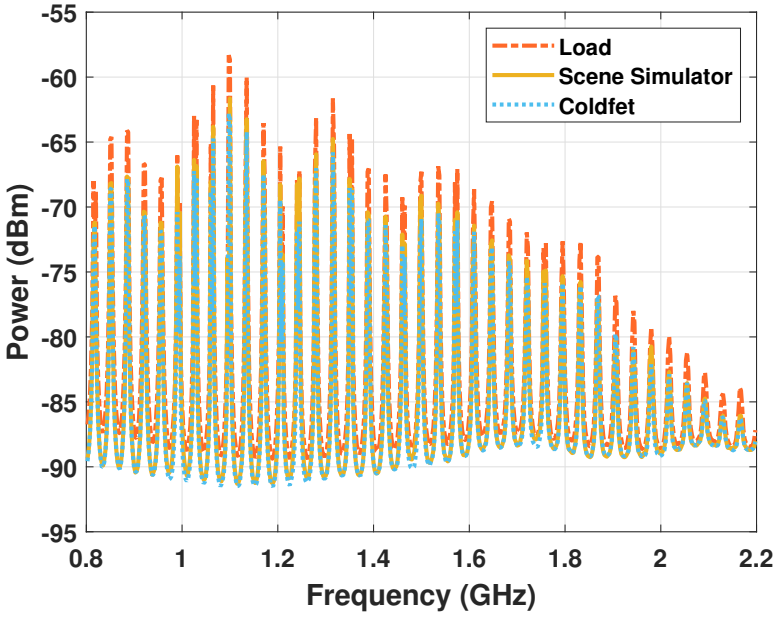

Figure 3.14: Measurement results at the output of the comb filter, with the load, cold-FET, and scene simulator as input to the RF front end. Measurements are done using a Keysight spectrum analyzer.

The TD-WiBAR calibration is constructed such that the ACF peak at zero lag is removed from the ACF, which has an additional advantage in that sidelobes of the impulse response does not contribute to the noise floor, potentially masking weak signals.

The large peak near 8 ns is the correlation of the direct ray with a doubly-delayed ray that went around the scene simulator loop twice. The comb filter also imposes a correlation on the ACF. With transmission lines in the comb filter at least twice as long as in the scene simulator, the correlations imposed by the comb filter do not appear in the ACF region of interest shown in Fig. 3.15. The spectral spacing of 36 MHz shown in Fig. 3.14, the comb filter's correlations occur at multiples of 27 ns.

Results show that the scene simulator circuit's lag time is detectable in the ACF for both TD and FD calibrations, both with and without the comb filter, and that the two calibrations are in good agreement.

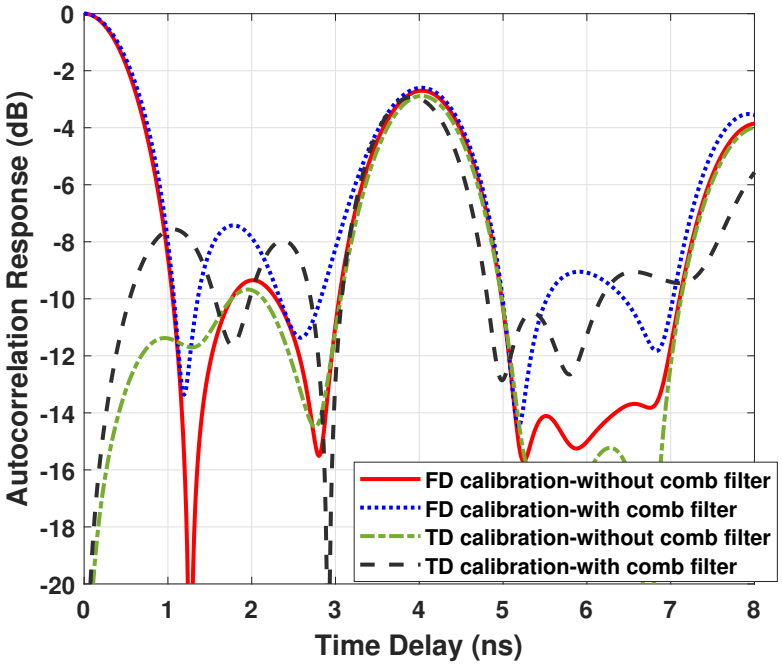

Figure 3.15: ACF of the secne simulator with two 10 dB couplers and coaxial cables of 40 cm using FD and TD calibrations for cases in which the WiBAR includes a comb filter and without comb filter.

3.7 RFI Mitigation in TD-WiBAR Using a Comb Filter

3.7.1 Simulation Results of the RFI Mitigation Using the Ideal Comb Filter

The emitted brightness spectrum, $T_B(f)$, received by WiBAR can be described by (*Mousavi et al.*, 2018)

$$T_B(f) = T_p\overline{e}/(1 + 2A_e \cos 2\pi f\tau_d) \tag{3.17}$$

where T_p is the physical temperature of the scene (henceforth assumed to be 273 K), $\overline{e}$ is the mean emissivity over frequency, and A_e is one half of the relative amplitude of oscillation in the spectrum due to constructive and destructive interference caused by the slab at different wavelengths. The received power by the WiBAR, normalized to brightness, is shown in Fig. 3.16. The estimated delay time by WiBAR can be derived by using the inverse fast Fourier transform (IFFT) of the spectrum to produce an autocorrelation function (ACF) (*Mousavi et al.*, 2018) as explained in the earlier sections.

$$\Phi(\tau) = \int \hat{T}_B(f)w(f)e^{-j2\pi f\tau}df \tag{3.18}$$

where $w(f)$ is an appropriate window function (eg. rectangular, Hamming, etc.) to be used used to improve the system sensitivity.

In Fig. 3.17, the spectrum polluted with RFI, which is added in the post-processing part, is shown along with the frequency response of the spectrum multiplied by the frequency domain response of the ideal, but non-optimized, comb filter. By changing the phase of the loop, the pass-band peaks can be tuned over the frequency range for removing the randomly occurring RFI.

In particular, the phase is adjusted to minimize the power out of the comb filter. As it is shown in Fig. 3.18, when optimized, the RFI falls into the reject bands of the

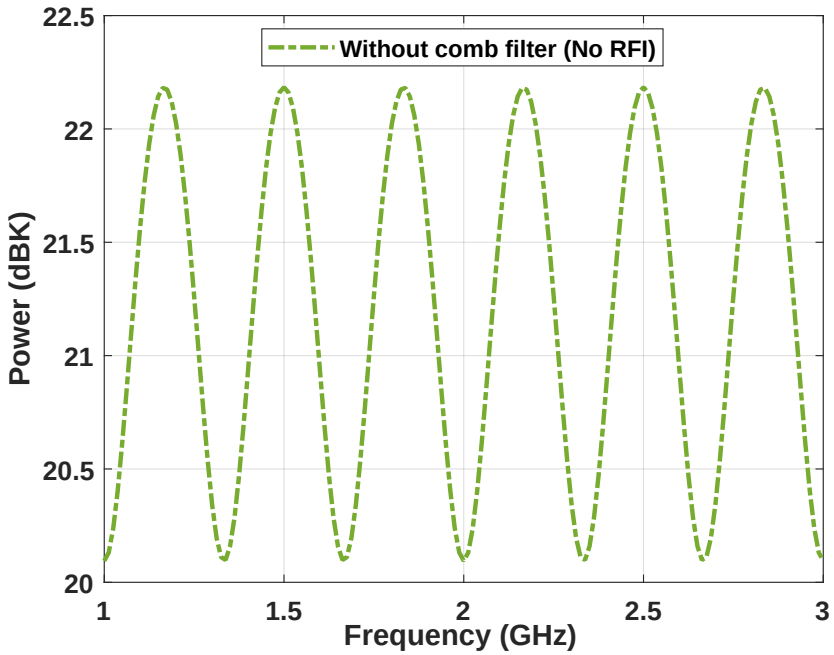

Figure 3.16: Simulated emissivity with no RFI signals and without applying the comb filter.

filter.

As shown, applying the optimized comb filter to the polluted received power can reduce the RFI amplitudes by more than 40 dB.

For a layer of ice with 25 cm thickness, the autocorrelation response should have a peak at 3 ns. Figure 3.19 shows the ACF in four different cases. In the first case, the ACF is created without RFI, and the peak appears at 3 ns as expected.

The second case is an ACF for a spectrum polluted with random RFI, but without applying the proposed comb filter, demonstrating that the peak is not detectable because it is below the increased noise floor due to the RFI.

The third curve is the ACF when the non-optimized comb filter is applying to the polluted spectrum with RFI.

As it is shown in the figure, the ACF peak is not detectable, because the RFI was not sufficiently removed.

The last curve shows the ACF result when an optimized comb filter is applied to

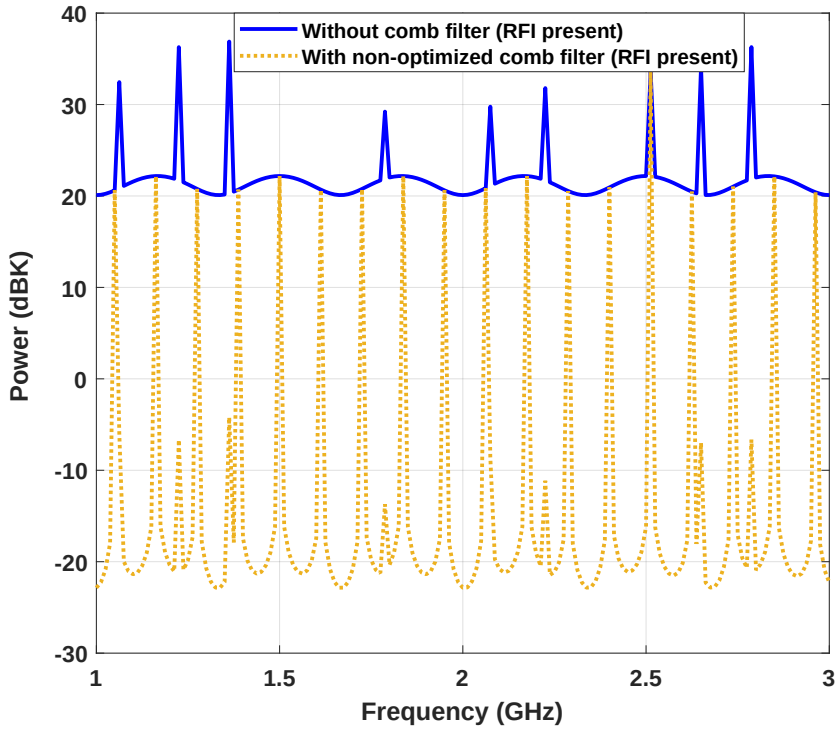

Figure 3.17: Simulated polluted spectrum with RFI signals (blue curve) and polluted spectrum after applying the non-optimized comb filter (yellow curve).

a spectrum with has random RFI.

It is shown that applying the comb filter reduces the RFI in the spectrum and the SNR of the autocorrelation function is more than 8 dB and at 3 ns the peak is detectable (*Salim et al.*, 2020b).

Simulation results shows that applying the comb filter results in clear detection of the layer thickness using the WiBAR method, while without using a comb filter, RFI increases the noise level and the thickness of the layer cannot be measured.

3.7.2 Circuit Design and Hardware Implementation

Figure 3.21 shows the set-up of the microwave circuit of WiBAR. The scene simulator includes two 10 dB couplers with the length of 9 cm, and coaxial cables of 31 cm and a low noise amplifier, representing the sky. We used a Mini-Circuits

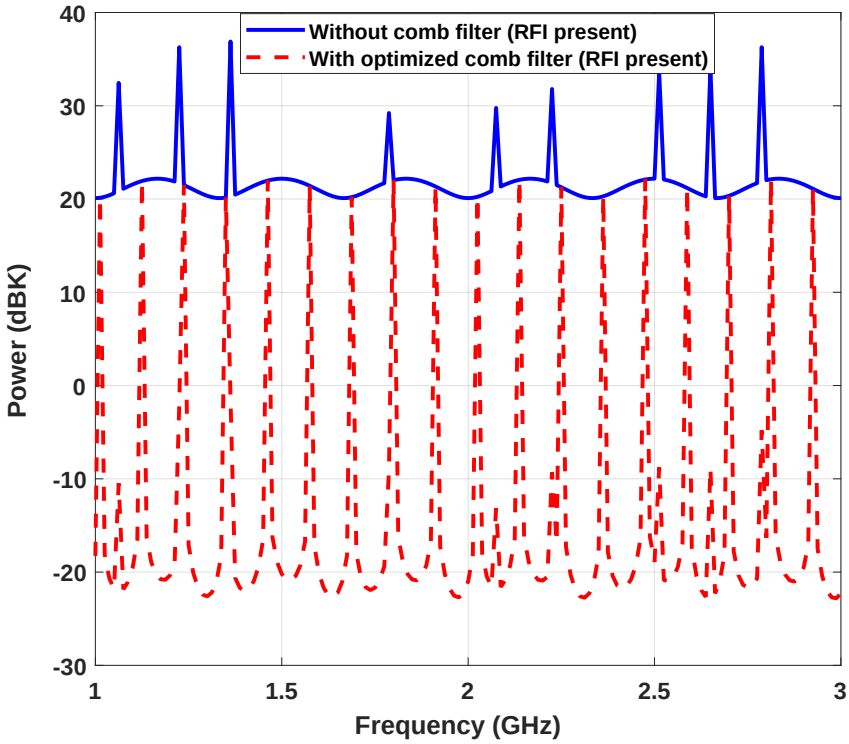

Figure 3.18: Simulated polluted spectrum with RFI signals (blue curve) and polluted spectrum after applying the optimized comb filter (red curve).

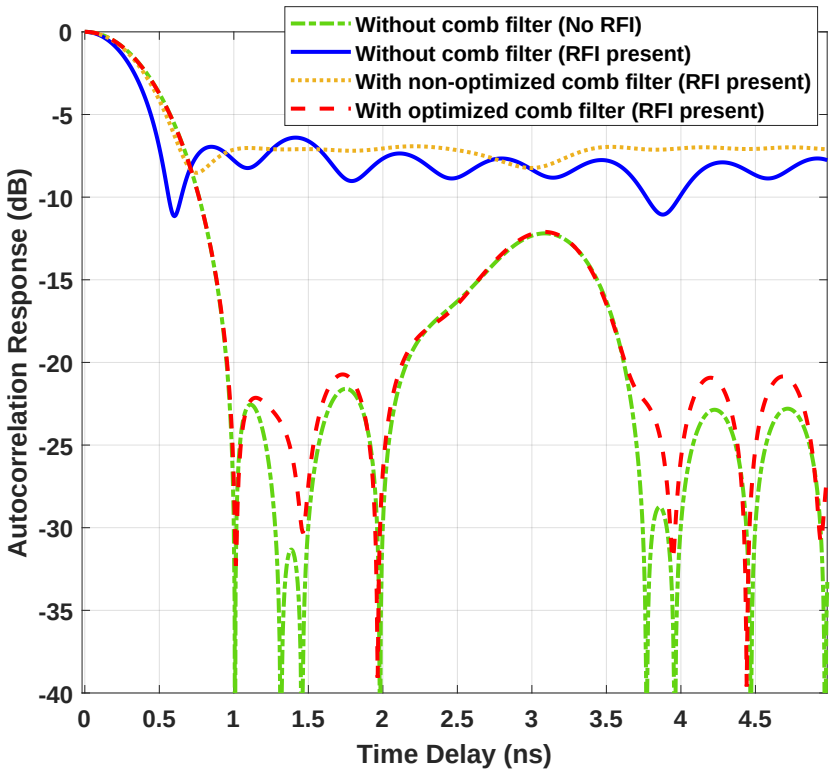

Figure 3.19: ACF of the simulated spectrum of the lake icepack with a thickness of 25 cm for signal without RFI and polluted spectrum with RFI, and applying optimized and non-optimized comb filter to the polluted spectrum with RFI and with out applying filter. The expected value of the autocorrelation response is 3 ns. Hamming window was used to reduce the side-lobes.

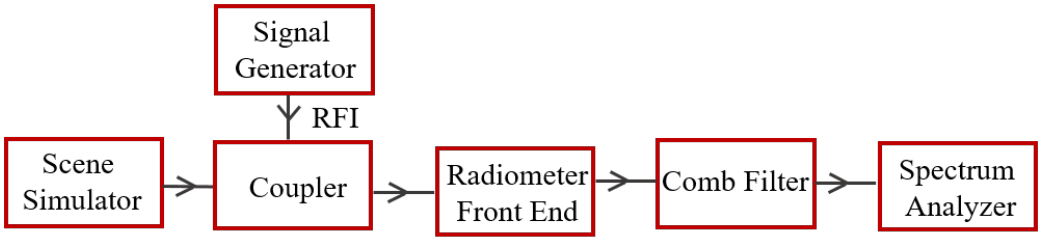

Figure 3.20: Block diagram of the simple WiBAR instrument Enhanced with a comb Filter with RFI injection using a signal generator.

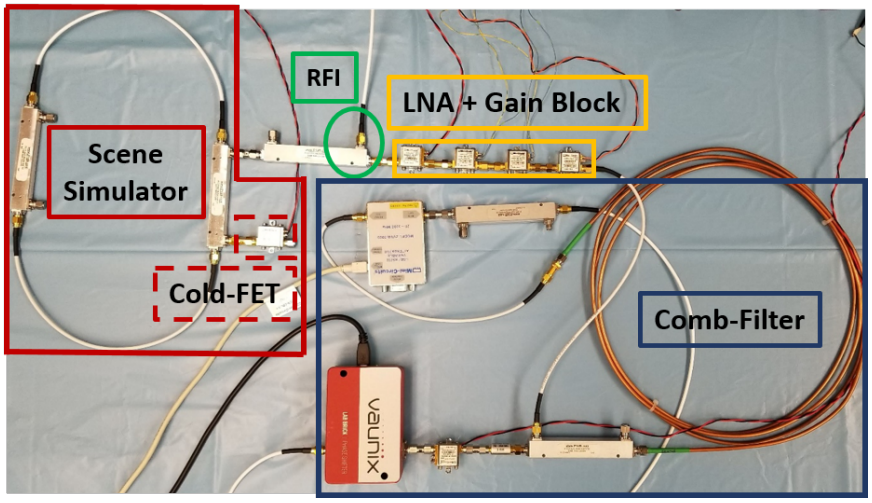

Figure 3.21: Laboratory set-up of the WiBAR with a scene simulator, radiometer front-end, RFI signal, and a comb filter for RFI mitigation.

ZX60-P105LN+ as the low noise amplifier (LNA) and three 13 dB amplifiers in the radiometer front-end and a comb filter with two 20 dB couplers and a 3 m long semi-rigid coaxial cable. The high-power RFI generated with a signal generator is added to the radiometer front-end using a directional coupler to inject the RFI signal to the receiver. Table 3.1 shows the detailed specifications of the components. Fig. 3.20 shows the block diagram of the microwave circuit of WiBAR enhanced with the comb filter and while a high power RFI signal is added to the measured spectrum.

We added a high power RFI signal to the spectrum. Figure 3.22 shows the polluted spectrum with RFI. Then we applied a comb filter to suppress the RFI signal.

Applying optimize and non-optimized comb filter to the polluted spectrum with

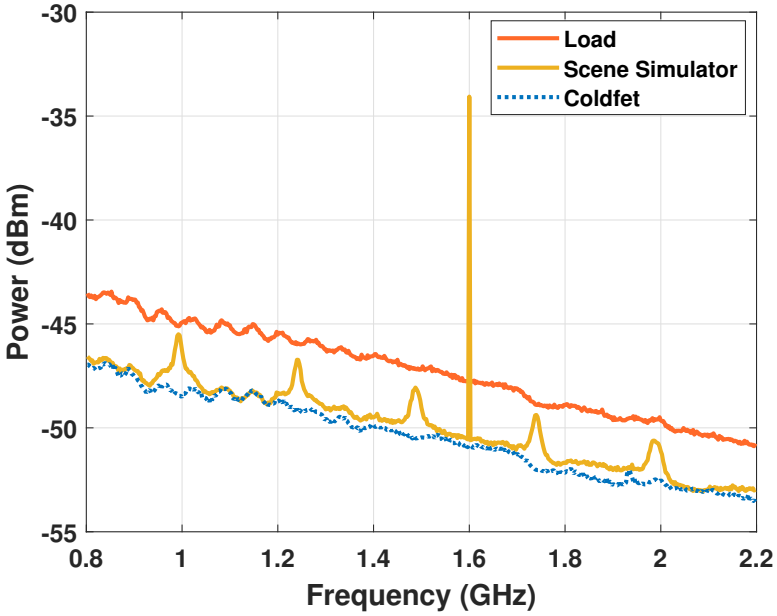

Figure 3.22: Measured spectrum for the load, cold-FET, and scene simulator with RFI. The RFI signal is applied using a hp digital signal generator series ESG-D4000A.

RFI is shown in Fig.3.23. By changing the phase of the loop, the pass-band peaks can be tuned over the frequency range for removing the randomly occurring RFI. In particular, the phase is adjusted to minimize the power out of the comb filter. Figure 3.23 b, is when the optimized comb filter is applied to the spectrum, the RFI falls into the reject bands of the filter. Therefore, applying the optimized comb filter to the polluted received power can reduce the RFI amplitudes by more than 20 dB.

Figure 3.24 shows the ACF in four different cases. In the first case, the ACF is created without RFI, and when we do not have a comb filter in the set-up, and the peak appears at 4 ns as expected.

The second case is an ACF for a spectrum polluted with a high power RFI, but without applying the comb filter, indicating that the peak is not detectable.

The third curve is the ACF when the non-optimized comb filter is applying to the polluted spectrum with RFI. The ACF peak is not detectable in this case, because the RFI is not sufficiently removed.

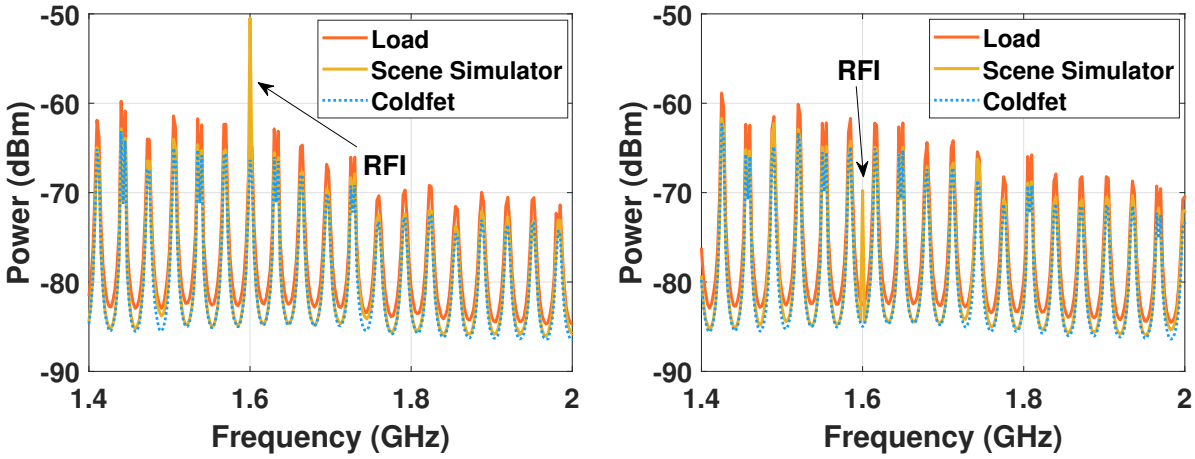

Figure 3.23: Measured spectrum for the load, cold-FET, and scene simulator polluted with RFI, after applying the a) non-optimized and b) optimized comb filter.

The last curve shows the ACF result when an optimized comb filter is applied to a spectrum with the RFI. It is demonstrating that applying the comb filter eliminates the RFI in the spectrum and the SNR of the autocorrelation function is more than 8 dB and at 4 ns the peak is detectable.

3.8 Conclusion

A wideband autocorrelation radiometer is an instrument that passively measures the thickness of a dielectric layer by finding the propagation delay of multipath thru the layer. In this chapter an alternate calibration of a WiBAR, the time-domain WiBAR is proposed, which enables more rapid data acquisition than the previous frequency-domain WiBAR.

A WiBAR instrument with a scene simulator circuit is set up in the laboratory in order to produce data with which to test the calibration algorithms. A scene simulator is a microwave circuit consists of directional couplers and transmission lines representing the multilayer structure of the soil-snow-air. Results show that the scene simulator circuit's lag time is detectable in the ACF for both TD and FD

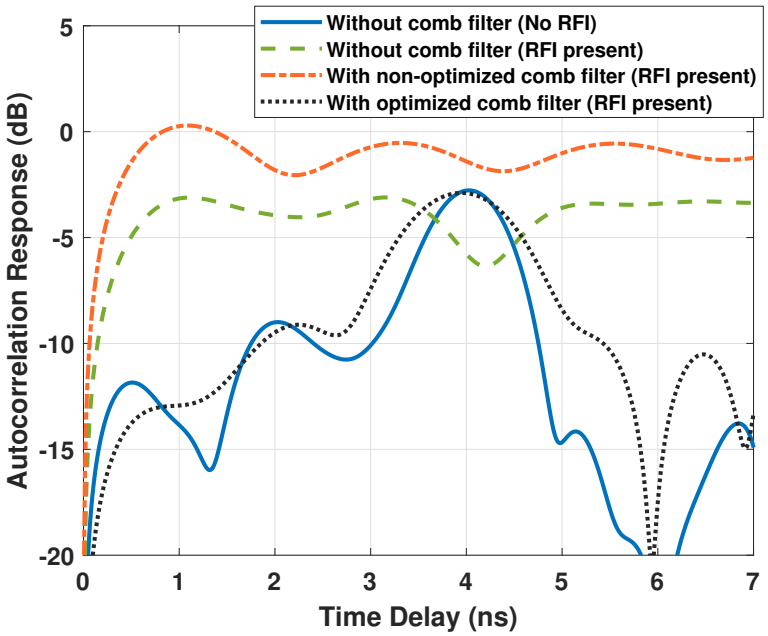

Figure 3.24: ACF of the measured spectrum of scene simulator with a loop length of 80 cm, (two 9 cm couplers and two 31 cm coaxial cables) for without applying RFI signal and polluted spectrum with RFI, and applying optimized and non-optimized comb filter to the polluted spectrum with RFI and with out applying filter. The expected value of the autocorrelation response is 4 ns.

calibrations, the two calibrations are in good agreement.

Being broadband, a WiBAR is susceptible to receiving radio frequency interference. This chapter also addresses a new approach for RFI suppression in WiBAR which uses a comb filter for the mitigation of RFI. RFI in WiBAR results in increased noise in the observation and decreases WiBAR's ability to detect the thickness of the ice or snow layer.

The comb filter has a pattern with many alternating band-pass and band rejection frequencies and the tunability for scanning through frequency makes it suitable for RFI mitigation. Results show that applying an optimized comb filter to the collected power spectrum can suppress the available RFI and the peak of the autocorrelation function is detectable in the presence of a high power RFI signal.

CHAPTER IV

Snowpack Remote Sensing using Wideband Long-Wavelength Microwave Radiometry (WiBAR- UWBRAD)

4.1 Introduction

The potential future impacts of climate change are of increasing concern. Impacts on ecosystems could potentially affect the capacity of natural systems to produce water resources for industrial and agricultural purposes (*Serreze et al.*, 2000). Cryospheric elements like snow cover are an indicator of global change and play an essential role in providing water supplies for numerous parts of the globe. Remote sensing information on snow water equivalent (SWE) and snowpack thickness serve as important water resource availability markers. To provide accurate resource monitoring, improvements in methods for remote sensing snow properties are required (*Milly et al.*, 2008).

Microwave radiometry measures the microwave emission from a layer of snow and ice. Measurements at long wavelengths minimize volume and surface scattering effects within the snowpack. As a result, the thermal emission from a layer of snow can experience multiple reflections in the layer.

The 0.5-2.0 GHz Ultra-Wideband Software-Defined Radiometer (UWBRAD)

(*Andrews et al.*, 2018), and the 1.0-2.0 GHz Wideband Autocorrelation Radiometer (WiBAR) (*Mousavi et al.*, 2018) exemplify instruments that can measure the snow properties like snow depth, dielectric properties.

This chapter reports snowpack measurements by The Ohio State University's UWBRAD and the University of Michigan's WiBAR deployed at the Keweenaw Research Center (KRC) near Houghton, MI from February 2020 to May 2021, where the snow reached 60 cm depth (*De Roo et al.*, 2020).

These two instruments are complementary in that UWBRAD has robust radio frequency interference detection, while WiBAR has a narrower beamwidth. The goal of these measurements is to recover the microwave propagation time for different thicknesses and to measure the brightness temperature of the snow layer.

4.2 Theory of WiBAR and UWBRAD

The concept of wideband autocorrelation radiometry (WiBAR) has been proposed as a radiometric technique for the remote sensing of snow and ice layers. Thermal emission from the ground under the snowpack propagates up through the snowpack to the receiver. The reflection of the upward traveling wave from first the upper and then the lower surface of the snowpack results in creating another ray. An observing antenna can receive both these waves, which are identical except for their amplitude and the time lag associated with the extra transit through the snowpack. Unlike the scatter darkening approach to the passive microwave remote sensing of snow depth (as used with 19-37 GHz brightness temperature measurements), WiBAR uses a direct method to remotely measure the propagation time delay, τ_d, and thus the thickness of the layer (*Mousavi et al.*, 2018), with

$$\tau_d = \frac{2d}{c}\sqrt{n_{snow}^2 - \sin^2\theta} \tag{4.1}$$

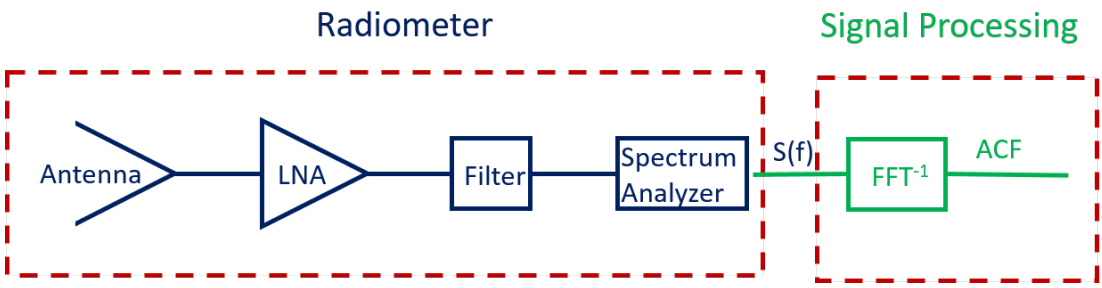

Figure 4.1: Hardware instrument of WiBAR.

where d is the thickness of the layer, c is the speed of light in free space, n_{snow} is the refractive index of the slab, and θ is the incidence angle (*Evans*, 1965).

An estimate of the refractive index of the dry snowpack can be obtained by from the empirical relationship:

$$n_{snow} = \begin{cases} \sqrt{1 + 1.9\rho_s} \ for \ \rho_s \leq 0.5 \ g.cm^{-3} \\ \\ \sqrt{0.51 + 2.88\rho_s} \ for \ \rho_s \geq 0.5 \ g.cm^{-3} \end{cases} \tag{4.2}$$

where ρ_s is the density of dry snowpack. The delay time can be estimated by performing an inverse fast Fourier transform (IFFT) of the emissivity spectrum $e(f)$ to produce an autocorrelation function (ACF).

$$\Phi(\tau) = \int e(f)w(f)e^{-j2\pi f\tau}df \tag{4.3}$$

where $w(f)$ is an appropriate window function used to improve the system sensitivity. In the autocorrelation function, in addition to a large peak at zero lag, which is the correlation of the direct ray with itself, there is a lag peak due to the correlation of the delayed ray with the direct ray. This non-zero lag peak of the ACF has a local maximum at $\tau = \tau_d$. Figure 4.1 shows the instrument concept of WiBAR.

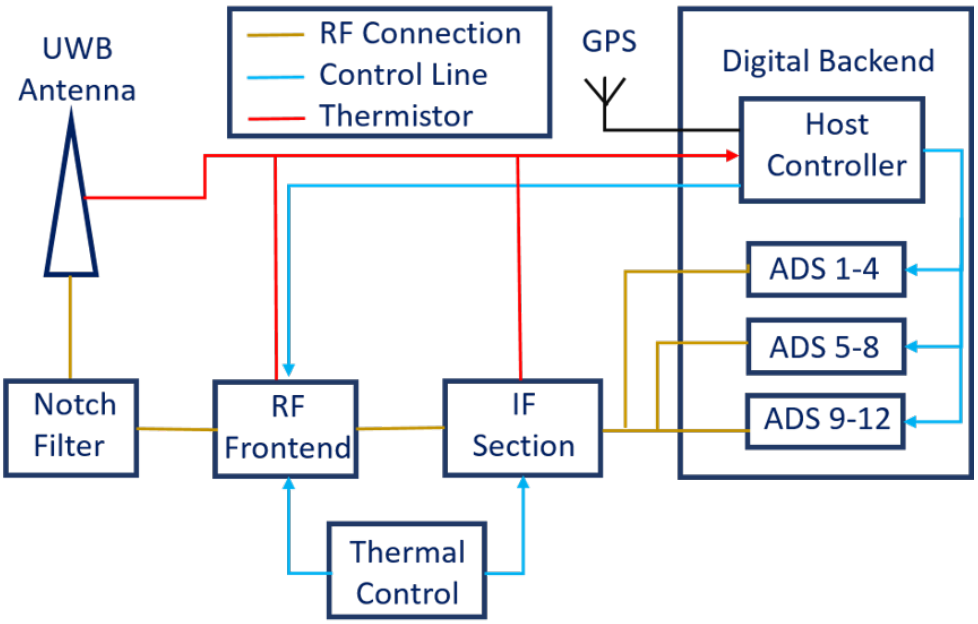

Figure 4.2: Hardware instrument of UWBRAD.

Radio frequency interference (RFI) within WiBAR's frequency of operation can reduce the ability of WiBAR to measure the layer's thickness accurately by raising the ACF noise floor. While there is no universal RFI mitigation method, RFI suppression may be implemented as part of the data processing.

The frequency of operation of UWBRAD is 0.5-2 GHz, and it has the capability of identifying and mitigating RFI through software-defined algorithms in real-time and post-processing of the acquired data (*Andrews et al.*, 2018). The hardware of UWBRAD as shown in Fig. 4.2, includes an ultrawide bandwidth conical spiral antenna with a protective radome.

The IF down conversion units divide the operation frequency band of UWBRAD into ten 81-MHz bandwidth and two 60-MHz channels. The analog-to-digital back end acquires data and processes it for RFI. Due to the wide bandwidth operation of both WiBAR and UWBRAD, many RFI types are expected.

The RFI detection algorithms of UWBRAD are applied in the time, frequency, and statistical domains similar to the methods used in the SMAP microwave radiometer

(*Piepmeier et al.*, 2014) which can be divided into two levels of RFI detection:

- Level 1: time-domain algorithms using full-band products to flag short pulsed and non-Gaussian RFI.
- Level 2: sub-band Kurtosis algorithms to flag any frequency-dependent RFI.

We use the RFI flags provided by the UWBRAD pulse and subband kurtosis detection algorithms to clean up the power spectrum measured by WiBAR prior to deriving the autocorrelation function, in order to estimate the snow depth more accurately.

4.3 Field Measurements and Data Collection

WiBAR and UWBRAD were installed on the University of Michigan's truck with the truck deployed at the Keweenaw Research Center (KRC) near Calumet in the Upper Peninsula of Michigan to measure the seasonal snowpack. Figure 4.3 shows the location of the truck and a photo of the experimental set-up at KRC.

The experiment's objective was to obtain evidence of the interference signal in a seasonal snowpack using the RFI information from UWBRAD. The snowpack was at least 58 cm deep, enough for a WiBAR signal to be observable given the system's frequency span. Throughout winter 2020, the temperature was below 0°C, indicating that snow was cold and dry enough for microwaves to propagate through the snowpack with at most mild attenuation.

Figure 4.4 shows the WiBAR and UWBRAD instruments installed on the truck.

UWBRAD measurements were made continuously. WiBAR measurements were performed early in the morning when conditions were expected to be coldest and driest. The systems were set to stare at the undisturbed field at fixed incidence angles ranging from 56° to 70°. Figure 4.5 depicts time series emissivities from WiBAR that we used to match up with the channels of the UWBRAD radiometer and the ground

Figure 4.3: a) Location and field of view of the truck b) The L-band WiBAR and UWBRAD deployed at the Keweenaw Research Center, Winter 2020.

measurements including air temperature and ground temperature as the time series measurements over there.

Figure 4.6 shows the power spectrum measured by WiBAR and the RFI signal using the pulse and kurtosis detection methods measured by UWBRAD.

4.4 Data Post Processing

4.4.1 Winter 2020

Figure 4.7a shows the measurements of February 22nd at 7:00 am as a representative example of data when the snow was deep and the weather was cold. It includes the measurements of cold-FET and load for calibration purposes and of the snow layer. The yellow curves indicate the measurements of the snow layer below 1.1 GHz suffer from large amounts of RFI compared to higher frequencies.

In order to clean up the spectrum, we removed the samples of the spectrum when the pulse detection algorithm indicates more than 20% of measurements include RFI. In Fig. 4.7b the spectrum after applying RFI mitigation techniques is shown.

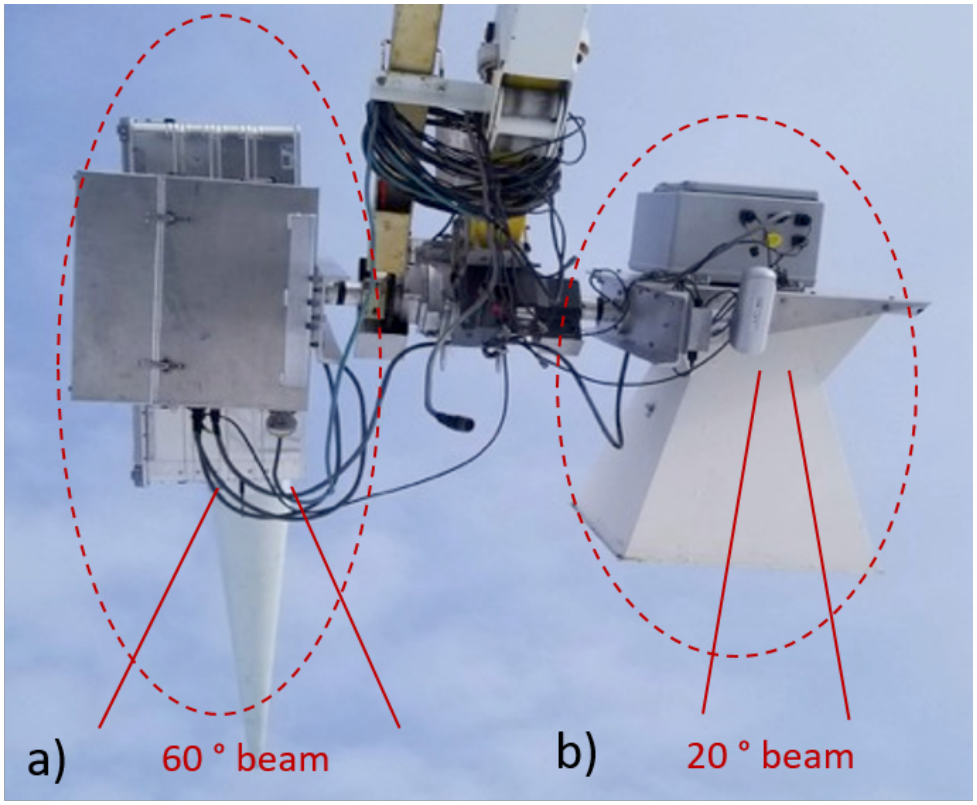

Figure 4.4: Measurement set up at Keweenaw Research Center (KRC), Winter 2020. a) UWBRAD b) WiBAR.

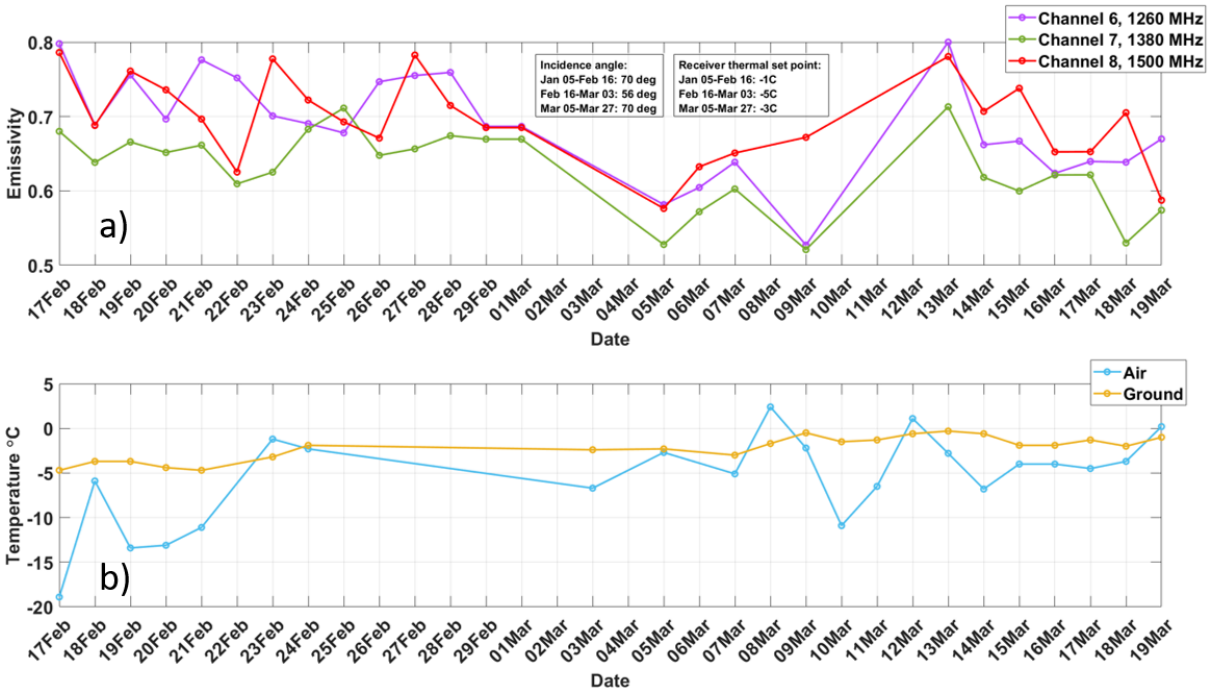

Figure 4.5: Time series measurements of emissivity during Winter 2020, a) WiBAR data matched to UWBRAD Channels b) Ground measurements of temperature.

According to Eq. 4.1 and Eq. 4.2, a 60 cm deep dry snow pack with mean density of 300 kg/m^3 creates a lag time close to 3.76 ns in the ACF.

The autocorrelation response at incident angle $\theta = 56°$ obtained from the measured emissivity spectra using the Hamming window function,before and after applying RFI mitigation is shown in Fig. 4.8. According to the ACF, the measured time delay occurs at τ_d =3.89 ns, which corresponds to 62 cm of snow depth. The measured thickness is around 2 cm different from the ground truth value of the snow depth. We believe that the larger peaks in the ACF are the instrument response. We are working on removing this instrument response and on decreasing the noise floor. The COVID pandemic has prevented us from accessing the instrument to confirm this hypothesis.

In order to remove the peak at the zero lag and its side lobe, the time domain calibration is applied to create the ACF response. Fig. 4.9 shows the TD and FD calibration applied to the measured data of 22nd of February 2020. Time-domain calibration removes the large peak and the zero lag. However, the expected peak is

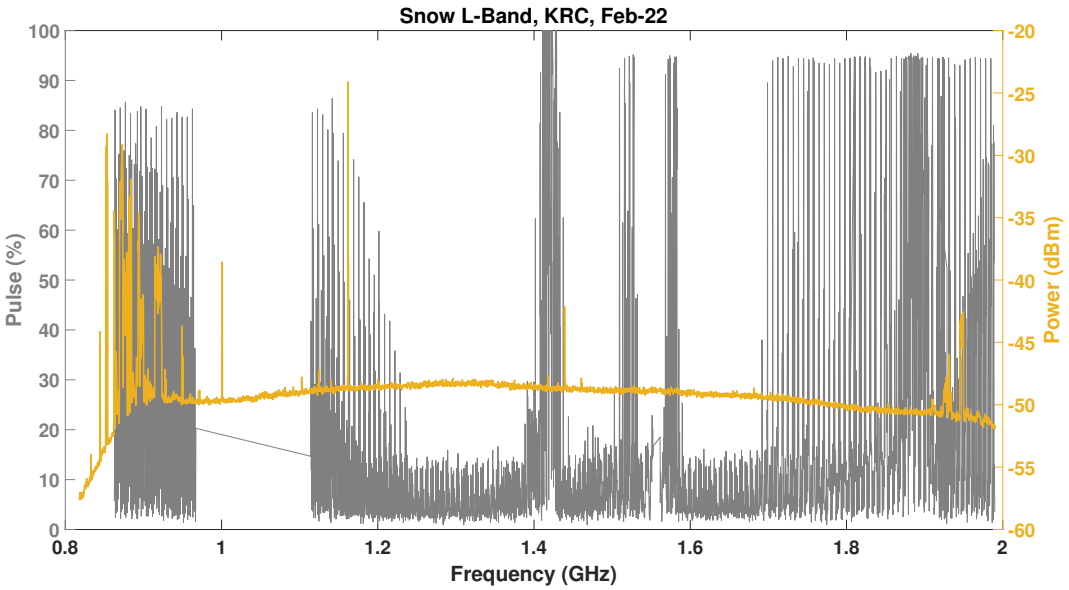

(a)

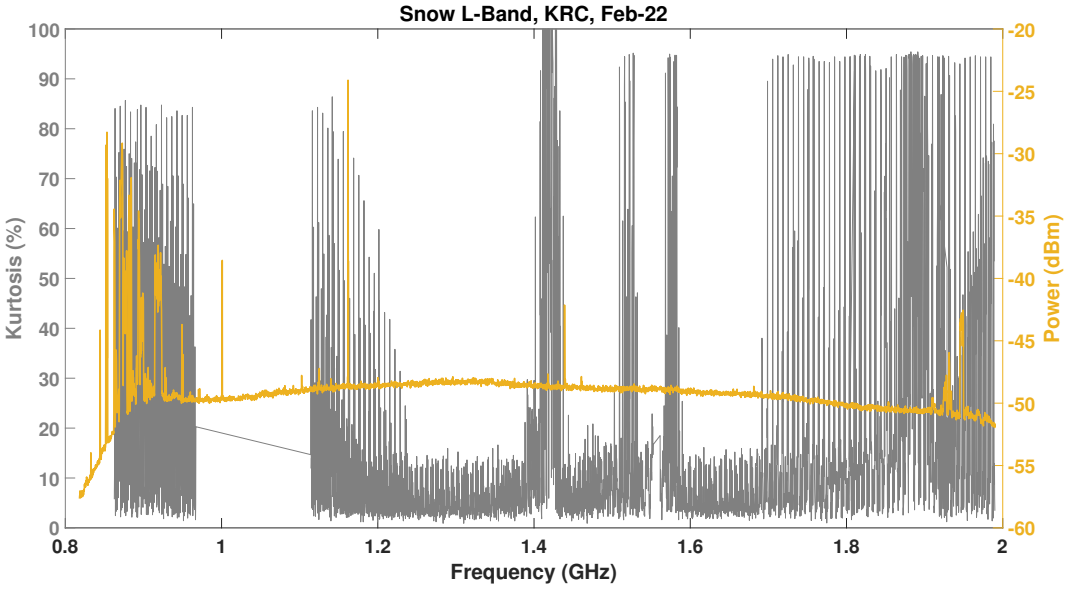

(b)

Figure 4.6: Power spectrum measured by WiBAR, RFI signal using a) pulse detection and b) kurtosis detection method measured by UWBRAD.

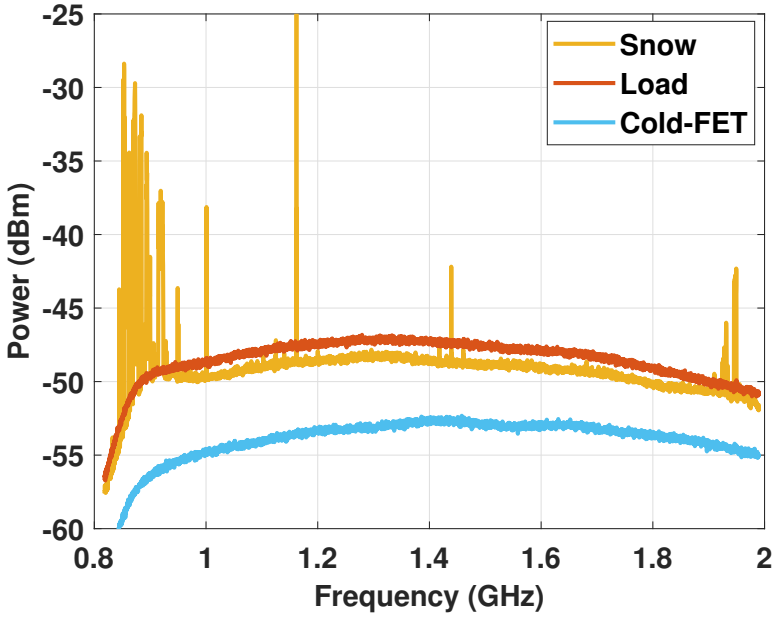

(a)

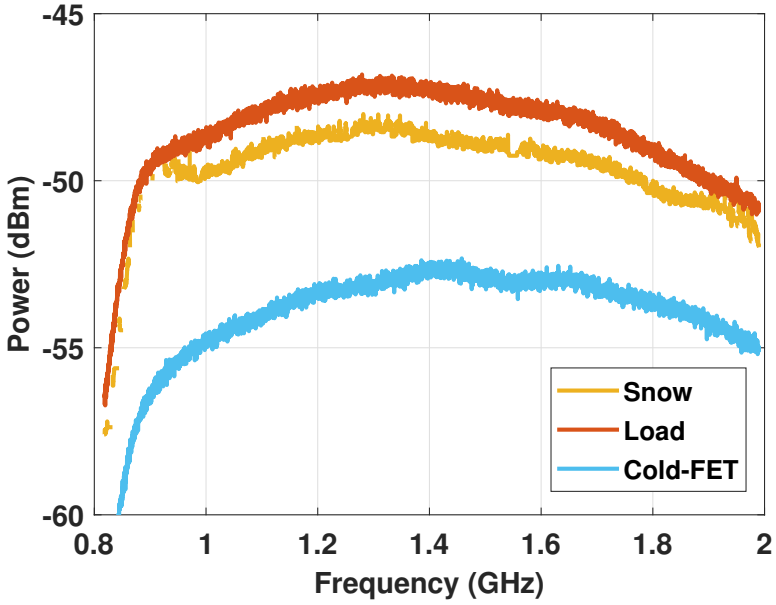

(b)

Figure 4.7: Measurements at Keweenaw Research Center on February 22, 2020. The incidence angle is $\theta = 56°$. a) Cold-FET, load, and snow layer power spectrum. b) Cleared power spectrum of RFI.

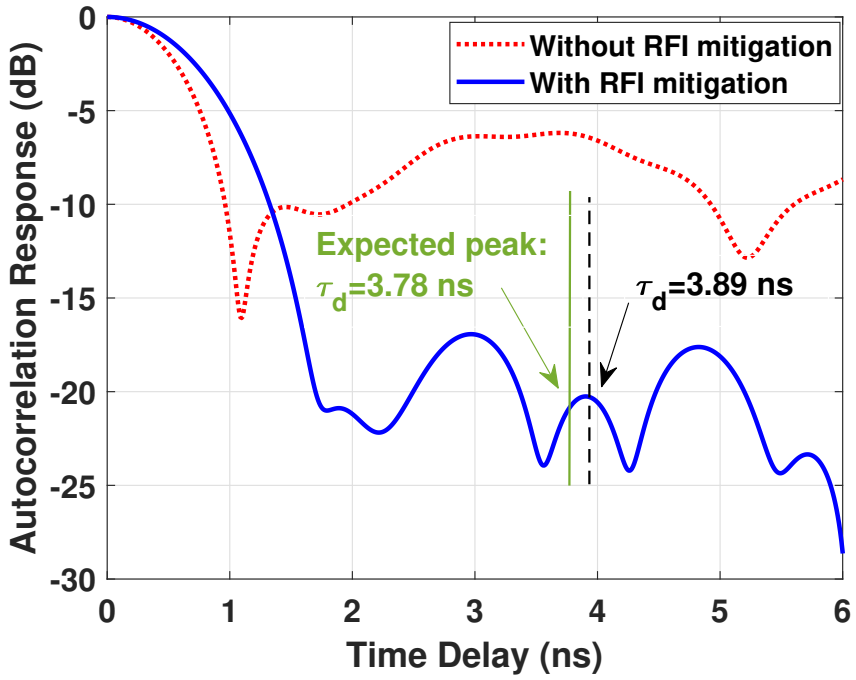

Figure 4.8: The autocorrelation function of the snow layer measured at $\theta = 56°$ with RFI (blue solid line) and without RFI mitigation (red dashed line) at Keweenaw Research Center on February 22, 2020. The Hamming window was used.

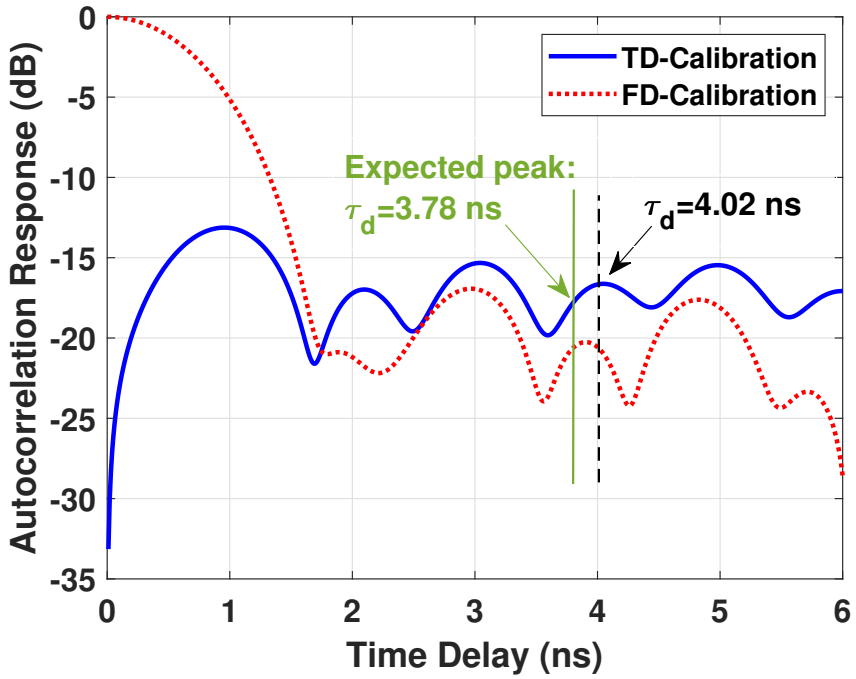

Figure 4.9: The autocorrelation function of the snow layer measured at $\theta = 56°$ with TD-calibration (blue solid line) and FD-calibration (red dashed line) at Keweenaw Research Center on February 22, 2020. The Hamming window was used.

still at the level of the noise floor.

4.4.2 Winter 2021

The Covid pandemic hit shortly after the deployment of systems at KRC. Therefore, we have been unable to return to the field site to acquire ground truth, collect external calibration data for the instruments, or perform maintenance. As such, the data set collected has limited utility. Also, on the L-band WiBAR receiver we lost thermal control on 2020 March 25 and communication with the UWBRad instrument, but we could still communicate with the L-band WiBAR.

Local personnel were able to move the incidence angle from 70 deg to 20 deg as shown in Fig. 4.10, which significantly reduced the apparent RFI, at the expense of increasing the effect of surface roughness. For the WiBAR, we also increased the

Figure 4.10: L-band WiBAR and UWBRad on 2020 Dec 18, at the beginning of the Covid winter. The incidence angle changed to 20°, and the RFI decreased considerably. Photo credit: Bob Baratono, KRC.

number of traces collected from 100 to 1000, in order to reduce the sampling noise.

Figures 4.11 shows the average of raw L-band WiBAR measured Load and ColdFET at the two different times of the day, and in Fig. 4.12 the averaged spectra measured at 20° incidence angle is shown. In Fig. 4.11 the shift between the red and dark yellow curves and the blue and cyan curves show the gain drift due to lack of receiver thermal control but do not impact the calibration of the data. Figure 4.12 shows the improvement in RFI performance compared to the winter 2020 measurements in which the incident angle was 70°. The black curve is the power from the snowpack,

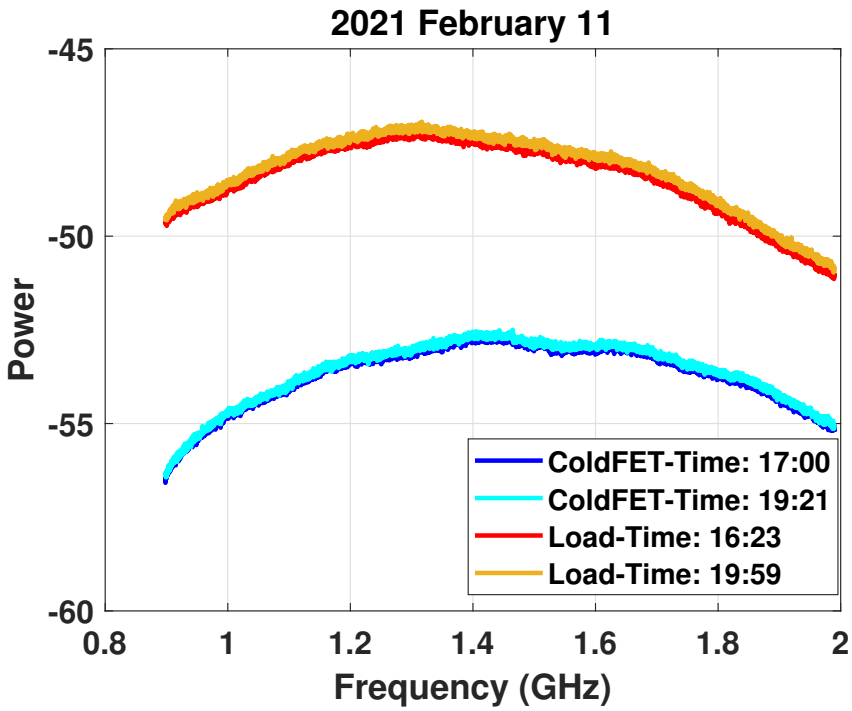

Figure 4.11: Measurements of Load and ColdFET on 2021 Feb 11. The air temperature was -13.3°C and the incidence angle is 20°.

which was 66 cm deep on 2021 Feb 11.

In figures 4.13 and 4.14 the ACF results of the measured spectrum are shown, The results include the measurements of snow on the ground, 09 Feb and 18 January, and when there is no snow on the ground, 18 May and 23 April. According to *England* (2013), for most combinations of snowpack and soil dielectric properties the ratio, $|\Phi(\tau_{del})|/|\Phi(0)|$, for a uniform snowpack will be near 15 dB in the absence of surface roughness, and other causes of scattering, which is not detectable in these measurements.

Figures 4.15, and 4.16 show the comparison of using a different number of traces to generate ACF response of FD-calibration and TD-calibration, respectively. The blue curve shows the ACF response of the averaged spectrum using 1000 traces which has a lower noise floor compering with the other curves. As a result, increasing the number of measurement traces decreases the sampling noise.

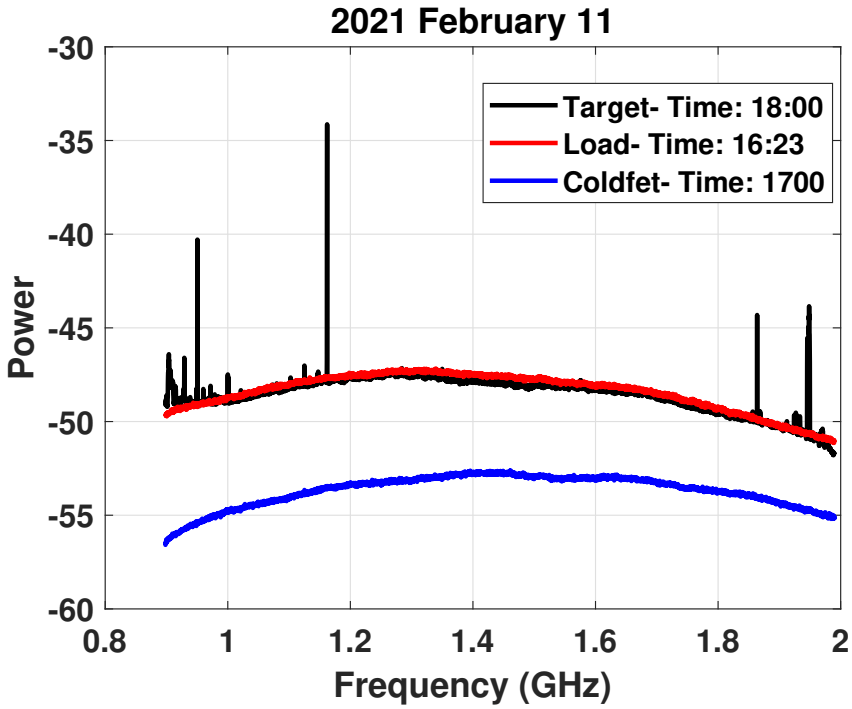

Figure 4.12: Measurements of Load and ColdFET and power spectrum of the snow layer on 2021 Feb 11. The incidence angle is 20°.

4.4.3 A New Frequency Domain Calibration

In this section, a new frequency domain calibration is derived to include the variation of the noise figure of the LNA used as a cold-FET for the calibration purpose.

Figure 4.17 shows the noise figure of the LNA used for the calibration, the cold-FET, at two different temperatures. Here we used the reported noise figure in the data-sheet of the LNA and we did not measure the noise figure of LNA. The interpolation is done using a spline fit which interpolation goes thru every measurement point.

Next, we applied the effect of the noise figure variation to the traditional FD-calibration. Here is a summary of traditional microwave radiometer calibration, applied to a WiBAR. As such, the frequency dependence of variables will be kept explicit. Figure 4.18 shows the typical block diagram of a radiometer measuring a

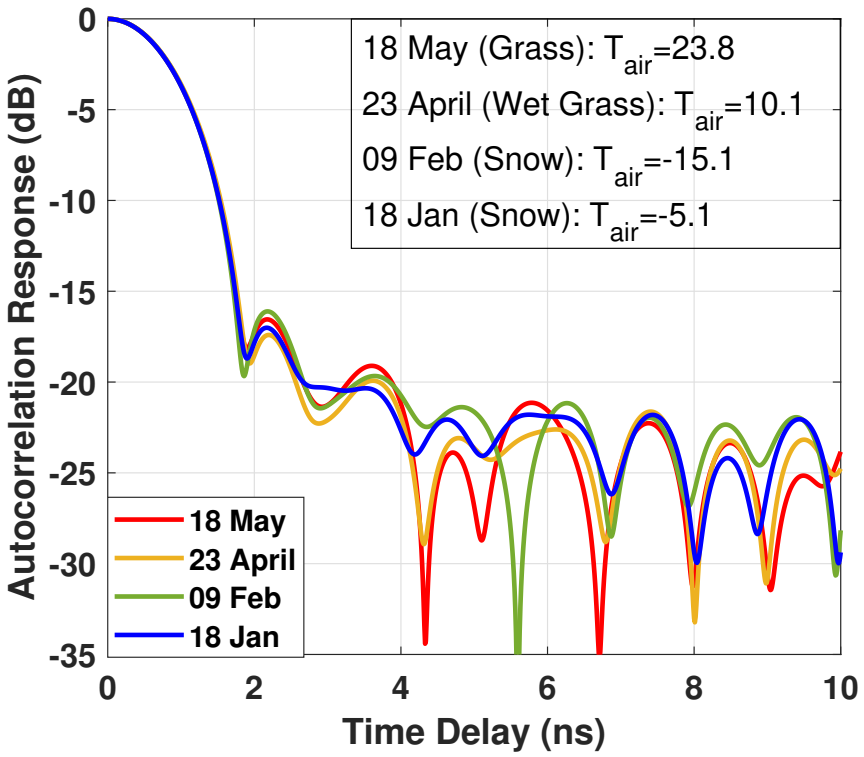

Figure 4.13: Autocorrelation response of measured spectrum on on different days of winter 2021 using FD-calibration. 1000 measured traces are averaged for the power spectrum. Hamming window is used in the post processing.

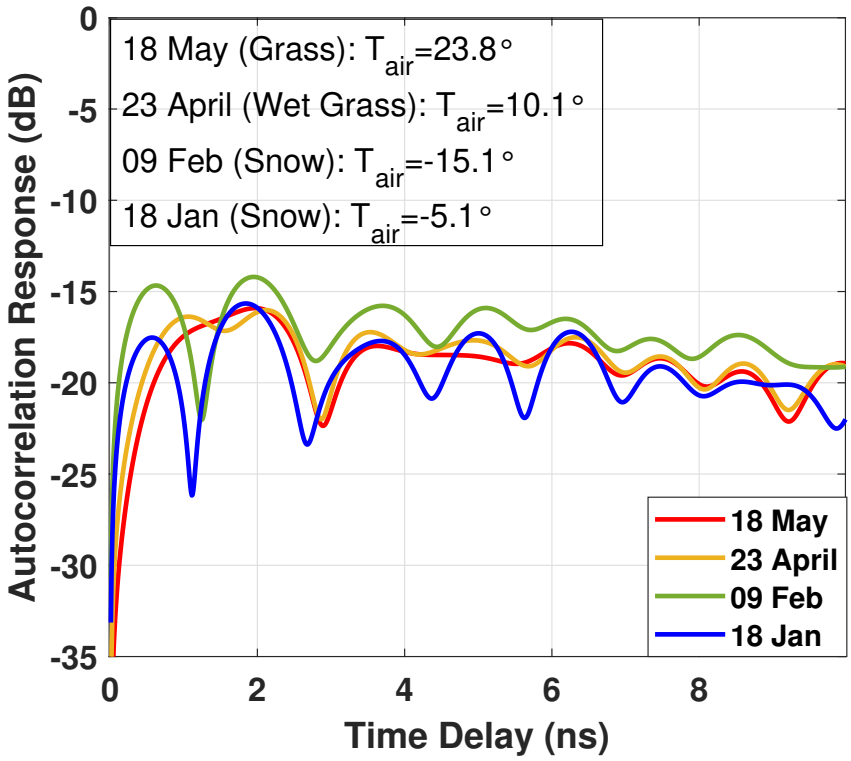

Figure 4.14: Autocorrelation response of measured spectrum on on different days of winter 2021 using TD-calibration. 1000 measured traces are averaged for the power spectrum. Hamming window is used in the post processing.

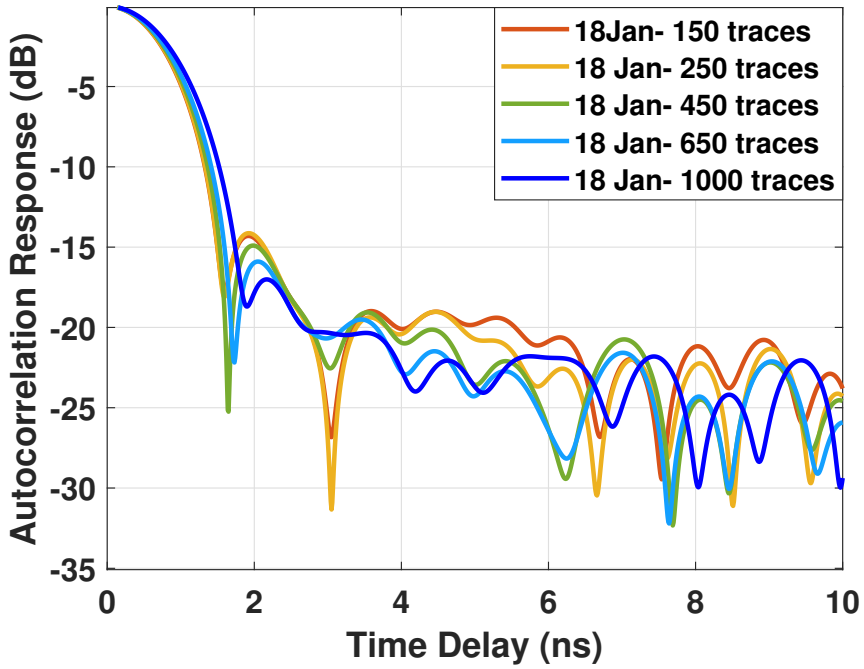

Figure 4.15: Autocorrelation response of measured spectrum on 18th January 2021 using FD-calibration for different numbers of sampling.

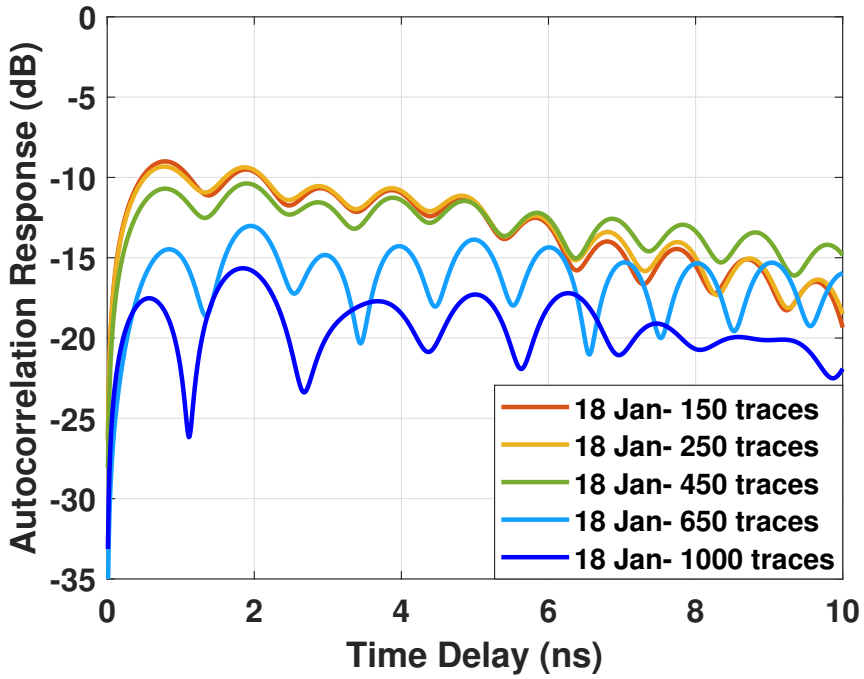

Figure 4.16: Autocorrelation response of measured spectrum on 18th January 2021 using TD-calibration for different numbers of sampling.

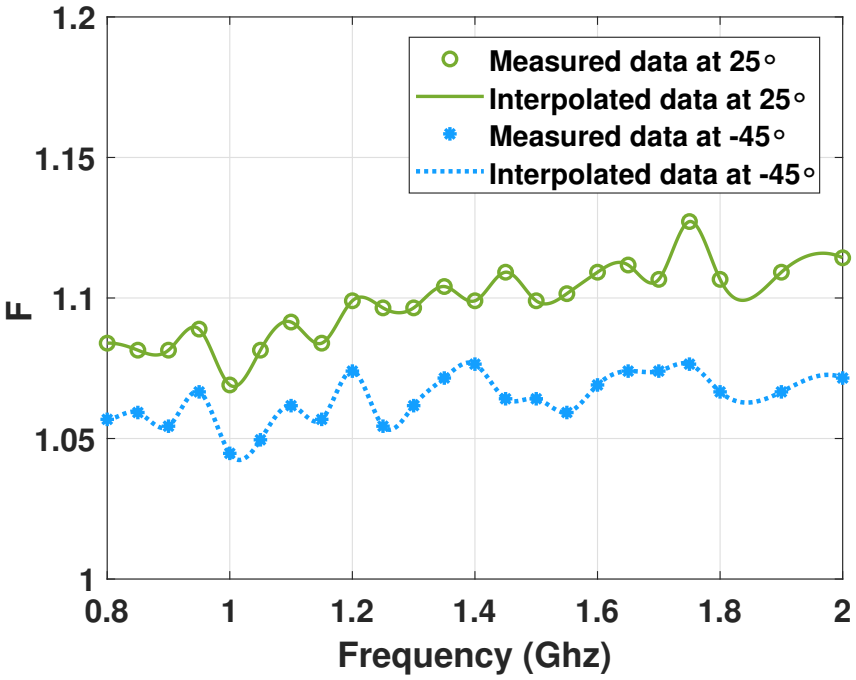

Figure 4.17: The noise figure of LNA at two different temperatures. To consider the effect of the noise figure, the measured data is interpolated over the frequency range of WiBAR.

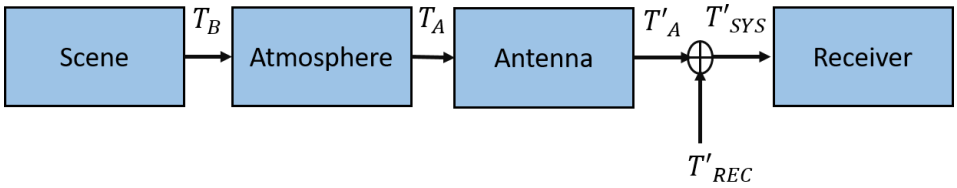

Figure 4.18: Conceptual block diagram of the radiometer measurement.

scene. V_{out} is the output of the radiometer and it is a function of frequency in a frequency-domain WiBAR.

At microwave frequencies, the Rayleigh-Jeans approximation to the Planck function applies, and the thermal noise power given off by the scene is given by $P(f) = k_B T_B(f) B$, where k_B is Boltzmann's constant, B is the bandwidth of observation, and $T_B(f)$ is the equivalent brightness temperature of the scene, which is the object of the radiometer measurement.

The atmosphere can alter the observed brightness temperature by the antenna. It can attenuate the brightness, it can emit its own brightness in the direction of (usually, upward to) the antenna, and it can also contribute brightness (usually, downward) onto the scene that is reflected. The block diagram is shown in 4.18. The atmosphere can also cause scattering or Faraday rotation, mixing brightnesses for V and H polarizations together.

For ground-based microwave remote sensing, we can neglect all of these effects and the brightness incident on the antenna aperture, $T_A(f)$, is the same as that coming from the scene, $T_B(f)$.

The last two blocks, the antenna and the receiver, constitute the radiometer. The instrument is broken into two blocks because internal calibration signals are injected at the junction of the two blocks: the switch where the antenna or calibration loads are selected is the point at which these two blocks are separated, conceptually. For the WiBAR, these internal calibration sources are the matched load and the

ColdFET *Frater and Williams* (1981). In this conceptual block diagram, the isolator and coaxial cable running from the antenna port to the calibration switch is considered part of the antenna, not part of the receiver.

In this derivations the unprimed variables are used for those associated with the input to the antenna and primed variables for the output of the antenna. Assuming the target (calibration source or scene) is beam-filling, the interpretation of the effect of the antenna is simplified. The integrals of the incident brightness over all directions reduces to the brightness temperature, $T_A(f)$. In this case, the effect of the antenna is just like that of an attenuator, Eq. 4.4:

$$T'_A(f) = T_A(f)/\eta(f) + T_{0ant}(1 - 1/\eta(f) \tag{4.4}$$

where T_{0ant} is the physical temperature of the antenna and η is the antenna's ohmic losses. Ideally, the losses should be 0 dB ($\eta = 1$, efficiency of 100%) in which case the physical temperature is immaterial and $T'_A(f) = T_A(f)$, but real antennas cannot achieve this.

The combined brightnesses of the receiver and the output of the antenna is known as the system temperature, Eq. 4.5. The receiver then amplifies the signal. The output indication, $P_{out}(f)$, is proportional to the output power by the receiver gain $G(f)$ as it is shown in Eq. 4.6.

$$T_{SYS}(f) = T'_A(f) + T_{REC}(f) \tag{4.5}$$

$$P_{out} = k_B B(T_A + T_{REC})G(f) \tag{4.6}$$

The internal calibration provides points at the input to the receiver (or output of the antenna), while the external calibration provides those points at the input to the antenna.

Eq. 4.7 shows the brightness temperature of load and coldFET and the assumptions that are considered.

$$\begin{cases} T_{A-load}(f) = T_0 \\ T_{A-cf}(f) = T_0(F-1) \\ T_0 = 273K \end{cases} \tag{4.7}$$

where T_0, is the physical temperature of the load. In this calibration we are considering the effect of the noise figure, F, of the LNA in the coldFET.

For the L-band FD-WiBAR, the $P_{out}(f)$ are the averaged spectral powers from the collected data files during the field measurements. Simplified power equations for the three sources (Load, Cold-FET, Scene) are:

$$P_l = k_B B(T_0 + T_{REC})G(f) \tag{4.8}$$

$$P_{cf} = k_B B(T_0(F-1) + T_{REC})G(f) \tag{4.9}$$

$$P_{sc} = k_B B(T_A + T_{REC})G(f) \tag{4.10}$$

By subtracting Eq. 4.8 and Eq. 4.9, $G(f)$ is calculated.

$$\frac{P_{cf} - P_l}{K_B B} = T_0 F G(f) - 2(T_0 G(f)) \tag{4.11}$$

$$G(f) = \frac{P_{cf} - P_l}{K_B B} \frac{1}{T_0.(F-2)} \tag{4.12}$$

from Eq. 4.8, T_{REC} is:

$$T_{REC} = T_0(\frac{P_l}{P_{cf} - P_l}(F-2) - 1) \tag{4.13}$$

By substituting the T_{REC} and $G(f)$ in Eq. 4.10 the temperature of the scene is

calculated in Eq. 4.14.

$$T_A = \frac{P_{sc} - P_l}{P_{cf} - P_l} T_0(F-2) + T_0 \tag{4.14}$$

By simplifying the Eq. 4.14 the new frequency domain calibration is:

$$\frac{T_A}{T_0} = \frac{(P_{sc} - P_{cf})(2-F)}{P_l - P_{cf}} + (F-1) \tag{4.15}$$

Figure 4.19 shows the results of applying new FD-calibration and traditional FD-calibration to the measured spectrum of 21st of February 2021. The new calibration is applied to an average of 500 samples and 1000 samples, however, it increases the noise figure and it did not improve the results.

4.5 Conclusions

In this Chapter, we made measurements to recover the microwave travel time for different thicknesses and measure the brightness temperature of the snow layer. UWBRAD and WiBAR were deployed in the Keweenaw Research Center (KRC) from February 2020 to May 2021 to demonstrate these techniques.

There are many uncertainties in measurements of winter 2021 which is affecting the calculation of snow depth and due to COVID lockdown, we were not able to fix them. Some of these uncertainties are listed below:

- The surface was rough and the lawn was not mowed.
- The incident angle changed to 20° from 70°, which increases the effect of a rough surface.
- We lost the thermal control on WiBAR in March 2020.
- We lost the communication with the UWBRad, and there is no RFI info for 2021 datasets.

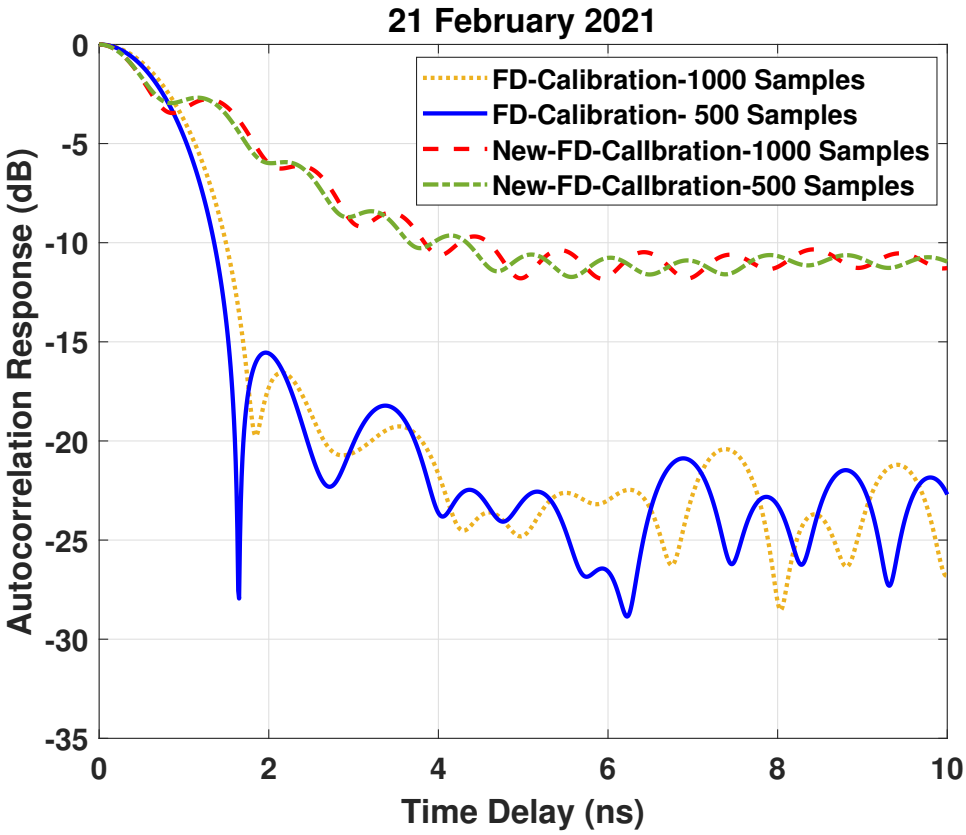

Figure 4.19: Autocorrelation response of measured spectrum on 21th February 2021 using original FD-calibration and new FD-calibration for different numbers of sampling.

- The interpolation method of the manufacturer's noise figure data, and whether it is truly appropriate for the emission from the LNA's input.

Results on snowpack thickness measurements need further analysis, but appear promising for demonstrating the presence of a secondary peak in the autocorrelation function at a time delay corresponding to the snowpack thickness.

CHAPTER V

Above Snow Vegetation Effects on Wideband Autocorrelation Radiometry

5.1 Introduction

Instruments like WiBAR measure the microwave emission from a scene of snow and ice over a wide and low frequency band where volume scattering within the snow/ice layer is negligible. Such instruments are exemplified by the 0.5-2.0GHz Ultra Wideband Software Defined Radiometer (UWBRAD) (*Andrews et al.*, 2018) and the Wiedband Autocorrelation Radiometer (WiBAR) (*Mousavi et al.*, 2018).

Experiments and modeling work have demonstrated that such wideband brightness temperature spectra can show oscillatory features. These features arise from coherent interference among the direct upward emission and its replicas from multiple reflections, Fig. 5.2, and are related to the layer thickness of snow or lake ice with a small absorptive loss.

Oscillatory patterns of the brightness temperature (TB) versus frequency have a period that is inversely proportional to the layer thickness, and therefore are also revealed in the Fourier transforms of the brightness spectra, known as the autocorrelation function of the microwave emission, where recurring peaks in time are separated by intervals that represent the round trip travel time of the electromagnetic

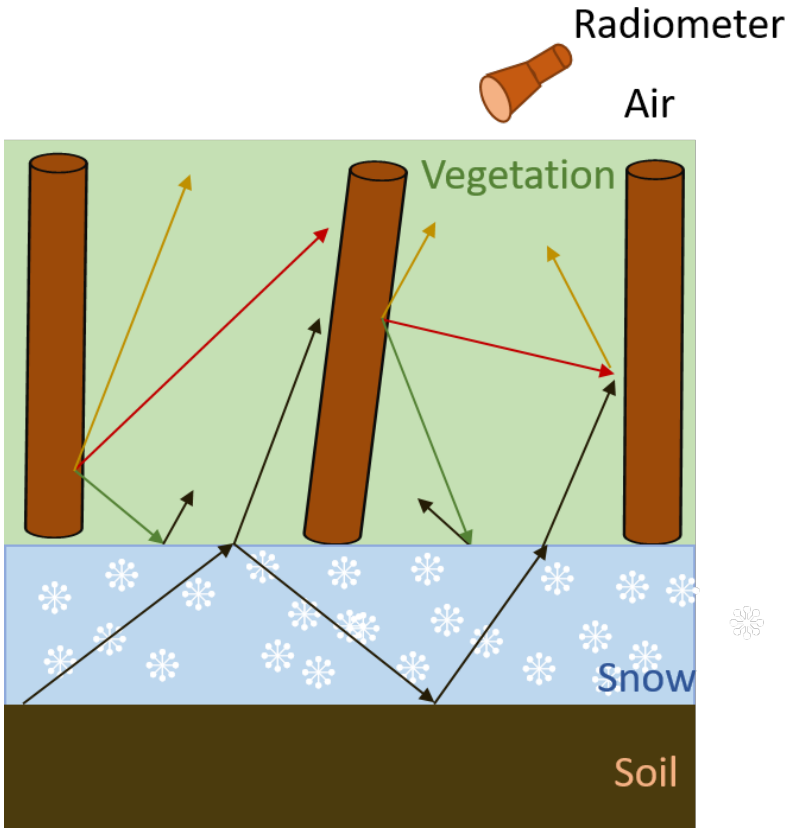

Figure 5.1: Illustration of a vegetation layer above a terrestrial snow layer on top of soil and the microwave emission mechanism.

emission in the layer. The TB angular pattern at a fixed frequency also shows oscillatory features when coherent interference effects are present.

The amplitude of these oscillatory patterns can be reduced in the presence of inhomogeneous scenes (*Tan et al.*, 2015), interface roughness (*Sanamzadeh et al.*, 2017), and any above snow vegetation canopy. Scene inhomogeneity, as exemplified by variations in layer thickness within the radiometer footprint, averages and smooths out coherent interference patterns. Interface roughness, common in all natural interfaces, can cause polarization and angular coupling of microwave emissions, and succeedingly weakening or destroying wave coherence if the scale of surface roughness is comparable to the observing wavelength. The above snow vegetation canopy, as represented by cylinders in Fig. 5.2, is also an important factor affecting the application of wideband

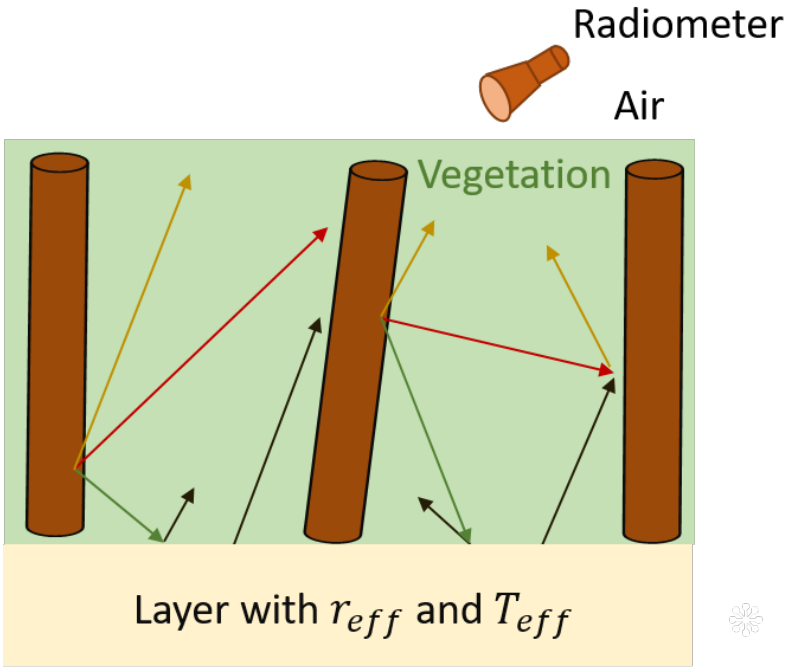

Figure 5.2: Illustration of the the microwave emission mechanism for a vegetation layer above a general layer with effective reflectivity of r_{eff} and effective temperature of T_{eff}.

autocorrelation radiometry in terrestrial snow remote sensing.

In this chapter, the effects of an above snow vegetation layer on scene brightness temperature spectra is analyzed. Particularly the possible decay of wave coherence arising from the volume scattering in the vegetation canopy. In our analysis, the snow layer is assumed to be flat, and its upward emission and surface reflectivities are modeled by a fully coherent model (*Tan et al.*, 2015), while volume scattering from the vegetation layer is described by an incoherent radiative transfer model (**?**). The solution to the radiative transfer equation is obtained through an interative approach that accounts for multiple scattering effects. Multiple scattering effects become important when the vegetation layer becomes thick and dense, and thus is associated with a moderate to large optical thickness and a potentially large scattering albedo.

5.2 Formulations

A vegetation layer of height H above a layer of snow is considered as illustrated in Fig. 5.2. The reference coordinate $z = 0$ is defined at the snow/vegetation interface. The generation and propagation of polarimetric microwave emissions through the vegetation layer is governed by the vector radiative transfer equation 5.1.

$$\begin{cases} \cos\theta \frac{d\overline{T}_u(\theta,z)}{dz} = -\overline{\overline{\kappa}}_e(\theta) \cdot \overline{T}_u(\theta,z) + \overline{\kappa}_a(\theta) T + \overline{S}(\theta,z) \\ -\cos\theta \frac{d\overline{T}_d(\theta,z)}{dz} = -\overline{\overline{\kappa}}_e(\pi-\theta) \cdot \overline{T}_d(\theta,z) + \overline{\kappa}_a(\pi-\theta) T + \overline{W}(\theta,z) \end{cases} \tag{5.1}$$

where $\overline{T}_u$ and $\overline{T}_d$ represents the upward and downward brightness temperatures. $\overline{\overline{\kappa}}_e(\theta)$ and $\overline{\kappa}_a(\theta)$ are the extinction matrix and emission vectors, respectively, for a wave propagating along angle θ. $\overline{S}(\theta,z)$ and $\overline{W}(\theta,z)$ are related to the phase matrix $\overline{\overline{p}}(\theta,\theta')$ through, respectively,

$$\begin{cases} \overline{S}(\theta,z) = \int_0^{\pi/2} d\theta' \overline{\overline{p}}(\theta,\theta') \cdot \overline{T}_u(\theta',z) + \int_0^{\pi/2} d\theta' \overline{\overline{p}}(\theta,\pi-\theta') \cdot \overline{T}_d(\theta',z) \\ \overline{W}(\theta,z) = \int_0^{\pi/2} d\theta' \overline{\overline{p}}(\pi-\theta,\theta') \cdot \overline{T}_u(\theta',z) + \int_0^{\pi/2} d\theta' \overline{\overline{p}}(\pi-\theta,\pi-\theta') \cdot \overline{T}_d(\theta',z) \end{cases} \tag{5.2}$$

and the boundary conditions at $z = 0$ and H are, respectively,

$$\begin{cases} \overline{T}_u(\theta,0) = \overline{\overline{r}}_{eff}(\theta) \cdot \overline{T}_d(\theta,0) + C\left(\overline{\overline{I}} - \overline{\overline{r}}_{eff}(\theta)\right) \overline{T}_{eff}(\theta) \\ \overline{T}_d(\theta,H) = 0 \end{cases} \tag{5.3}$$

where C is equal to $(KB/2)$ with KB and λ representing the Boltzmann's constant and the wavelength, respectively. The scene $\overline{T}_b$ is then $\overline{T}_b(\theta) = \overline{T}_u(\theta,H)$.

In the boundary conditions, $\overline{\overline{r}}_{eff}(\theta)$ and $\overline{\overline{T}}_{eff}(\theta)$ are the effective reflectivities and temperatures of the snow layer above the soil, which for flat interfaces is determined exactly in terms of the layered medium reflection coefficients, which includes coherent interactions (*Tan et al.*, 2015). The effective temperature $\overline{\overline{T}}_{eff}(\theta)$ is related to the scene brightness temperature $\overline{T}_{b0}$ with no vegetation coverage by

$$\overline{T}_{b0} = (\overline{\overline{I}} - \overline{\overline{r}}_{eff}(\theta))\overline{T}_{eff}(\theta) \tag{5.4}$$

The vector radiative transfer equations can be cast into integral equations by considering S and W as source terms. In the most simple case when we consider 2×1 Stokes parameters.

$$T_u(\theta, z) = \begin{bmatrix} T_{uv}(\theta, z) \\ T_{uh}(\theta, z) \end{bmatrix} T_d(\theta, z) = \begin{bmatrix} T_{dv}(\theta, z) \\ T_{dh}(\theta, z) \end{bmatrix} \tag{5.5}$$

$$\overline{\overline{\kappa}}_e(\theta) = \begin{bmatrix} \kappa_{ev}(\theta) & 0 \\ 0 & \kappa_{eh}(\theta) \end{bmatrix} \overline{\kappa}_a(\theta) = \begin{bmatrix} \kappa_{av}(\theta) \\ \kappa_{ah}(\theta) \end{bmatrix} \tag{5.6}$$

$$\overline{\overline{p}}(\theta, \theta') = \begin{bmatrix} p_{vv}(\theta, \theta') & p_{vh}(\theta, \theta') \\ p_{hv}(\theta, \theta') & p_{hh}(\theta, \theta') \end{bmatrix} \tag{5.7}$$

$$\overline{\overline{r}}_{eff}(\theta) = \begin{bmatrix} r_{eff,v} & 0 \\ 0 & r_{eff,h} \end{bmatrix} \tag{5.8}$$

We can now solve the integral equation iteratively by considering the phase matrix $\overline{\overline{p}}$ as small quantity and by balancing orders. Thus, the zero-th order solution is obtained.

$$
\begin{aligned}
T_u^{(0)}(\theta, z) = & \\
& \sec\theta \int_0^z dz' \exp\left(\kappa_e(\theta)\sec\theta\,(z'-z)\right)\kappa_a(\theta)\,T \\
& + \exp\left(-\kappa_e(\theta)\sec\theta z\right) r_{eff}(\theta)\sec\theta \\
& \int_0^H dz' \exp\left(-\kappa_e(\pi-\theta)\sec\theta z'\right)\kappa_a(\pi-\theta)\,T \\
& + \exp\left(-\kappa_e(\theta)\sec\theta z\right)\left(1-r_{eff}(\theta)\right)T_{eff}(\theta)
\end{aligned}
\tag{5.9}
$$

$$
\begin{aligned}
T_d^{(0)}(\theta, z) = & \\
& \sec\theta \int_z^H dz' \exp\left(-\kappa_e(\pi-\theta)\sec\theta\,(z'-z)\right)\times\kappa_a(\pi-\theta)\,T
\end{aligned}
\tag{5.10}
$$

These are the solution when the scattering effects are ignored. Each term has very clear meaning known as the τ-ω solution.

The $(n+1)$ th order are related to the n-th order, $n \geq 0$, by

$$
\begin{aligned}
T_u^{(n+1)}(\theta, z) = & \\
& \sec\theta \int_0^z dz' \exp\left(\kappa_e(\theta)\sec\theta\,(z'-z)\right) S^{(n+1)}(\theta, z') \\
& + \exp\left(-\kappa_e(\theta)\sec\theta z\right) r_{eff}(\theta)\sec\theta \\
& \times \int_0^H dz' \exp\left(-\kappa_e(\pi-\theta)\sec\theta z'\right) W^{(n+1)}(\theta, z')
\end{aligned}
\tag{5.11}
$$

$$T_d^{(n+1)}(\theta, z) = \sec\theta \int_z^H dz' \exp\left(-\kappa_e (\pi - \theta) \sec\theta (z' - z)\right) \times W^{(n+1)}(\theta, z') \tag{5.12}$$

Note that the iterative solution is identical to that of the scalar differential equations except that we update the source term $\overline{S}$ and $\overline{W}$ polarimetrically,

$$\begin{aligned}
\overline{S}^{(n+1)}(\theta, z) &= \int_0^{\pi/2} d\theta' \overline{\overline{p}}(\theta, \theta') \cdot \overline{T}_u^{(n)}(\theta', z) + \int_0^{\pi/2} d\theta' \overline{\overline{p}}(\theta, \pi - \theta') \cdot \overline{T}_d^{(n)}(\theta', z) \\
\overline{W}^{(n+1)}(\theta, z) &= \int_0^{\pi/2} d\theta' \overline{\overline{p}}(\pi - \theta, \theta') \cdot \overline{T}_u^{(n)}(\theta', z) + \int_0^{\pi/2} d\theta' \overline{\overline{p}}(\pi - \theta, \pi - \theta') \cdot \overline{T}_d^{(n)}(\theta', z)
\end{aligned} \tag{5.13}$$

Finally, the brightness temperature is obtained from

$$\overline{T}_b(\theta) = \overline{T}_u(\theta, H) = \sum_{n=0}^{\infty} \overline{T}_u^{(n)}(\theta, H) \tag{5.14}$$

5.3 Result and Discussions

As a starting point, a layer of vertical circular cylinders is considered to represent the above snow vegetation canopy. The cylinders are of radius $a = 7$ cm, length $L = 16.8$ m, and a vegetation volumetric moisture content $m_{veg} = 0.5$. The Ulaby and El-Rayes model (*Ulaby and El-Rayes*, 1987) is applied to compute the dielectric constant of the cylinders, leading to $\epsilon_{rp} = 32.1 + i10$ at 1.41 GHz.

The infinite cylinder approximation (ICA) (*Tsang and Kong*, 2004) and the independent scattering assumption are employed to compute the scattering phase matrix, extinction coefficients, and absorption coefficients of the vegetation layer.

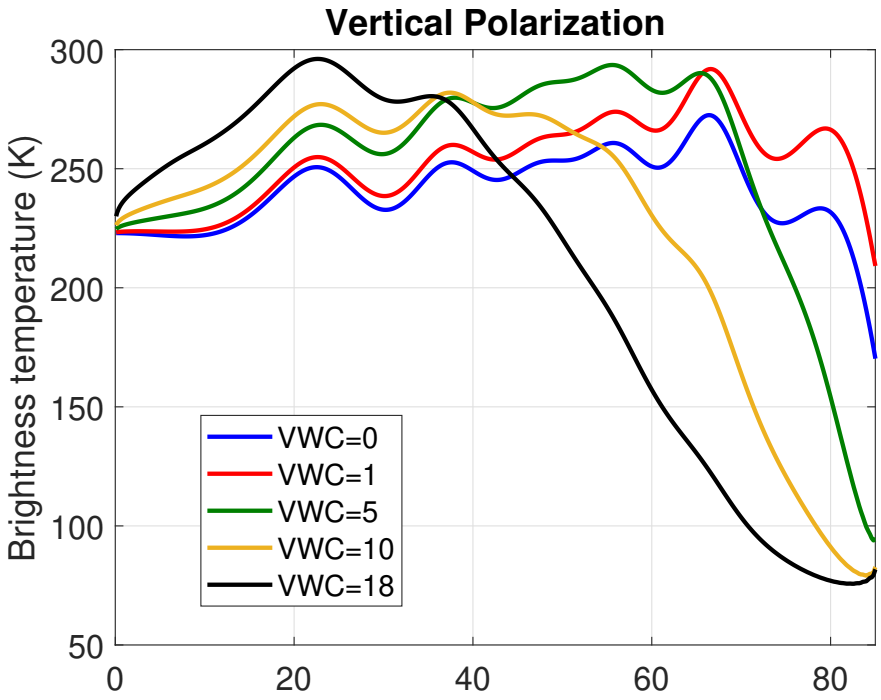

Figure 5.3: Vertical polarized brightness temperatures versus observation angles for various vegetation densities, in kg/m^2 . The results are computed at L-band.

In Figs. 5.3 and 5.4, the brightness temperatures at L band (1.41 GHz) as a function of observation angles are shown, for vertical and horizontal polarizations, respectively. The snow layer has a thickness $d = 1$ m and a volume fraction $f_v = 0.25$ following Matzler's empirical model (*Matzler*, 1996). In each graph, brightness temperature results are compared for cases with increasing vegetation densities having vegetation water contents (VWC) of 0, 1, 5, 10, and 18 kg/m^2.

The brightness temperature results are computed up to 5th order and show clear convergence. Multiple scattering results show significant differences from the zero-th order solution, i.e, the $\tau - \omega$ model, as exemplified in their angular dependence and VWC dependence (zero-th order solution not shown). It is shown that when VWC is 0 kg/m^2, i.e., no vegetation, the brightness temperature angular pattern shows coherent oscillations that contain information about the snow water equivalent.

These oscillation patterns weaken but remain with low to moderate vegetation coverage. However, when the VWC is large, indicating thick vegetation, the oscillatory

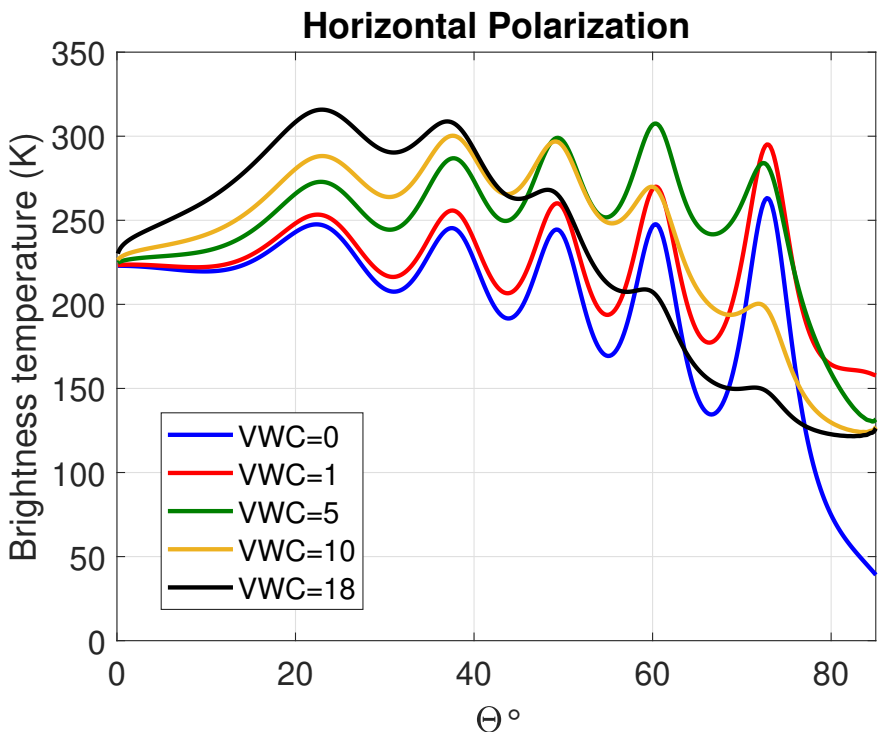

Figure 5.4: Horizontal polarized brightness temperatures versus observation angles for various vegetation densities, in kg/m^2 . The results are computed at L-band.

patterns in Tb become less distinguishable due to scattering induced angular and polarization coupling. Vertical polarized emission experiences increased loss of coherence as compared to horizontal polarized emission as the vertical cylinders.

5.4 Conclusion

A microwave emission model that incorporates coherent wave interactions in the snow layer and incoherent multiple scattering effects in the above-snow vegetation canopy layer was developed to examine the effects of the vegetation scattering and emission effects on wideband autocorrelation radiometry for sensing terrestrial snow water equivalent. Computed brightness temperature angular patterns at L-band indicate that loss of coherent wave features can occur for moderate to high vegetation coverage. This loss of coherence appears related to angular and polarization coupling caused by multiple scattering in the vegetation layer. Emission from the vegetation layer itself also contaminates coherent wave interference features.

More examinations can be done to study the brightness temperature dependence on snow depth and frequency dependence with varying VWCs and to incorporate more representative vegetation structures. Also the differences in the scene brightness temperatures between coherent and incoherent models for snowpack emissions can be compared, because two might be different even if vegetation scattering completely washes out coherent oscillations.

CHAPTER VI

Passive Multiple Scattering of Forests Using Radiative Transfer Theory With an Iterative Approach

6.1 Introduction

Passive and active microwave remote sensing of vegetated land surface is important as indicated by the rapid growth of the number of microwave radiometers and radars in the L- to X- band frequency range for land surface observation. These include the Advanced Microwave Scanning Radiometer-2 (AMSR2) (*Kachi et al.*, 2013), the Soil Moisture and Ocean Salinity (SMOS) radiometer (*Kerr et al.*, 2012), the NASA-ISRO Synthetic Aperture Radar (NISAR) (*NISAR*, 2019), and the Soil Moisture Active and Passive (SMAP) mission (*Entekhabi et al.*, 2010).

The sensitivity of radiometer brightness temperature and radar backscatter signatures to land surface features is affected strongly by the sensing wavelength, as well as the landscape structure and moisture conditions. Soils are typically covered by heterogeneous vegetation of various types such as grass, crops, woodlands, and forests. L-band frequency is suitable for remote sensing of soil moisture of vegetated surface with various amounts of vegetation water contents (VWCs) (*Jackson and Schmugge*, 1991; *Monerris et al.*, 2009; *Grant et al.*, 2009; *Kurum et al.*, 2012; *Schwank et al.*,

2008). A unified physical model of vegetated surface for active and passive microwave remote sensing is required to interpret and synergistically utilize data from these missions including backscattering coefficients and brightness temperatures (*Bolten et al.*, 2003; *Tan et al.*, 2015).

In passive microwave remote sensing of vegetated land surface, the tau-omega model has been primarily adopted over the years. Tau-omega model can be derived from the zero-th order solution of radiative transfer equation which does not consider the effect of the scattering phase matrix (*Bindlish et al.*, 2009). In this model, scattering albedo is estimated empirically for specific vegetation types, which is generally much smaller than the physical single scattering albedo, i.e., the ratio of the scattering coefficient over the extinction coefficient of the random media distributed in a random volume (*Wigneron et al.*, 2017). This approach is only valid for small scattering albedo and optical thickness. In (*Karam*, 1997; *Kurum et al.*, 2012) the zeroth and first order radiative transfer equations is developed for vegetation canopy scattering.

For moderate scattering albedo when optical thickness of the layer of vegetation over soil is larger than 0.4, effects of multiple scattering need to be carefully considered (*Liao et al.*, 2016). In this chapter, iterative approach is used to solve the passive radiative transfer equation and iteration is carried out to higher orders numerically to compute the brightness temperatures. Effects of multiple scattering for vegetation layer with large scattering albedo and optical thickness are illustrated.

We presented a unified framework for both active and passive remote sensing of vegetated land surfaces using radiative transfer theory that takes into account multiple scattering effects and backscattering

enhancement effects. Earlier in (*Dente et al.*, 2014; *Guerriero et al.*, 2016) combined active and passive model are presented without including backscattering enhancement. Considering backscattering enhancement allows the use of the same set of physical

parameters to model active and passive microwave signatures simultaneously. Previous models of active and passive RT theory are inconsistent, requiring different sets of parameters for the same vegetated surface (*Akbar and Moghaddam*, 2015).

Multiple scattering effects are important in C- and X- bands for moderate vegetation coverage, and in L- band for high VWC cases like tree trunks in forest areas. Here, the iterative approach is used to solve both the active and passive RT equations with a single-reflective boundary at the bottom of the vegetation layer and negligible reflections from the top (vegetation/air) boundary. The approach we adopted is closely related to (*Tan et al.*, 2015) where a snow layer with reflective boundaries at both top and bottom are considered. In (*Tan et al.*, 2015), the iterative approach with cyclical corrections is only applied to active radiative transfer equation; since the snow layer comprised of snow grains has a regular and smooth phase matrix, the discrete coordinate approach (*Tsang et al.*, 1985) can be readily applied for passive radiative transfer equations to take into account the multiple scattering effects. However, in this work, the vegetation layer, including large scatterers of tree trunks and branches, is characterized by highly singular phase matrices; the discrete coordinate approach fails so that we seek the iterative approach to solve both active and passive radiative transfer equations.

Recently, the Numerical Maxwell Model of 3D (NMM3D) simulations of vegetation scattering is proposed and being implemented (*Huang et al.*, 2017), providing benchmark solutions for vegetation scattering. The approach yields much higher vegetation transmissivity than the tau-omega model predictions. In (*Huang et al.*, 2017), the vegetation structure is decomposed into simple parts, such as small branches, and for each part the scattering T-matrix is calculated; wave interactions among multiple objects are then solved through the Foldy-Lax multiple scattering equations using the T-matrices. With Monte-Carlo statistical averages and the overhead to construct the T-matrices, this hybrid method costs considerable CPU time and memory.

In this chapter the radiative transfer equations are solved by a numerical iterative approach for passive configuration which includes multiple scattering of the vegetation. The numerical iterative approach predicts significantly different results compared to the tau-omega model *Salim et al.* (2021).

The results of brightness temperatures using iterative approach compared with tau-omega model to show the effect of multiple scattering in soil moisture retrieval. Then a realistic forest scenario inspired by the SMAPVEX12 campaign measurements is set up and the results of simulated brightness temperatures at L-band are compared with measurements from the airborne Passive and Active L-band Sensor (PALS) acquired in the SMAPVEX12 campaign *Salim et al.* (2020).

6.2 RT Theory

The RT theory with a single reflective boundary at the bottom is typically used for vegetation scattering layer. The reflection off the top boundary (vegetation/air) is negligible and is considered to be zero. The vector radiative transfer equation is expressed in Eq. (6.1), (*Tsang et al.*, 2004).

$$\begin{cases} \cos\theta \frac{d\overline{I}_u(\theta,\phi,z)}{dz} = -\overline{\overline{\kappa}}_e(\theta) \cdot \overline{I}_u(\theta,\phi,z) + C\overline{\kappa}_a(\theta) T + \overline{S}(\theta,\phi,z) \\ \\ -\cos\theta \frac{d\overline{I}_d(\theta,\phi,z)}{dz} = -\overline{\overline{\kappa}}_e(\pi-\theta) \cdot \overline{I}_d(\theta,\phi,z) + C\overline{\kappa}_a(\pi-\theta) T + \overline{W}(\theta,\phi,z) \end{cases} \tag{6.1}$$

where C is equal to $\dfrac{k_B}{\lambda^2}$ with k_B and λ representing the Boltzmann constant and the wavelength, respectively, and T represents the temperature of vegetation layer. $\overline{I}_u(\theta,\phi,z)$ and $\overline{I}_d(\theta,\phi,z)$ represent the upward and downward intensities, respectively. Source terms $\overline{S}(\theta,\phi,z)$ and $\overline{W}(\theta,\phi,z)$ represent coupled scattering from other directions of intensity propagation to $\overline{I}_u(\theta,\phi,z)$ and $\overline{I}_d(\theta,\phi,z)$, respectively. These two source

terms and the specific intensities $\overline{I}_u$ and $\overline{I}_d$ are functions of three independent variables, the vertical coordinate z, the inclination angle θ, between 0 and $\pi/2$, and the azimuth angle ϕ, between 0 and 2π.

$$\begin{cases} \overline{S}(\theta,\phi,z) = \\ \quad \int_0^{2\pi} d\phi' \int_0^{\frac{\pi}{2}} d\theta' \sin\theta' [\overline{\overline{P}}(\theta,\phi;\theta',\phi')\overline{I}_u(\theta',\phi',z) + \overline{\overline{P}}(\theta,\phi;\pi-\theta',\phi')\overline{I}_d(\theta',\phi',z)] \\ \\ \overline{W}(\theta,\phi,z) = \\ \quad \int_0^{2\pi} d\phi' \int_0^{\frac{\pi}{2}} d\theta' \sin\theta' [\overline{\overline{P}}(\pi-\theta,\phi;\theta',\phi')\overline{I}_u(\theta',\phi',z) + \overline{\overline{P}}(\pi-\theta,\phi;\pi-\theta',\phi')\overline{I}_d(\theta',\phi',z)] \end{cases} \tag{6.2}$$

In the RT equations, the source terms $\overline{S}$ and $\overline{W}$ are related to $\overline{I}$ by the scattering phase matrix $\overline{\overline{P}}(\theta,\phi;\theta',\phi')$, as described in Eq. (6.2). The phase matrix is derived from the scattering amplitude of the elementary scatterers using physical models such as the finite-length cylinder scattering with infinite length approximation (ICA) for the scattering of tree trunk, primary branches, and secondary branches and the thin disk approximation (TDA) for the leaf scattering (*Tsang et al.*, 1985). $\kappa_e(\theta)$ is the extinction coefficient which is calculated using the optical theorem from the forward scattering amplitude, and $\kappa_s(\theta)$ is scattering coefficient derived from the scattering amplitude ($f_{\alpha\beta}$) and integrated over all scattering angles. The subscript 'α' and 'β' denote the scattering and incidence polarizations, respectively. $\kappa_a(\theta)$ is the absorption coefficient which is calculated by subtracting the scattering coefficient from the extinction coefficient.

The boundary conditions for active RT theory are expressed in Eq. (6.3).

$$\begin{cases} \overline{I}_d(\theta, \phi, z = d) = \overline{I}_0 \delta(\cos\theta - \cos\theta_0)\delta(\phi - \phi_0) \\ \overline{I}_u(\theta, \phi, z = 0) = \overline{\overline{r}}_{12}(\theta)\overline{I}_d(\theta, \phi, z = 0) \end{cases} \tag{6.3}$$

where the $\overline{I}_0$ term represents the incident wave. The boundary conditions of the specific intensity in passive RT are shown in Eq. (6.4).

$$\begin{cases} \overline{I}_d(\theta, z = d) = 0 \\ \\ \overline{I}_u(\theta, z = 0) = \overline{\overline{r}}_{12}\overline{I}_d(\theta, z = 0) + C(\overline{\overline{I}} - \overline{\overline{r}}_{12})\overline{T}_2 \end{cases} \tag{6.4}$$

In Eq. (6.3) and Eq. (6.4) $\overline{\overline{r}}_{12}$ is the Fresnel reflectivity matrix for the Stokes parameters at the vegetation/soil boundary, and T_2 is the physical temperature of soil. T_2 is stacked into a vector in Eq. (6.4) to facilitate the mathematical formulation. Kirchhoff approximation (*Tsang and Kong*, 2004) is used to account for the effects of interface roughness where the Fresnel reflectivity of power for horizontal and vertical polarizations, r_h and r_v, respectively, are multiplied by an attenuation factor $\exp(-4(k_0 s\cos\theta)^2)$, where s is the rms height of the vegetation/soil interface, and k_0 is the wavenumber in the vegetation layer, which is approximated to be the free-space wavenumber, while the bistatic scattering from the rough interface is ignored.

$$\begin{cases} r_h = \left| \dfrac{\cos\theta_1 - \sqrt{\frac{\epsilon_2}{\epsilon_1} - \sin^2\theta_1}}{\cos\theta_1 + \sqrt{\frac{\epsilon_2}{\epsilon_1} - \sin^2\theta_1}} \right|^2 \exp(-4(k_0 s\cos\theta)^2) \\ \\ r_v = \left| \dfrac{\frac{\epsilon_2}{\epsilon_1}\cos\theta_1 - \sqrt{\frac{\epsilon_2}{\epsilon_1} - \sin^2\theta_1}}{\frac{\epsilon_2}{\epsilon_1}\cos\theta_1 + \sqrt{\frac{\epsilon_2}{\epsilon_1} - \sin^2\theta_1}} \right|^2 \exp(-4(k_0 s\cos\theta)^2) \end{cases} \tag{6.5}$$

where ϵ_1 represents permittivity of the layer of vegetation and ϵ_2 denotes soil permittivity. The above passive and active radiative transfer equations are of the same form and the

extinction, scattering, and attenuation computations are based on the same physical model. This consistent formulation using the same physical scattering parameters provides a unified framework for active and passive remote sensing modeling.

6.3 Multiple scattering in Passive Remote Sensing Using Iterative Solution of RTE

Multiple scattering in passive remote sensing is illustrated in Fig. 6.1. In this section, we present the formulation of passive RTE to include the effect of multiple scattering in the modeling of brightness temperatures. Passive RTE with a single reflective boundary at the bottom is assumed (*Njoku and Entekhabi*, 1996). With statistical azimuthal symmetry, the passive RTEs are rewritten as follows with no explicit azimuthal angle ϕ dependence.

$$\begin{cases} \cos\theta \frac{d\overline{I}_u(\theta,z)}{dz} = -\overline{\overline{\kappa}}_e(\theta) \cdot \overline{I}_u(\theta,z) + C\overline{\kappa}_a(\theta) T + \overline{S}(\theta,z) \\ \\ -\cos\theta \frac{d\overline{I}_d(\theta,z)}{dz} = -\overline{\overline{\kappa}}_e(\pi-\theta) \cdot \overline{I}_d(\theta,z) + C\overline{\kappa}_a(\pi-\theta) T + \overline{W}(\theta,z) \end{cases} \tag{6.6}$$

where

$$\begin{cases} \overline{S}(\theta,z) = \int_0^{\frac{\pi}{2}} d\theta' \sin\theta' [\overline{\overline{p}}(\theta;\theta')\overline{I}_u(\theta',z) + \overline{\overline{p}}(\theta;\pi-\theta')\overline{I}_d(\theta',z)] \\ \\ \overline{W}(\theta,z) = \int_0^{\frac{\pi}{2}} d\theta' \sin\theta' [\overline{\overline{p}}(\pi-\theta;\theta')\overline{I}_u(\theta',z) + \overline{\overline{p}}(\pi-\theta;\pi-\theta')\overline{I}_d(\theta',z)] \end{cases} \tag{6.7}$$

In the passive RTEs, the phase matrix $\overline{\overline{p}}$ has no ϕ dependence due to statistical azimuthal symmetry, and it is related to $\overline{\overline{P}}$ through (6.8).

$$\overline{\overline{p}}(\theta,\theta') = \int_0^{2\pi} d\phi \overline{\overline{P}}(\theta,\phi;\theta',\phi') \tag{6.8}$$

To derive the iterative solution, the passive RTE in differential form, as illustrated in Eq. (6.6), is first cast into a set of coupled integral equations, as shown in Eq. (6.9), in scalar form.

$$\begin{cases} I_u(\theta,z) = \\ \quad C\sec\theta \int_0^z dz' \exp(\kappa_e(\theta)\sec\theta(z'-z))[\kappa_a(\theta)T + S(\theta,z')] + \\ \quad C\exp(-\kappa_e(\theta)\sec\theta z) r_{12}\sec\theta \int_0^d dz' \exp(-\kappa_e(\pi-\theta)\sec\theta z')[\kappa_a(\pi-\theta)T + W(\theta,z')] + \\ \quad C\exp(-\kappa_e(\theta)\sec\theta z)(1-r_{12})T_2 \\ \\ I_d(\theta,z) = \\ \quad C\sec\theta \int_z^d dz' \exp(-\kappa_e(\pi-\theta)\sec\theta(z'-z))[\kappa_a(\pi-\theta)T + W(\theta,z')] \end{cases} \tag{6.9}$$

The integral equations are then solved iteratively by considering the phase matrix as a small argument and balancing orders (*Tan et al.*, 2015; *Salim et al.*, 2019a,b). Therefore, the zero-th order solution is achieved by setting $\overline{S}$ and $\overline{W}$ to be zero, while the first order solution is obtained by substituting zero-th order solution into $\overline{S}$ and $\overline{W}$ and evaluating the integrals. Following the same procedure higher order solution of intensity is obtained.

The zero-th order intensities are explicitly given in Eq. (6.10). This leads to the tau-omega model where scattering from the vegetation only contributes to extinction of coherent wave propagation.

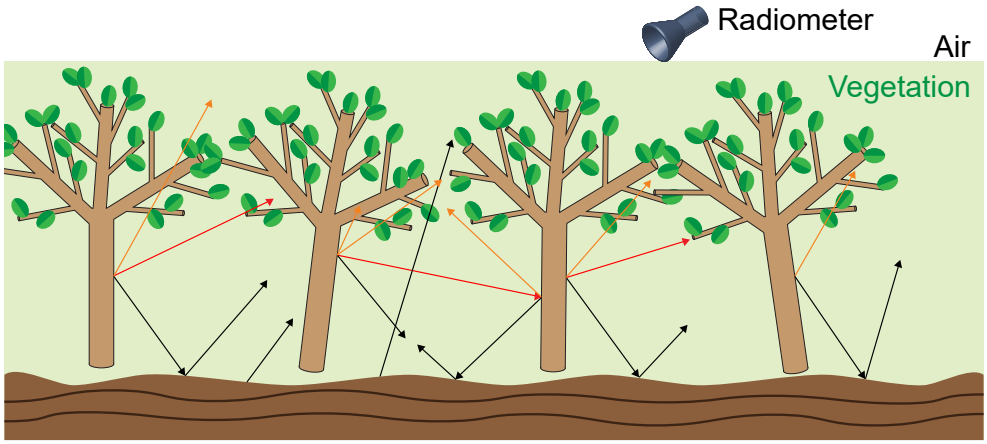

Figure 6.1: Illustration of a vegetation layer above soil and the microwave emission mechanism for passive configuration.

$$
\begin{cases}
I_u^{(0)}(\theta, z) = \\
\quad C \sec\theta \int_0^z dz' \exp\left(\kappa_e(\theta) \sec\theta \left(z' - z\right)\right) \kappa_a(\theta) T + \\
\quad C \exp\left(-\kappa_e(\theta) \sec\theta z\right) r_{12}(\theta) \sec\theta \int_0^d dz' \exp\left(-\kappa_e(\pi - \theta) \sec\theta z'\right) \kappa_a(\pi - \theta) T + \\
\quad C \exp\left(-\kappa_e(\theta) \sec\theta z\right) \left(1 - r_{12}(\theta)\right) T_2 \\
\\
I_d^{(0)}(\theta, z) = \\
\quad C \sec\theta \int_z^d dz' \exp\left(-\kappa_e(\pi - \theta) \sec\theta \left(z' - z\right)\right) \kappa_a(\pi - \theta) T
\end{cases}
\tag{6.10}
$$

The zero-th order brightness temperature is shown in Eq. (6.12) related to the zero-th order upward intensity through Eq. (6.11) and by carrying out the z-integrals. It contains three terms that correspond to upward emission from the soil, upward emission from the vegetation layer, and downward emission from the vegetation layer

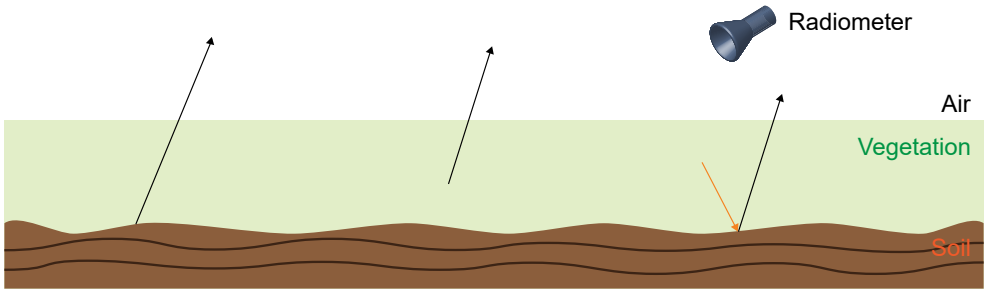

Figure 6.2: Zeroth order solution of brightness temperature which is a scattering free medium. It contains three terms: upward emission of ground, upward emission from the vegetation layer, and downward emission from the vegetation layer reflected by the ground.

reflected by the ground as shown in Fig. 6.2.

$$T_B{}^{(0)} = \frac{I_u^{(0)}(z=d,\theta)}{C} \tag{6.11}$$

$$\begin{cases} T_B{}^{(0)} = \\ \quad T_2(1-r_{12})e^{-\kappa_e d\sec(\theta)} + \frac{\kappa_a T}{\kappa_e}(1-e^{-\kappa_e d\sec(\theta)}) + \frac{\kappa_a T r_{12}}{\kappa_e}(1-e^{-\kappa_e d\sec(\theta)})e^{-\kappa_e d\sec(\theta)} \end{cases} \tag{6.12}$$

Higher order upward and downward intensities are computed as follows. The $(n+1)$-th order is related to the n-th order, $n \geq 0$ by

$$\begin{cases} I_u^{(n+1)}(\theta,z) = \\ \quad \sec\theta \int_0^z dz' \exp\left(\kappa_e(\theta)\sec\theta\,(z'-z)\right) S^{(n+1)}(\theta,z') + \\ \quad \exp\left(-\kappa_e(\theta)\sec\theta z\right) r_{12}(\theta)\sec\theta \int_0^d dz' \exp\left(-\kappa_e(\pi-\theta)\sec\theta z'\right) W^{(n+1)}(\theta,z') \\ \\ I_d^{(n+1)}(\theta,z) = \sec\theta \int_z^d dz' \exp\left(-\kappa_e(\pi-\theta)\sec\theta\,(z'-z)\right) W^{(n+1)}(\theta,z') \end{cases} \tag{6.13}$$

Note that Eqs. (6.9-6.13) are put in scalar forms that apply to both vertical and horizontal polarizations. These are following the assumption that κ_e and r_{12} are diagonal matrices. To reflect the vector nature of RTEs arising from volume scattering, we update the source term $\overline{S}$ and $\overline{W}$ polarimetrically,

$$\begin{cases} \overline{S}^{(n+1)}(\theta,z) = \\ \qquad \int_0^{\pi/2} d\theta' \overline{\overline{p}}(\theta,\theta') \cdot \overline{I}_u^{(n)}(\theta',z) + \int_0^{\pi/2} d\theta' \overline{\overline{p}}(\theta,\pi-\theta') \cdot \overline{I}_d^{(n)}(\theta',z) \\ \\ \overline{W}^{(n+1)}(\theta,z) = \\ \qquad \int_0^{\pi/2} d\theta' \overline{\overline{p}}(\pi-\theta,\theta') \cdot \overline{I}_u^{(n)}(\theta',z) + \int_0^{\pi/2} d\theta' \overline{\overline{p}}(\pi-\theta,\pi-\theta') \cdot \overline{I}_d^{(n)}(\theta',z) \end{cases} \tag{6.14}$$

Higher order intensities can be derived by substituting $\overline{I}^{(0)}$ into $\overline{I}^{(1)}$ and $\overline{I}^{(1)}$ into $\overline{I}^{(2)}$. The procedure can be extended to any order where $\overline{S}^{(n+1)}$ and $\overline{W}^{(n+1)}$ will be updated from $\overline{I}^{(n)}$. Finally, brightness temperature is obtained by summing up contributions from all orders as illustrated in Eq. (6.15). The process is repeated until

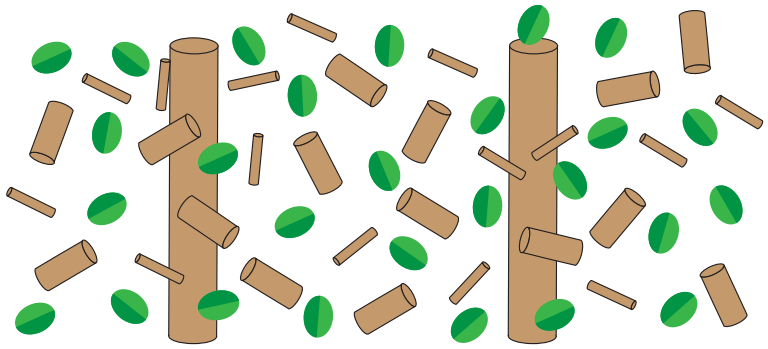

Figure 6.3: Radiative transfer theory assumes uniformly distributed discrete scatterers for a tree model.

the brightness temperature converges.

$$T_B = \frac{\sum_{n=0}^{\infty} I_u^{(n)}(z = d, \theta)}{C} \tag{6.15}$$

6.4 Model Implementation and Numerical Results

The present iterative RT method incorporates multiple scattering effects for a layer of random media with large optical thickness and scattering albedo. To illustrate the impact of the proposed new model on brightness temperature for vegetated area, a realistic simulation is set up. In support of investigations related to the SMAP mission, we considered an L-band radiometer with a land cover type of aspen trees. For the purpose of this simulation, the measured parameters acquired from SMAPVEX12 campaign is applied to the model. Trees are considered as discrete scatterers of tree trunks, primary branches, secondary branches, and leaves. In RTE the scatterers including trunks, branches, and leaves are assumed to be uniformly distributed in the 3D space as illustrated in Fig. 6.3.

The scattering coefficient, absorption coefficient, and extinction coefficient and

phase matrix are calculated using the infinite cylinder approximation (ICA) and thin disk approximation (TDA) assuming independent scattering and incoherent addition from multiple cylinders and disks. ICA is used for tree trunks, primary branches, and secondary branches and TDA is used for simulation of aspen leaves modeled with circular disks (*Tsang and Kong*, 2004). The vegetation parameters are given in Table 6.1.

Parameter	Value	Parameter	Value
Trunk Height	7.85 m	PB Volumetric Moisture	0.501
Trunk Diameter	15 cm	SB Length	55.5 cm
Trunk Density	$0.24/m^2$	SB Diameter	1.12 cm
Trunk Dielectric	25+7i	SB Density	143/tree
PB Length	1.41 m	SB Orientation	35°-90°
PB Diameter	2.88 cm	SB Volumetric Moisture	0.444
PB Density	13/tree	L density	1648/PB
PB Orientation	30°-90°	L Volumetric Moisture	0.58

Table 6.1: Vegetation parameters for medium aspen trees of forestry areas southwest of Winnipeg, Canada, based on measurements collected during SMAPVEX12 campaign. Trees are modeled with trunks, primary branches (PB), secondary branches (SB), and leaves (L). The leaves' thickness and radius are not reported in the SMAPVEX12, and are considered to be 1 mm and 2 cm, respectively.

The probability distribution function of the Eulerian angles α and β of the cylinder or disk axis is:

$$p(\alpha,\beta)=\begin{cases}\frac{1}{2\pi}\frac{1}{1-\cos\Delta\beta}, & \text{for } 0\le\beta\le\Delta\beta\\ \\ 0, & \text{otherwise}\end{cases} \tag{6.16}$$

where α and β are the orientation angles of the body axis of the cylinder and disk. α is the azimuthal direction and β is the elevation angle from the vertical direction ($+z$ axis). Equation (6.16) assumes the cylinders and disks are uniformly distributed in a specified range of elevation angles. In the following numerical examples, the ranges of the elevation angles $\Delta\beta$ for primary branches and secondary branches are reported in Table 6.1 based on the campaign's measurements and α is uniformly distributed from 0° to 360°. The tree trunks are assumed to be vertical, and the leaves are assumed to be uniformly distributed in all directions. The orientation average for the phase matrix and coefficients are taken as illustrated in (6.17) using the extinction coefficient as an example.

$$<\kappa_e>=\int_0^{2\pi}d\alpha\int_0^{\Delta\beta}\sin\beta d\beta p(\alpha,\beta)\kappa_e(\alpha,\beta) \tag{6.17}$$

The vegetation layer is characterized by its vegetation water content (VWC), which is related to the tree parameters as follows, considering trunks, branches, leaves:

$$\begin{aligned}VWC_{tree}=&VWC_{trunk}+VWC_{primary-branches}\\&+VWC_{secondary-branches}+VWC_{leaves}\end{aligned} \tag{6.18}$$

Equation (6.19) is the example of tree trunk's VWC. The VWC of each part of the tree is calculated similarly,

$$VWC_{trunk}=\rho_{water}\pi r_{trunk}^2 L_{trunk} m_{veg,trunk} N_A \tag{6.19}$$

where $\rho_{water} = 10^3$ kg/m^3 is the density of water. For $VWC = 15$ kg/m^2, which is reported in the SMAPVEX12 campaign for medium aspen trees, the calculated density is $N_A = 0.24$ trees/m^2. For simplicity, in the analysis, when we modify VWC, we do so by scaling N_A. A rough soil surface is assumed under the vegetation layer with rms height of 1 cm. In the following calculations, the microwave frequency is 1.41 GHz (L-band). The dielectric constant of tree is calculated using Ulaby et al (*Ulaby and El-Rayes*, 1987) and the dielectric constant of soil is calculated from the Mironov model (*Mironov et al.*, 2004) with soil moisture of 20% and clay fraction of 19%.

Figure 6.4 shows the absorption and scattering cross-sections per tree for the tree trunk, primary branches, secondary branches, and leaves for both vertical and horizontal polarizations as a function of incidence angle.

Results show that for the tree trunk, both scattering coefficients and absorption coefficients increase with the incidence angle, and the scattering coefficients exceed the absorption coefficient around 15° for the vertical polarization and 25° for the horizontal polarization. The scattering coefficients of the vertical polarization are in general larger than that for the horizontal polarization for a tree trunk.

In primary and secondary branches the orientation average is considered and results for horizontal polarization are larger than vertical. For leaves and secondary branches, the absorption coefficients are dominant over the scattering coefficients.

Numerical iterations up to fourth order are performed for passive radiative transfer equations. Figure 6.5a shows the brightness temperature up to fourth-order using multiple scattering model versus observation angle.

In Fig. 6.5b, the contributions from each order are shown. At 40°, contributions from zero-th up to second-order are significant with contribution percentages of 79%, 15.6%, and 3.8% for vertical polarization and 82.9%, 12.84%, and 3.2% for horizontal polarization, respectively. These results clearly show the importance of including

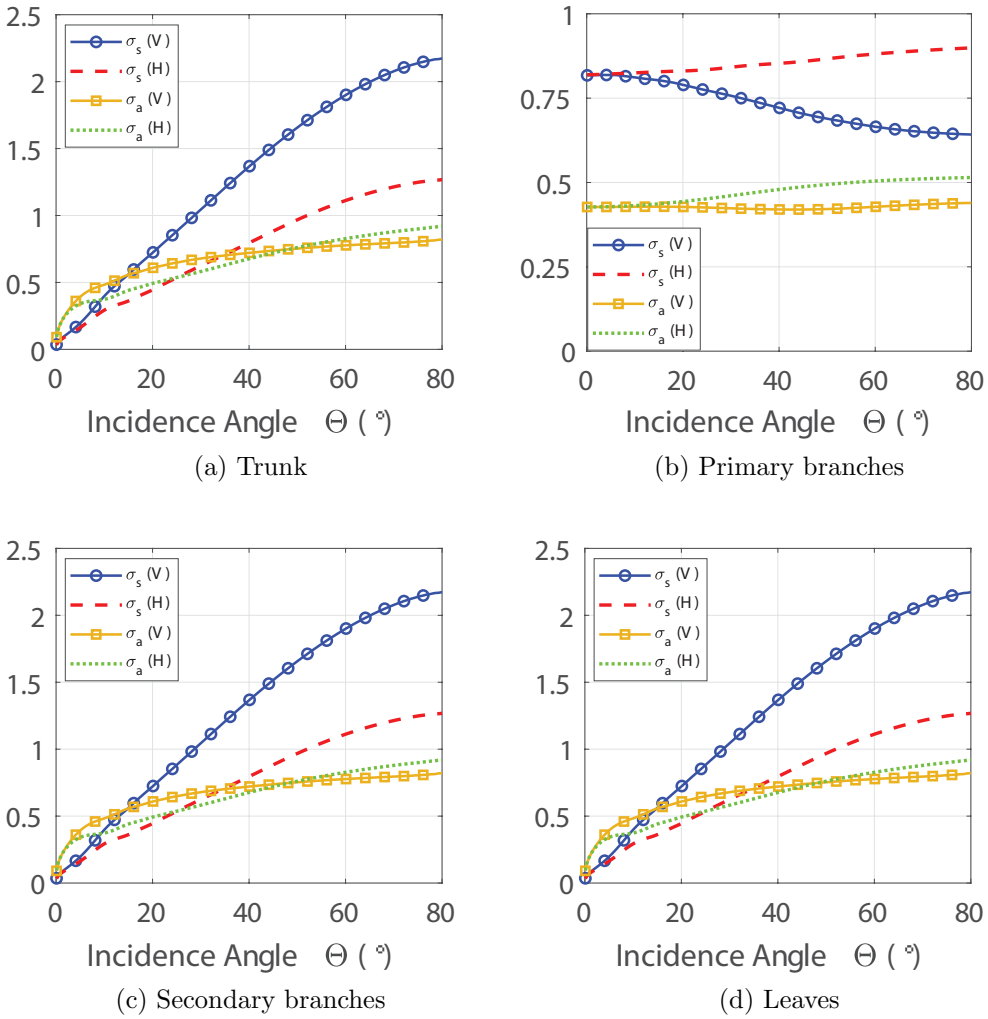

(a) Trunk

(b) Primary branches

(c) Secondary branches

(d) Leaves

Figure 6.4: Absorption and scattering cross sections per tree, in m^2/tree, of tree trunk, primary branches, secondary branches, and leaves with specifications of Table 6.1 as a function of the incident angle.

multiple scattering effects for large scattering albedo and optical thickness. These effects are less significant near nadir and grazing.

Figure 6.6 depicts the brightness temperature results for the 0-th order contribution which is the tau-omega model for both physical and empirical parameters, and results including contributions up to 4-th order using the proposed multiple scattering model.

When we calculate the tau and albedo using computed extinction and absorption coefficients, we call them physical parameters, while those that have been calculated using measurements and matched to the tau-omega model as empirical parameters.

Results of bare soil is also given for reference. It is shown that the tau-omega model based on physical parameters derived from the calculated extinction and absorption coefficient does not capture correctly either the value of brightness temperature nor the angular pattern of brightness temperature. The black dot shows the tau-omega model's result based on empirical parameters reported in the algorithm theoretical basis document (ATBD) of SMAP (*Neill et al.*, 31 August 2020). The empirical parameters are reported for deciduous broadleaf forests at 40°, which predicts higher brightness temperature than the tau-omega model based on physical parameters. The empirical parameters predict a lower value albedo, $\omega = 0.07$, which results in higher brightness temperature.

At 40°, the difference between the passive iterative RTE and the tau-omega model is more than 55.5 K for vertical polarization and 38 K for horizontal polarization, which confirms the importance of multiple scattering effects.

Figure 6.7 shows the brightness temperature as a function of soil moisture at 40° observation angle. Brightness temperature is calculated using both the passive iterative RT theory up to 4-th order and the tau-omega model for two cases of VWC of 15 kg/m^2 and VWC of 1 kg/m^2 for both polarizations.

The results for bare soil are also included for comparison. In general, scattering from the layer of vegetation decreases the sensitivity of brightness temperature to soil

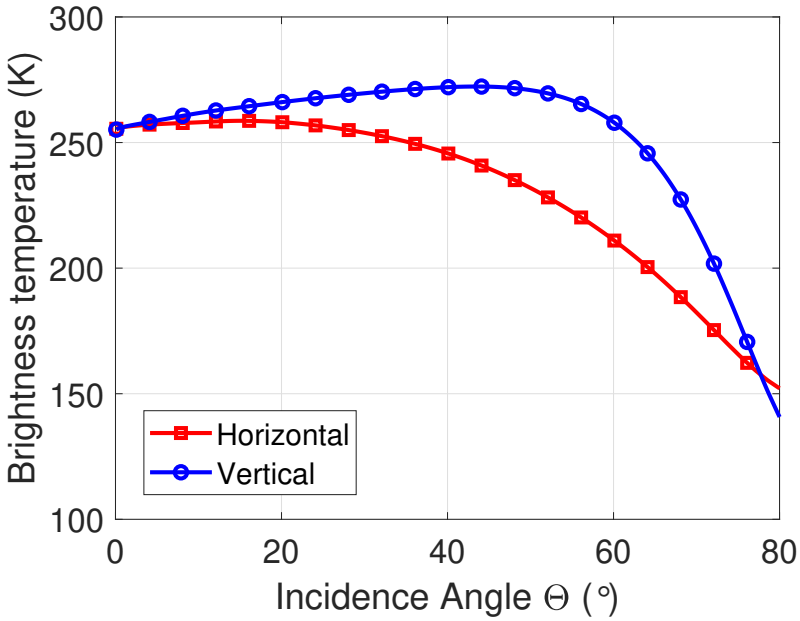

(a) Brightness temperature up to 4-th order.

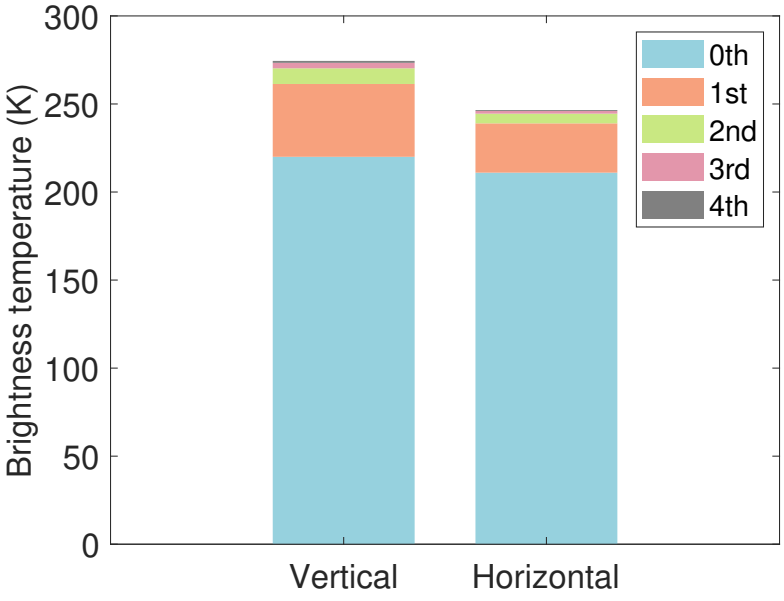

(b) Contribution of orders.

Figure 6.5: (a) The L-band brightness temperatures with multiple scattering model up to 4-th order versus observation angle, and (b) contribution from different orders to the brightness temperatures. The model is applied to the forest area with medium aspen trees with VWC of 15 kg/m^2, and density of 0.24 trees/m^2. The medium temperature is 300 Kelvin. The soil surface has rms height of 1 cm and moisture of 0.2 m^3/m^3.

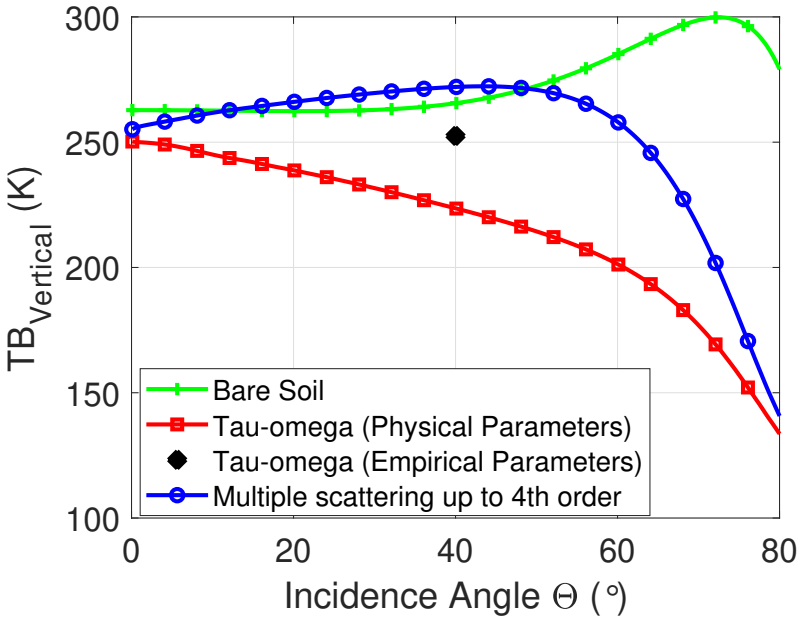

(a) Vertical polarization

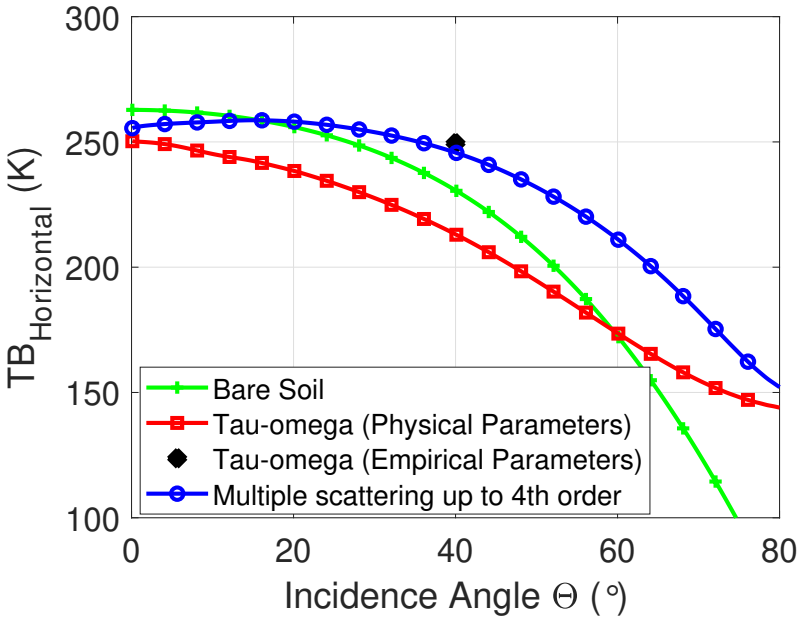

(b) Horizontal polarization

Figure 6.6: The brightness temperatures versus observation angles with up to 4-th order multiple scattering model, tau-omega model based on physical and empirical parameters, and the bare soil at L-band. The empirical parameters are derived from algorithm theoretical basis document (ATBD) of SMAP (*Neill et al.*, 31 August 2020). Medium aspen trees are considered with VWC of 15 kg/m^2, and density of 0.24 trees/m^2.The medium temperature is 300 Kelvin. The soil has an rms height of 1 cm and moisture of 0.2 m^3/m^3.

moisture.

The tau-omega model also predicts lower values of the brightness temperatures for thick vegetation layers like forests.

6.5 Model Evaluation With Experimental Data

To validate the proposed multiple scattering model, the results of calculated brightness temperature is compared with data acquired over a forest area during the SMAPVEX12 campaign.

6.5.1 SMAP Validation Experiment 2012 (SMAPVEX12)

SMAPVEX12 was located southwest of Winnipeg, MB, Canada, it took place between June 7 and July 19, 2012 and included airborne and field measurements (*McNairn et al.*, 2015).

The study area is characterized by changes in soil texture (changes in sand and clay percentages) and vegetation land cover, from crop with VWC of 0.25 kg/m^2 to large aspen trees with VWC of 25.6 kg/m^2.

The forested area of the experiment, which is the focus of this chapter, includes four sampling sites of F1, F2, F3, and F5 each with a varying degree of tree cover. The main tree species included aspen trees, bur oak, and balsam poplar on soil textures ranging from clay to loamy fine sand (*McNairn et al.*, 2015; *Colliander et al.*, 2015). For the purpose of the proposed model validation we used site F5 which contained medium aspen trees with a VWC of 14.102 kg/m^2. The structural parameters of these trees are given in Table 6.1 (*NASA Jet Propulsion Laboratory*, 2014; *McNairn and Wiseman*, 2014).

The soil texture varies across the site, producing significant spatial variability in moisture conditions over short distances. To capture this heterogeneity, there were 9 soil moisture sampling locations within each observation area. Soil moisture and

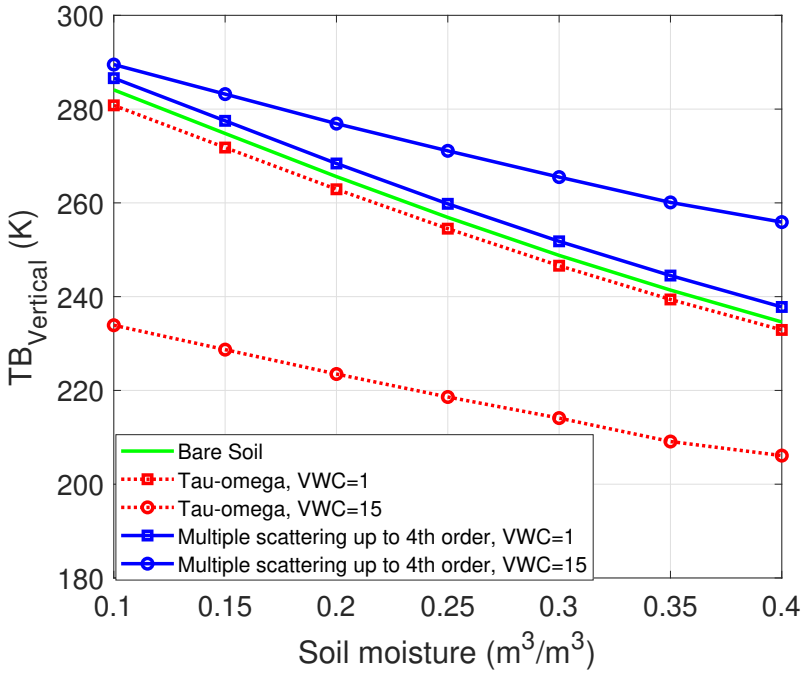

(a) Vertical polarization

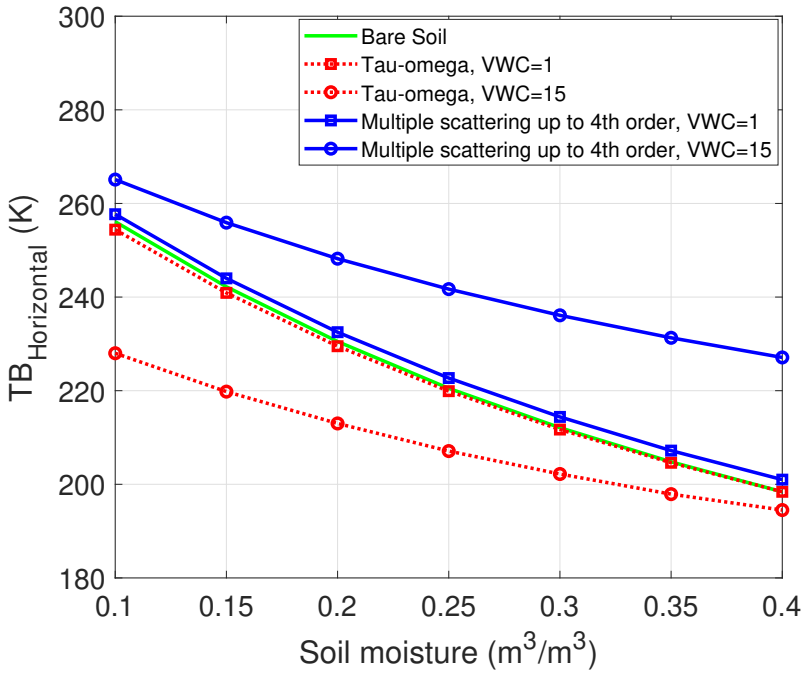

(b) Horizontal polarization

Figure 6.7: Brightness temperatures versus soil moisture with up to 4-th order multiple scattering model, tau-omega model, and for the bare soil case at 40° at L-band for VWC of 15 kg/m^2 and 1 kg/m^2, respectively. The soil has an rms height of 1 cm.

dielectric constant, measured with Stevens HydraProbes, soil temperature, and soil bulk density samples (i.e. sand, clay, and silt) have been reported for each of the 9 samples in each site during measurement days.

Passive and Active L-band Sensor (PALS), developed at the Jet Propulsion Laboratory, collected airborne data for the development of active and passive remote sensing techniques at L-band. The PALS instrument collects coincident radar and radiometer measurements in time and space.

The incidence angle of the instrument was fixed at 40° to match the observing angle of SMAP. Brightness temperature and backscatter measurements were obtained with PALS on measurement days with both low-altitude (1200 m) and high-altitude (2750 m) flights (*Wilson et al.*, 2001).

The model validation uses low-altitude measurements for higher spatial resolution of the F5 forestry area. The soil moisture and temperature of reported samples and measured brightness temperatures, using PALS instrument, of field F5 for each day of measurement, are averaged for the analysis. The range of averaged soil moisture, soil temperature, soil roughness for this field are 0.15-0.35 m^3/m^3, 286-296 K, and 0.776 cm respectively. In the multiple scattering model, the dielectric of the soil is calculated by the Mironov model using the reported soil texture properties.

Figure 6.8 shows the ground based measurements including soil moisture, temperature, tree's specifications, and airborne measurements of brightness temperature of 13th July 2012.

6.5.2 Model Validation

Figure 6.9 shows the comparison between the passive measurements and the simulated brightness temperatures in scatter plots. Blue square dots show the measurements of SMAPVEX12 for field F5 over eleven days and orange circular dots show the simulation results. For each day the measured soil temperatures, soil

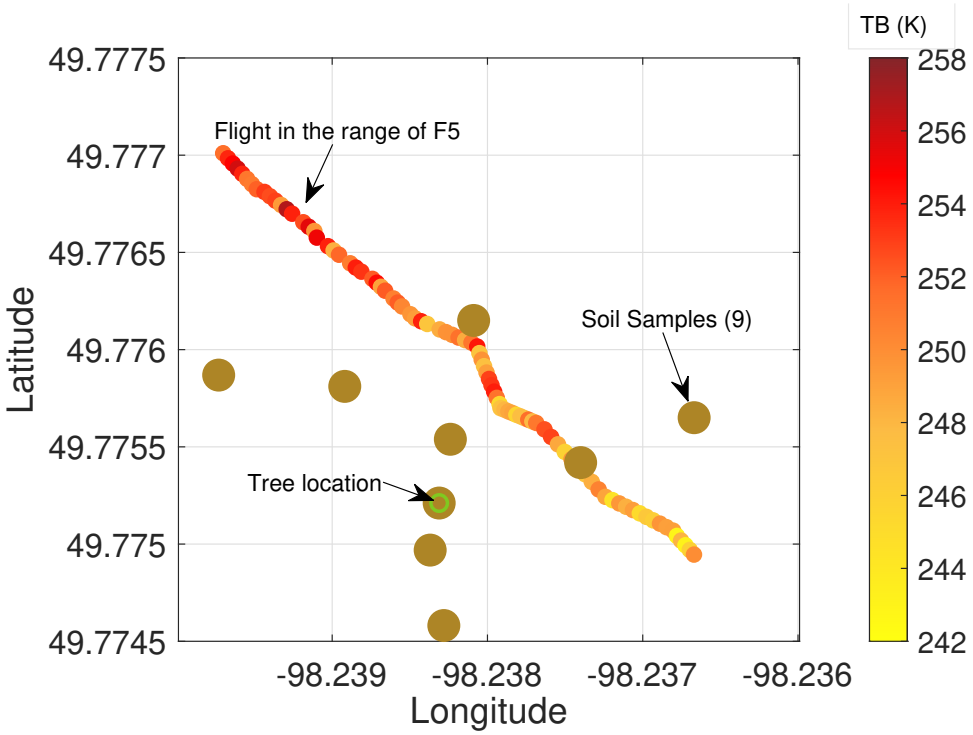

Figure 6.8: Ground based measurements and airborne measurements of the brightness temperature of 13th July 2012.

Date	mv	T_s	TB_v	TB_h
7/3/12	0.207	294.5	273.1	265.5
7/5/12	0.1703	294.4	273.2	264.35
7/10/12	0.179	294.7	273.75	262.3
7/13/12	0.1603	294.6	276.3	268.4
6/12/12	0.3065	288.2	259.85	248.75
6/15/12	0.2795	288.6	263.1	248.1
6/17/12	0.3453	290.5	259.7	249.6
6/22/12	0.337	287.3	263.86	253.68
6/23/12	0.283	287.9	263.68	254.7
6/25/12	0.315	287.2	265.6	261.3
6/27/12	0.302	292.6	270.37	261.2

Table 6.2: Averaged measured soil moisture (m^3/m^3), soil temperature (Kelvin), and brightness temperature (Kelvin) for each day of measurement during the SMAPVEX12 campaign in 2012.

moisture, and brightness temperatures are averaged.

We used these parameters, Table 6.2, and the tree parameters reported in Table 6.1 as the input for a 3-layered (soil-trees-air) multiple scattering model for which the results are shown as orange circular dots.

6.5.2.1 Passive Configuration

For vertical polarization, in Fig. 6.9 (a), the model and data match in low soil moisture conditions but when the soil moisture is increasing the model underestimates the data by 5-10 K. For horizontal polarization, in Fig. 6.9 (b), the model overestimate the data by 15-20 K. Figure 6.9 (c) and (d) show the scatter plot of the measured brightness temperature versus simulation results using the RT model. The root mean square error (RMSE) for the vertical and horizontal polarization is ≈5 K and ≈22 K, respectively.

Several studies in the literature addressed the effect of leaf litter by finding empirical parameters based on field measurements of forest leaf litter (*Grant et al.*, 2009; *Schwank et al.*, 2008; *Kurum et al.*, 2012), the radiative transfer model is used to derive the reflectivities using measured brightness temperature and effective permittivity approach is used to model the permittivity of the litter layer.

Figure 6.10 shows the measured area of the SMAPVEX12 campaign which indicates a layer of shrubs, leaves and dead leaves on the soil. There is some information about this layer in the reports. However it does not include many of the parameters required for the modeling. To show the effect of this layer we include a homogenous 3 cm layer of moist dead leaves above the soil to alter the effective reflectivity of the bottom boundary. For simplicity, flat interfaces with coherent interactions (*Tan et al.*, 2019; *Tan et al.*, 2015) is assumed.

The effective permittivity of this intermediate layer is approximated by Ulaby's model for leaves (*Ulaby and El-Rayes*, 1987). Figure. 6.11 shows the result of this

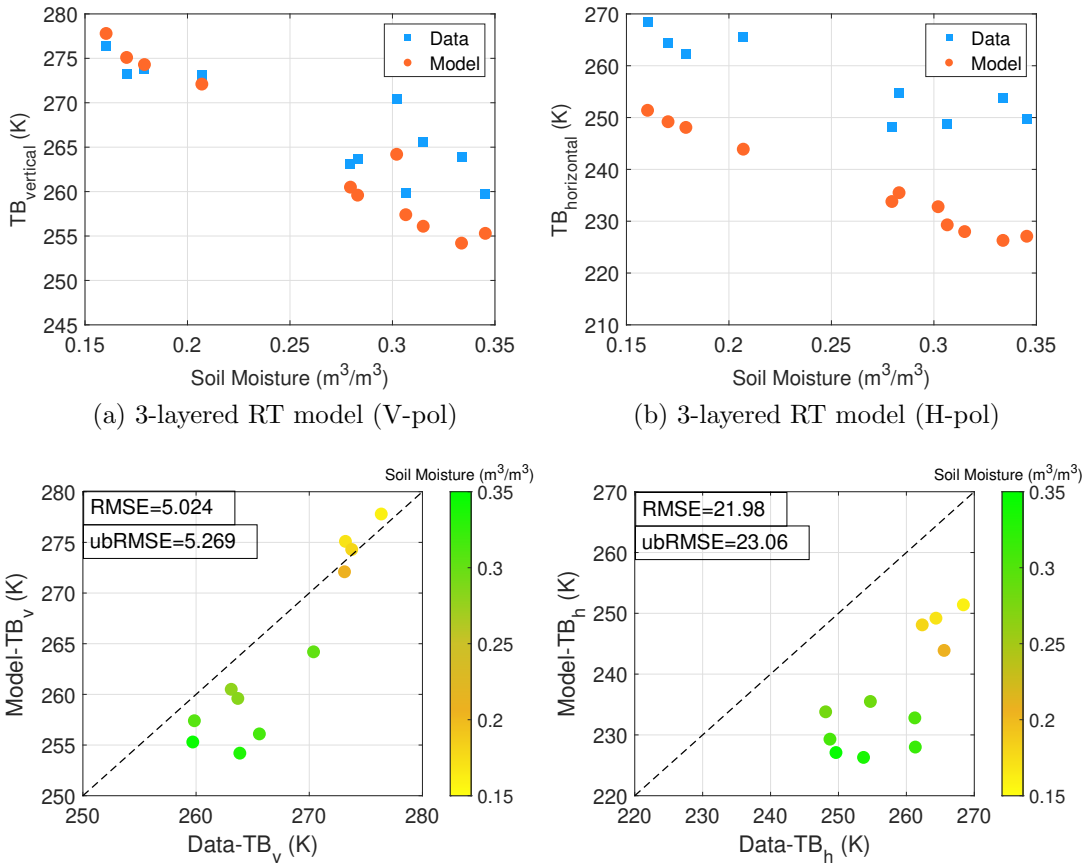

(a) 3-layered RT model (V-pol)

(b) 3-layered RT model (H-pol)

(c) 3-layered RT model (V-pol)

(d) 3-layered RT model (H-pol)

Figure 6.9: Model Validation for brightness temperature using SMAPVEX12 measured data for a forest field of medium aspen trees for vertical and horizontal polarizations. The vegetation parameters are given in Table 6.1.

Figure 6.10: Measurement fields of SMAPVEX12 campaign. Bottom boundary, soil, covered by a layer of shrubs, leaves and dead branches *NASA Jet Propulsion Laboratory* (2014).

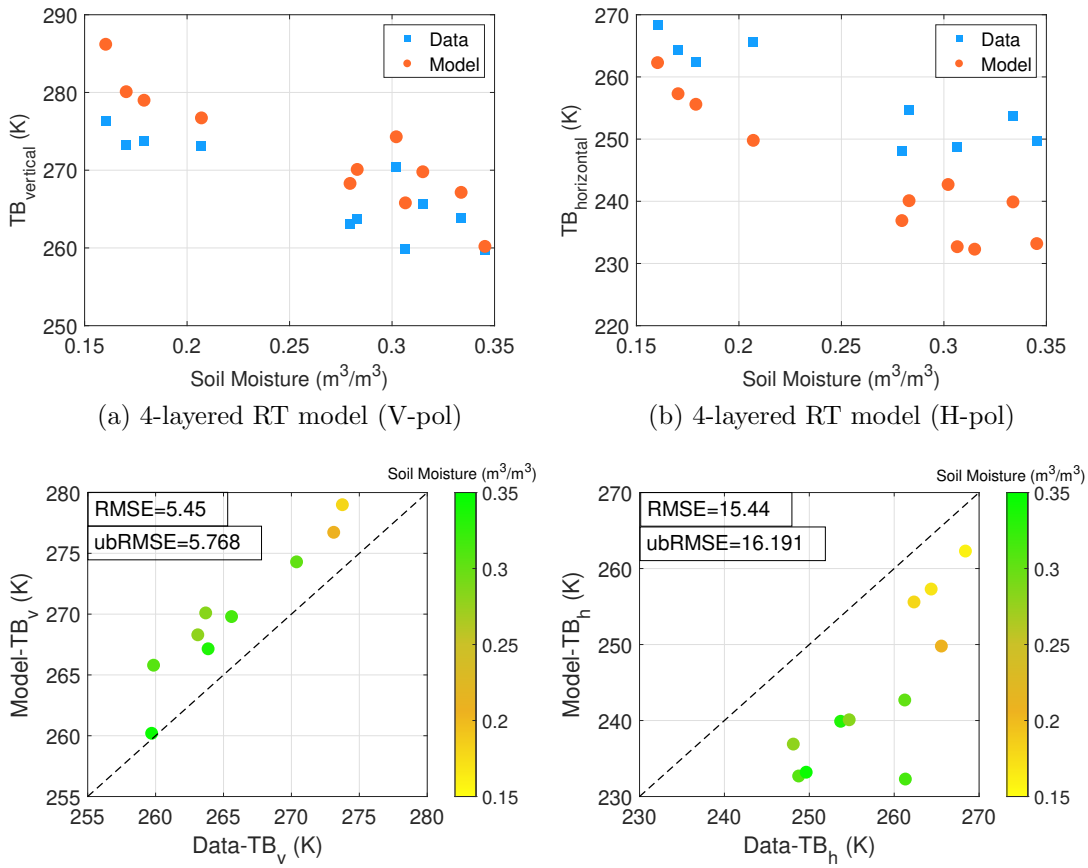

(a) 4-layered RT model (V-pol)

(b) 4-layered RT model (H-pol)

(c) 4-layered RT model (V-pol)

(d) 4-layered RT model (H-pol)

Figure 6.11: Model Validation for brightness temperature using SMAPVEX12 measured data for a forest field of medium aspen trees for vertical and horizontal polarizations. In this figure a layer of litter over the soil is considered. The vegetation parameters are given in Table 6.1.

4-layered model.

For H-pol only, it increases the brightness temperature and decreases the difference between model and data to less than 10 K, and the RMSE for horizontal polarization is 15 K, which shows the significance of considering the layer of shrubs and leaves over the bottom layer (soil).

Another simple approach to account for the effects of the litter over soil is to apply the Q-H model (*Wang and Choudhury*, 1981). The Q-H model computes the vegetation soil interface reflectivity $r_{(s,p)}$ from the reflectivities $r_{(0,p)}$ and $r_{(0,q)}$ of an

assumed flat interface as follows,

$$r_{s,p} = ((1-Q)r_{0,p} + Qr_{0,q}) \exp(-h\cos^2\theta) \tag{6.20}$$

where subscript p and q represent polarizations.

There are two empirical parameters, Q and h in the model: Q is the coupling coefficient representing polarization mixing due to the rough surface and volume scattering, and h is a dimensionless roughness, a function of frequency, polarization, geometric properties of the soil and surface height standard deviation. When $Q = 0$, the Q-H model reduces to the coherent reflectivity predicted by the Fresnel reflectivities. It is assumed that the volume scattering within the litter layer would introduce polarization coupling and increase the effective rms height.

The reported rms height in the SMAPVEX12 varies within 0.71-0.85 cm with an average of 0.776 cm. In the Q-H model results, as illustrated in Fig. 6.12, h is set as 1.2, and Q set as 0.14. The Q and h values for field F5 are assumed constants with time for all the 11 data points. The Q-H model reduces the reflectivity for horizontal polarization without affecting that for the vertical polarization much. This yields RMSEs of 6.67 K and 4.46 K in the brightness temperatures for the horizontal and vertical polarizations, respectively, as shown in Fig. 6.12 (c), (d), improving the overall agreement with data compared to the case when the litter layer effects are not considered.

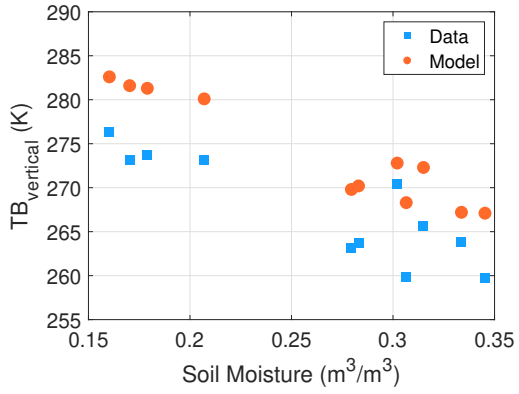

(a) 3-layered RT with Q-H roughness model (V-pol)

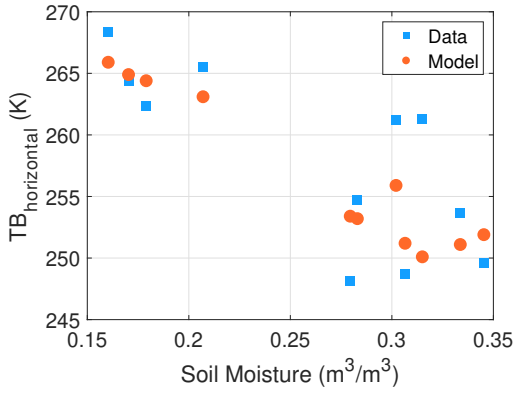

(b) 3-layered RT with Q-H roughness model (H-pol)

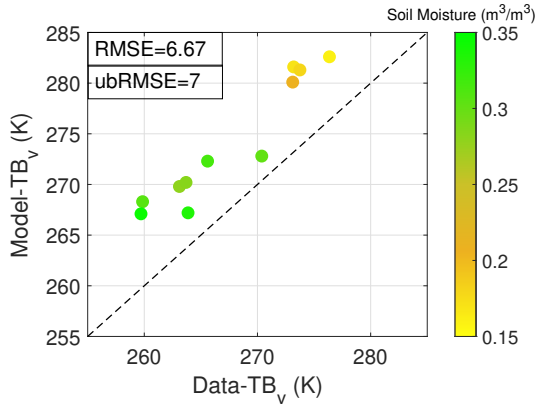

(c) 3-layered RT with Q-H roughness model (V-pol)

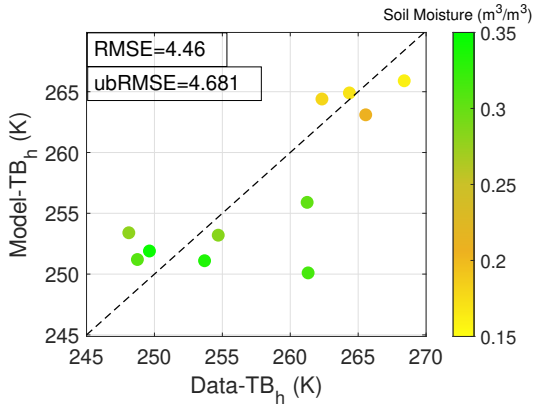

(d) 3-layered RT with Q-H roughness model (H-pol)

Figure 6.12: Model Validation for brightness temperature using SMAPVEX12 measured data for a forest field of medium aspen trees for vertical and horizontal polarizations. The Q-H roughness model is considered in this figure. The vegetation parameters are given in Table 6.1.

6.6 Conclusion

Effects of multiple scattering on a layer of trees on top of a reflective boundary is incorporated by solving the vector radiative transfer equations with an iterative method to high orders numerically. We used the iterative RTE method as a tool to study the angular dependence of brightness temperature and the sensitivity of brightness temperature to the soil moisture for different VWCs.

The multiple scattering solutions shows distinct features compared to the tau-omega model. For a layer comprised of predominant trees, increasing VWCs reduces more the sensitivity of brightness temperatures to soil moisture.

The applicability of the proposed physical model and tau-omega model is compared and summarized in Table 6.3.

The tau-omega model is a valid model only for small optical thicknesses. As the optical thickness become larger, this model becomes inaccurate physically due to the missing of multiple scattering effects.

The proposed framework, through solving RT equations iteratively and numerically, includes multiple scattering effects up to fourth order. The proposed method is applicable to both small and large VWCs and optical thicknesses.

To validate the iterative RT approach, the proposed model's results are compared with the data acquired in SMAPVEX12 campaign and results show relatively good agreement. The mismatch is attributed to the layer of litter over the soil and the tilt angle of tree trunks, neither of which are reported in the measurement campaign. Our results highlight the importance of the data related to these parameters. Hence, we predict that their inclusion can further enhance the accuracy the model.

Physical model	Small τ	large τ
Tau-omega (τ-ω)	✓	×
Passive multiple scattering RTE	✓	✓

Table 6.3: Comparison of the proposed passive iterative multiple scattering RTE method with existing model, for small and large optical thicknesses.

CHAPTER VII

Conclusion and Recommendations for Future Work

7.1 Research Summary

In this thesis, snowpack remote sensing using wideband novel radiometers and their challenges are considered. Microwave radiometry measures the microwave emission from a layer of snow and ice. Measurements at long wavelengths minimize volume and surface scattering effects within the snowpack. As a result, the thermal emission from a layer of snow can experience multiple reflections in the layer.

In particular, the thermal radiation emitted from the soil is split into two parts: one ray travels through the snow toward the radiometer's receiver which is named the direct ray, and another ray, reflecting from the top snow surface and then from the soil interface, is the delayed ray. Since the delayed ray is a copy of the direct ray, they coherently interfere with each other.

With sufficiently wide bandwidth, the radiometer can observe destructive and constructive interference as the radiometer frequency is varied, from which the microwave propagation time delay of the delayed ray relative to the direct ray can be obtained. This delay is primarily a function of the snow depth, with a smaller dependence on the SWE.

An instrument that can measure these features is exemplified by the $1.0-2.0$ GHz Wideband Autocorrelation Radiometer (WiBAR). However, there are some challenges that degrade WiBAR's ability to correctly measure the slab thickness.

The current WiBAR system is a frequency-domain system that suffers from a high data acquisition time. An alternative method is a time-domain mode which is introduced in this thesis.

The presence of narrowband radio frequency interference (RFI) signals is one of the challenges that ubiquitous in the WiBAR's frequency of operation (L-band). RFI increases the noise floor of the autocorrelation function and. A new comb filter is proposed to mitigate the present RFI in the measured spectrum.

A time-domain WiBAR instrument with a comb filter is set up on a bench to collect the data from a microwave scene simulator. A spectrum analyzer is used as a receiver and the data post-processed in both time-domain and frequency-domain to show the calibration and RFI mitigation using the new comb filter.

In addition, such wideband brightness temperature spectra can show oscillatory features that arise from coherent interference among the direct upward emission and its replicas from multiple reflections, are related to the layer thickness of snow, and can be affected by interface roughness or any above snow vegetation canopy.

Therefore, the effects of an above snow vegetation layer on brightness temperature spectra, particularly the possible decay of wave coherence arising from volume scattering in the vegetation canopy is analyzed using iterative radiative transfer equations.

Furthermore, a unified framework of vegetation scattering using radiative transfer (RT) theory for passive and active remote sensing of forest field, is presented. RT equations are solved by a numerical iterative approach for both passive and active configurations. This approach allows including higher order scattering, which represents multiple scattering. The method is applied to aspen trees in forest fields to compute the brightness temperatures and backscattering coefficients for passive and active

remote sensing configurations, respectively. The proposed model is validated with the passive and active L-band sensor (PALS) acquired in SMAPVEX12 measurements in 2012, which demonstrates the applicability of this model.

7.2 Contributions

In the following, the contributions made in this research are mentioned.

- We showed that RFI in wideband autocorrelation radiometry results in an increased noise in the observation.
- We designed and fabricated a new frequency tunable comb filter for RFI suppression.
- We enhanced the WiBAR instrument with the proposed comb filter and calibrated the WiBAR system with the comb filter.
- We proposed an alternate calibration of a WiBAR, TD-WiBAR, which enables more rapid data acquisition than the previous FD-WiBAR.
- We compared the performance of time-domain calibration with the frequency-domain calibration.
- We set up a WiBAR instrument with a scene simulator circuit in the laboratory in order to produce data to test the calibration algorithms.
- We demonstrated the RFI mitigation using the comb filter on a bench test and we showed that the comb filter can suppress the available RFI in the spectrum, and the peak of the autocorrelation function is detectable in the presence of a high power RFI signal.
- We conducted field measurements for snowpack remote sensing using WiBAR and UWBRad instruments, at the Keweenaw Research Center (KRC), in the

Michigan Tech University, in Calumet, MI for a particular time period during winter 2020 2021.

- We used the detected RFI flags by the UWBRad in the data post processing of WiBAR to clear the measured spectrum of the snow layer.
- We proposed a hybrid method to examine above-snow vegetation effects.
  - For the snow layer, a coherent model is proposed, and effective lower boundary conditions are derived for RTE.
  - For vegetation, an iterative RT solution incorporating multiple scattering is proposed.
- We showed the angular patterns of brightness temperature affected by above snow vegetation scattering and emission at L-band strongly.
- We proposed a uniform passive and active forward model of the iterative RTE solutions including the effect of multiple scattering to calculate the brightness temperature and back-scatter coefficient of the forest areas for radiometry and radar applications.
- We included the cyclical corrections for back-scattering enhancements in the active multiple scattering RTE model.
- We validated our proposed passive multiple scattering RTE model and active multiple scattering RTE with cyclical corrections, with the data acquired from PALS measurements in the SMAPVEX12 campaign for forestry areas.

7.3 Future Directions

We have discussed some of the challenges of snowpack remote sensing using wideband radiometers and proposed solutions to address these challenges. However,

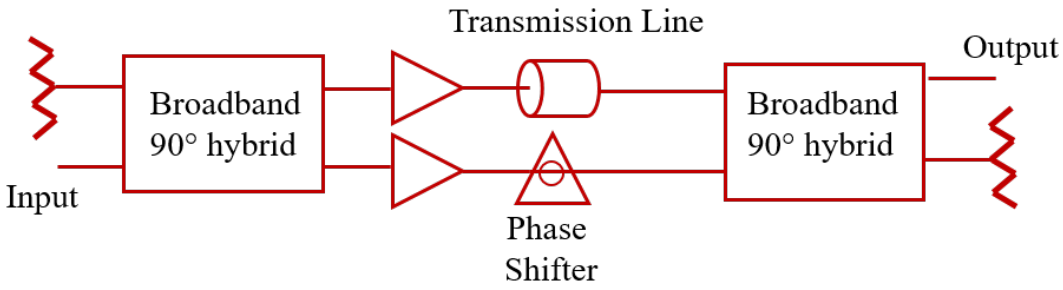

Figure 7.1: Schematic of the feed-forward comb filter.

there would be several directions that can be continued for further develop the concept. As such, below are some primary paths to further continue this work.

7.3.1 Feed Forward Comb Filter

An alternative architecture that could be used closer to the antenna in the front end of the WiBAR is a modification of the pseudo-correlation amplifier occasionally used in microwave radiometers (*Andrews et al.* (2018)). A block diagram is shown in Fig. 7.1, When the electrical lengths of the two paths are deliberately mismatched, but the amplitudes still matched, the transfer function exhibits nulls periodically in frequency, Fig. 7.2 shows the frequency response of the feed forward comb filter. With the phase shifter, the pattern of nulls can be tuned to frequencies of excessive RFI, as needed.

The feed-forward filter is good for nulling the single highest RFI frequency in the WiBAR frequency span. The feedback filter rejects much of the lower-level RFI that remains.

Because the feed-forward filter has wide passbands, the feedback filter has significant headroom for tuning. The electrical delay of the delay lines in the feed-forward filter should be made to match that in the feedback filter within the reciprocal of the frequency span of the WiBAR in order to avoid introducing apparent delays in the autocorrelation function where we expect target delays.

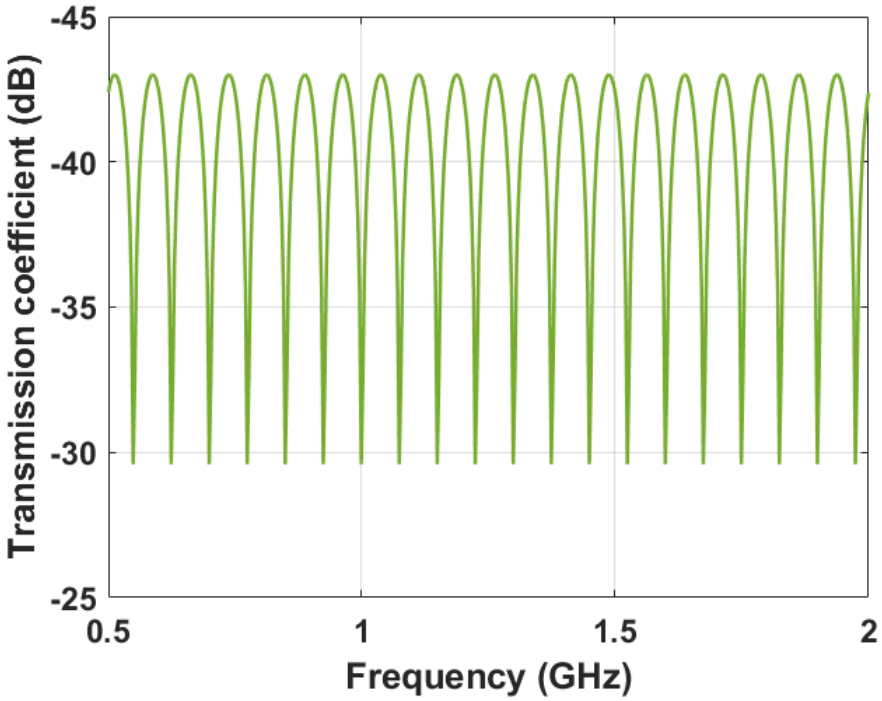

Figure 7.2: Frequency response of the ideal feed-forward filter.

7.3.2 Time-Domain WiBAR Receiver

In chapter III we demonstrated the TD-WiBAR calibration and RFI mitigation on a bench using an spectrum analyzer as the receiver. Next is replacing the spectrum analyzer with a digital back-end of the WiBAR radiometer that is the key to speeding up the WiBAR measurement relative to the use of a spectrum analyzer as the back-end.

The time domain receiver back-end is digitizing the input radiation signal at two closely spaced sampling frequencies. Two high-speed latching comparators convert the RF input into one-bit samples at two slightly different sampling rates.

A field-programmable gate array (FPGA) controls independent programmable clock delays to the analog to digital converters (ADC).

Two samples are collected with a time lag between them τ. These two samples are multiplied and the product is accumulated, yielding a measure of the ACF at

the time lag τ. As the time lag is varied, the real part of the complex ACF is built up. The imaginary part is reconstructed by applying a Hilbert transform to the real part (mirrored about zero lag to make a symmetric function of time), and the ACF is complete.

7.3.3 Image Resolution Enhancement of WiBAR

An unavoidable consequence of passive microwave observations from space is the large footprint. This will be especially true for WiBAR observations, where longer wavelengths are preferred to avoid the volume and surface scattering that reduce the coherence of the brightness.

The objective is to demonstrate the mapping/imaging of the thickness of a ice/snow layers with spatially varying thickness using a Wideband Autocorrelation Radiometer at a spatial resolution better than the footprint of the available WiBAR instrument.

The Backus-Gilbert algorithm (*Backus and Gilbert* (1970)) provides a method to trade absolute or relative amplitude precision for spatial precision. This algorithm, along with some others (*Olson et al.* (1986); *Lenti et al.* (2015); *Long and Daum* (1998)), has been very successful in remote sensing, particularly for the large footprints of the passive microwave sensors (*Stogryn* (1978); *Poe* (1990); *Long and Brodzik* (2015)). The Backus-Gilbert resampling scheme for traditional microwave radiometry is an appropriately weighted sum of brightness temperature observations in a region local of the desired location.

However, unlike single frequency observations that are disaggregated with algorithms like Backus-Gilbert, WiBAR observations are distinct in three ways:

- WiBAR observations are entire functions, not single data points. This distinction is important because the delay time of the Delayed Ray is linearly related to layer thickness. Thus, sub-pixel variance of layer thickness is embedded in the width of the delayed peak of the autocorrelation function (ACF). That

is, the observed width of the delayed peak should allow an estimate of the sub-pixel variance of layer thickness permitting useful snowpack information in more complex terrains than current satellite techniques.

- The high bandwidth of WiBAR observations permit rapid data acquisitions. The rapid acquisitions of large footprints means there are significant overlaps in a WiBAR image.

- WiBAR observations have inherent robustness against contamination by radio frequency interference (RFI). For traditional microwave radiometry, RFI is always additive, while for WiBAR, typically narrowband RFI merely affects the noise floor of the ACF from which the lag time, corresponding to a local maximum, is extracted.

The research will evaluate the potential for improved disaggregation of a WiBAR image compared to that for single frequency passive microwave observations, due to the very high rates of overlap of information that is more than a mere average value. In addition, the potential for improved disaggregation can be evaluated by combining global WiBAR observations with sub-global observations of snow depth at higher spatial resolution, such as could be provided by an orbiting InSAR or GNSS-R. Such sparse but high spatial resolution observations could serve as seeds or anchor points for an algorithm that disaggregates the WiBAR global coverage.

APPENDIX

APPENDIX A

Active Multiple Scattering of Forests Using Radiative Transfer Theory With an Iterative Approach and Cyclical Corrections

A.1 Introduction

For active remote sensing modeling, the distorted Born approximation (DBA) (*Lang and Sighu*, 1983) is frequently applied. DBA is used to calculate the backscattering coefficients at different polarizations considering the enhancement factor in the double bounce scattering mechanism. The double bounce backscattering for a single particle includes two paths where reflection by the underlying surface can take place after scattering from the particle or before that (*Chauhan et al.*, 1994).

Ulaby et al. (*Ulaby et al.*, 1990) proposed the first implementation of radiative transfer (RT) model for calaculation of polarimetric bistatic scatter from forest-covered terrain. In this model the trunk layer is modeled using a 2D RT to maintain the coherence of the long tree trunks in RT formulations. In (*Lin and Sarabandi*, 1999) the first fully coherent model for forest that accounts for the coherence effects of tree

structure is proposed. The model is capble of producing phase information needed for simulation of SAR interferometry. It is based on single scattering model in which very accurate scattering from individual elements are used (*Yi-Cheng Lin and Sarabandi*, 1995; *Polatin et al.*, 1995; *Sarabandi et al.*, 1993; *Sarabandi and Ulaby*, 1991; *Sarabandi and Senior*, 1990; *Sarabandi et al.*, 1988; *Senior et al.*, 1987).

In (*Kurum et al.*, 2011), a first-order backscattering model is proposed. However, DBA and these models ignore the effect of multiple scattering and only account for single scattering. As a result, this method is only valid for vegetations with small optical thickness such as wheat and canola fields. Ferrazzoli et al. (*Ferrazzoli and Guerriero*, 1995) include multiple scattering effects for calculating backscattering coefficients using the matrix-doubling method based on the active RT theory (*Twomey et al.*, 1966). However, this approach did not consider the backscattering enhancement factor for cyclical terms which also occurs in higher order volume scattering and in bounces from surface. In (*Liao et al.*, 2016; *Tan et al.*, 2015) both backscattering enhancement effects and multiple scattering effects are incorporated by solving the active RT equation through numerical iterations and identifying the cyclical terms for enhancement corrections. Here, we apply this iterative approach with backscattering enhancements under active configurations for calculating backscattering coefficients of tree trunks.

In this chapter the radiative transfer equations are solved by a numerical iterative approach for active configuration which includes multiple scattering of the vegetation and cyclical corrections. The numerical iterative approach predicts significantly different results compared to the distorted Born approximation.

The results of backscattering coefficients for VV and HH polarizations with enhancement factors are compared with DBA and RT results without enhancement, to show the effects of both multiple scattering and backscattering enhancement, respectively. Then the results are compared with the measured backscatter coefficient

during SMAPVEX12 campaign.

A.2 Combined Active and passive Model Using Distorted Born Approximation (DBA)

Combination of active and passive model is possible by relating emissivity to the bistatic scattering coefficient when the scene temperature is assumed homogeneous vertically. In this scenario, emissivity is one minus reflectivity, which can be computed from integration of the bistatic scattering coefficients over the upper hemisphere of solid angles (*Tsang and Kong*, 2004).

$$e_q = 1 - \frac{1}{4\pi} \int_0^{\pi/2} d\theta_s \sin\theta_s \int_0^{2\pi} d\phi_s \sum_{p=v,h} \gamma_{pq}(\theta_s, \phi_s; \theta_i, \phi_i)$$

(A.1)

where γ_{pq} is the bistatic scattering coefficient and 'p' and 'q' denote the polarizations of the scattered and incident waves, respectively. 'p' and 'q' can be either the vertical or horizontal polarization. In (*Huang et al.*, 2017), γ_{pq} is calculated using distorted Born approximation (DBA). In DBA, the total bistatic scattering coefficient is calculated as the sum of three scattering terms corresponding to the three scattering mechanisms of volume scattering (γ_{pq}^{vol}), double bounce scattering (γ_{pq}^{db}), and surface scattering (γ_{pq}^{surf}) as illustrated in Fig. A.1. The double bounce scattering contains two scattering terms. The first term, $\gamma_{pq}^{db,sr}$, is the scattering from a scatterer that is then reflected by the surface, and the second term, $\gamma_{pq}^{db,rs}$, corresponds to scattering of the reflected wave by a scatterer. For co-polarizations and in the backward scattering direction, these two terms are identical and in phase by nature, and thus the scattering fields add up

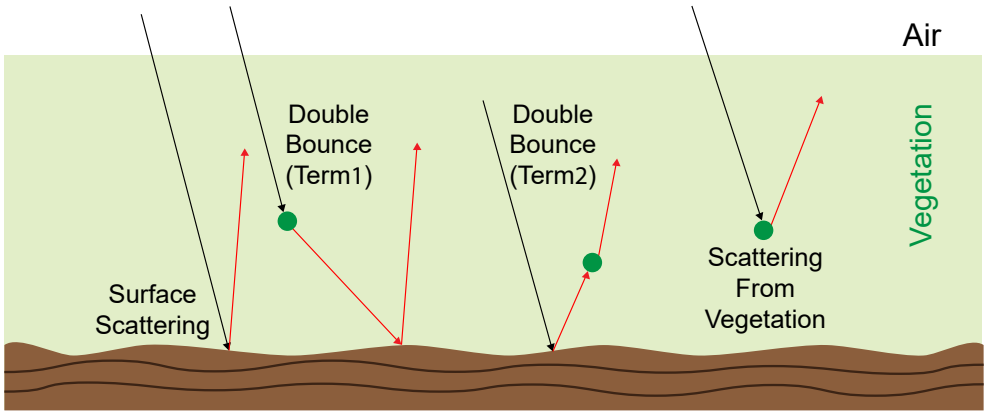

Figure A.1: Scattering mechanisms in DBA. It contains: surface scattering, double bounce scattering, and volume scattering.

coherently and constructively. The backscattering coefficient is:

$$\sigma_{pq}(\theta_{0i}, \phi_i) = \gamma_{pq}(\theta_{0i}, \phi_i + \pi, \theta_{0i}, \phi_i) \cos\theta_{0i} \tag{A.2}$$

The angle is related to the vegetation layer by Snell's law, $n_0 \sin\theta_{0i} = n_1 \sin\theta_i$ (*Tsang et al.*, 2007). Thus, the total backscattering is:

$$\sigma_{pp} = \sigma_{pp}^{vol} + 2 \times \sigma_{pp}^{db} + \sigma_{pp}^{surf} \tag{A.3}$$

with

$$\sigma_{pp}^{db} = \sigma_{pp}^{db,sr} + \sigma_{pp}^{db,rs} \tag{A.4}$$

In Eq. (A.3) the factor 2 before σ_{pp}^{db} accounts for the constructive coherent wave interference between the two double bounce scattering mechanisms. Such wave interference leads to backscattering enhancement in the first scattering order. Backscattering also occurs in cross-polarization but the relations are more complicated. Formulations to compute γ_{pq} in Eq. (A.2) is detailed in (*Huang et al.*, 2017).

Despite its wide usage, it is important to note that there are three important assumptions in the DBA that might not be valid:

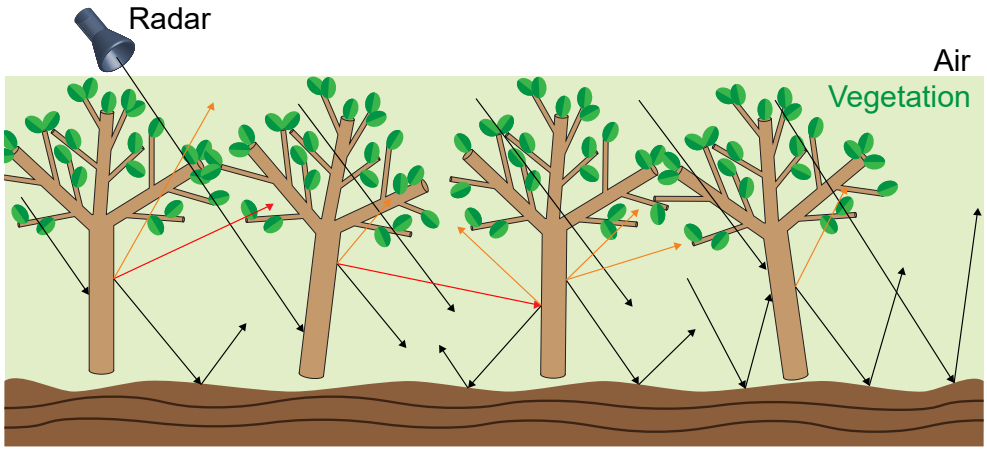

Figure A.2: Illustration of a vegetation layer above soil and the microwave scattering mechanism under active configuration.

1) Scatterers are uniformly distributed in the vegetation layer.

2) Only single scattering from vegetation is considered.

3) The position of the vegetation scatterer has no correlation with that of other scatterers.

Here, we try to address the second limitation by incorporating multiple scattering effects in the RT formulation.

A.3 Solution to Active RTE with multiple scattering and backscattering enhancement

In this section, we review the numerical iterative approach developed in (*Tsang and Ishimaru*, 1984, 1985), to solve the active RTE where iteration is numerically carried out to higher orders, and cyclical corrections are applied to all the cyclical terms to account for the backscattering enhancement effects in the co-polarization.

The zero-th order solution of upward and downward intensity for active RT equations is shown in Eq. (A.5) (*Tan et al.*, 2015).

$$\begin{cases} \overline{I}_u^{(0)}(z,\theta,\phi) = \overline{\overline{r}}_{12}\exp\left(-\overline{\overline{\kappa}}_e(z+d)\sec\theta\right)\overline{I}_0\delta(\cos\theta-\cos\theta_0)\delta(\phi-\phi_0) \\ \\ \overline{I}_d^{(0)}(z,\theta,\phi) = \exp\left(\overline{\overline{\kappa}}_e(z-d)\sec\theta\right)\overline{I}_0\delta(\cos\theta-\cos\theta_0)\delta(\phi-\phi_0) \end{cases} \tag{A.5}$$

For high orders, the n-th order solution relates to the $(n-1)$-th order solution recursively.

$$\begin{cases} \overline{I}_u^{(n+1)}(\theta,\phi,z) = \\ \quad \sec\theta\int_0^z dz' \exp\left(\overline{\overline{\kappa}}_e(\theta)\sec\theta\,(z'-z)\right)\overline{S}^{(n+1)}(\theta,\phi,z') + \\ \quad \exp\left(-\overline{\overline{\kappa}}_e(\theta)\sec\theta z\right)\overline{\overline{r}}_{12}(\theta)\sec\theta\int_0^d dz' \exp\left(-\overline{\overline{\kappa}}_e(\pi-\theta)\sec\theta z'\right)\overline{W}^{(n+1)}(\theta,\phi,z') \\ \\ \overline{I}_d^{(n+1)}(\theta,\phi,z) = \\ \quad \sec\theta\int_z^d dz' \exp\left(-\overline{\overline{\kappa}}_e(\pi-\theta)\sec\theta\,(z'-z)\right)\overline{W}^{(n+1)}(\theta,\phi,z') \end{cases} \tag{A.6}$$

where the source terms $\overline{S}^{(n)}$ and $\overline{W}^{(n)}$ can be updated from lower-order solution $\overline{I}^{(n-1)}$.

$$
\begin{cases}
\overline{S}^{(n+1)}(\theta,\phi,z) = \\
\quad \int_0^{\pi/2} d\theta' \int_0^{2\pi} d\phi' \overline{\overline{P}}(\theta,\phi,\theta',\phi') \cdot \overline{I}_u^{(n)}(\theta',\phi',z) + \\
\quad \int_0^{\pi/2} d\theta' \int_0^{2\pi} d\phi' \overline{\overline{P}}(\theta,\phi,\pi-\theta',\phi') \cdot \overline{I}_d^{(n)}(\theta',\phi',z) \\
\\
\overline{W}^{(n+1)}(\theta,\phi,z) = \\
\quad \int_0^{\pi/2} d\theta' \int_0^{2\pi} d\phi' \overline{\overline{P}}(\pi-\theta,\phi,\theta',\phi') \cdot \overline{I}_u^{(n)}(\theta',\phi',z) + \\
\quad \int_0^{\pi/2} d\theta' \int_0^{2\pi} d\phi' \overline{\overline{P}}(\pi-\theta,\phi,\pi-\theta',\phi') \cdot \overline{I}_d^{(n)}(\theta',\phi',z)
\end{cases}
\tag{A.7}
$$

Note that Eqs. (A.6, A.7) are in the same form as in Eqs. (6.13 and 6.14), respectively, except for the explicit ϕ-dependence.

The angular integrals in $\overline{S}^{(1)}(\theta,\phi,z)$ and $\overline{W}^{(1)}(\theta,\phi,z)$ are evaluated due to the Dirac delta functions in $\overline{I}^{(0)}$. Therefore, the expressions for the zero-th and first order solution can be derived explicitly (*Tan et al.*, 2015). For high orders, the intensity I is discretized along its three dimensions and computed numerically following Eqs. (A.6) and (A.7). This process is continued until the backscattering coefficient converges.

In (*Tan et al.*, 2015) the angular integrals in Eq. (A.6) are evaluated by Gaussian-Legendre quadrature for θ-integral and trapezoidal quadrature for ϕ-integral. The z-integrals in Eq. (A.7) are solved by the trapezoidal quadrature rule. Similar quadrature rules are adopted in solving the passive RTEs iteratively.

Distinct from the iterative solution of the passive RTE, where we directly sum up the contribution from one scattering order, in the active iterative solution, we need to keep track of contribution from each scattering mechanism. This is to facilitate the subsequent cyclical corrections to be applied to the cyclical terms. Such cyclical correction accounts for backscattering enhancement. Figure A.3 illustrates

the backscattering enhancement mechanism in double bounce scattering. The scattering by the particle can occur before the ground reflection or after the ground reflection. In conventional RT theory, the intensities of the two paths add up incoherently. This is not true in the backward scattering direction, where the two fields add up coherently, doubling the contribution from incoherent additions. Such cyclical corrections are included in the distorted Born approximation for the first order scattering, and the iterative approach extends such corrections to any higher orders. Of special interest is the explicit solution to Eq. (A.6) for first order scattering. With the cyclical correction as illustrated in Fig. A.3, this leads to the backscattering coefficient solution, in Eq. (A.8), where the first two terms represent volume scattering and double bounce scattering, respectively. This is in agreement with the results of DBA, as illustrated in Eq. (A.3).

$$
\begin{aligned}
&\sigma^{(1)}(\theta_0,\phi_0) \\
&\quad = 4\pi\cos\theta_0\{P(\theta_0,\pi+\phi_0;\pi-\theta_0,\phi_0)\tfrac{1-\exp(-2\kappa_e(\theta_0)d\sec\theta_0)}{2\kappa_e(\theta_0)} \\
&\quad +4r(\theta_0)P(\pi-\theta_0,\pi+\phi_0;\pi-\theta_0,\phi_0)d\sec\theta_0\exp(-2\kappa_e(\theta_0)d\sec\theta_0) \\
&\quad +r^2(\theta_0)P(\pi-\theta_0,\pi+\phi_0;\theta_0,\phi_0)\exp(-2\kappa_e(\theta_0)d\sec\theta_0)\tfrac{1-\exp(-2\kappa_e(\theta_0)d\sec\theta_0)}{2\kappa_e(\theta_0)}
\end{aligned}
\tag{A.8}
$$

The proposed iterative RT method with cyclical corrections applied for a layer of random media with large optical thickness and scattering albedo. The correction of contributions from cyclical terms allows us to consider the backscattering enhancement effects. To illustrate the impact of the proposed new model on radar backscattering cross-sections for the vegetated areas, a realistic simulation is set up. In support of investigations related to the SMAP mission, we considered an L-band radar at an incidence angle of 40 with a land cover type of aspen trees. For the purpose of this simulation, the measured parameters acquired from the SMAPVEX12 campaign, which are reported in Chapter VI, are applied to the model.

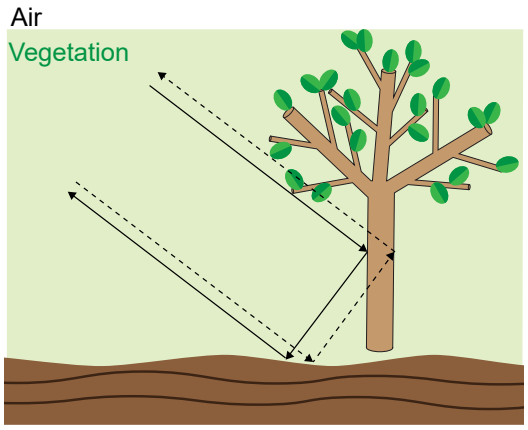

Figure A.3: Cyclical paths corresponding to double bounce scattering. In solid path reflection occurs after volume scattering, and in dashed path reflection occurs before volume scattering.

Next, the active iterative RT theory with backscattering enhancement corrections when applied to tree is investigated. To emphasize the effects of multiple scattering from vegetation, the surface scattering contributions in the backscattering results explicitly excluded. As the focus of this work is the effect of multiple scattering by the vegetation, general bistatic surface scattering is not considered.

To clearly depict the contribution to backscatter from different scattering orders and the effects of backscattering enhancements, in Fig. A.4, the accumulative contribution to backscatters in bar plots for both VV and HH polarizations, both with and without cyclical corrections is shown. The results are computed at L-band, at 40° incidence angle for VWC=15 kg/m^2 and soil moisture = 0.2 m^3/m^3. It is evident that the backscattering enhancement almost doubles the contribution from each scattering order. The HH backscatter is also shown to be stronger than the VV due to a smaller optical thickness and a larger surface reflectivity, which leads to larger contribution from bounces from the soil. The HH backscatter also seems to have faster convergence with respect to scattering orders compared to VV, consistent with a smaller optical thickness.

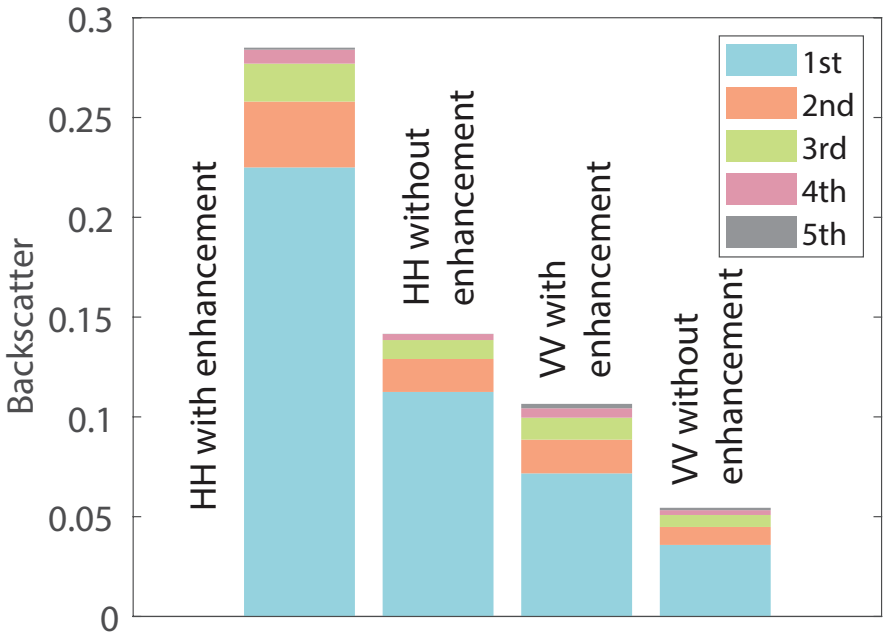

.4.1

Figure A.4: Backscatter contributions [m^2/m^2] up to 4th order for trees with VWC=15 kg/m^2 and density of 0.24 stems/m^2 with the soil moisture of 0.2 m^3/m^3 and roughness of 1 cm at L-band at 40°.

Figure A.5 compares the sensitivity of backscatter to soil moisture for different VWCs: one smaller VWC case of 1 kg/m^2, and one larger VWC case of 15 kg/m^2. The L-band backscatters are compared at 40° incidence angle.

For the smaller VWC case, the first order scattering results, i.e., the DBA results, are close to the multiple scattering results; while for the large VWC case, the DBA results underestimates the backscatter by about 1.6 and 0.65 dB, for VV and HH polarizations, respectively. Multiple scattering does not significantly affect the sensitivity of backscatter in dB scale to soil moisture, while increasing VWC from small to moderate ranges slightly reduces the sensitivity of backscatter to soil moisture by about 0.5 dB. The fact that the dominant double bounce alike terms decrease with VWC explains these.

A.4 Model Validation With SMAPVEX12 Data

To validate the proposed multiple scattering model, the results of calculated backscattering coefficient is compared with data acquired over a forest area during the SMAPVEX12 campaign.

Figure A.6 shows the ground based measurements including soil moisture, temperature, tree's specifications, and airborne measurements of Backscatter of 13nd July 2012.

We used the parameters, Table A.1, and the tree parameters reported in Chapter VI as the input for a 3-layered (soil-trees-air) multiple scattering model for which the results are shown as orange circular dots.

Figure A.7 shows the result of the comparison between measured backscatter coefficient in the SMAPVEX12 campaign and the model prediction for the same set of parameters reported in Table 6.1 and A.1. As it is shown in Fig. A.7 (c), (d) for the low values of soil moisture, the model overestimates the backscatter by 1 dB and 2.5 dB for vertical and horizontal polarization. By increasing the soil moisture the

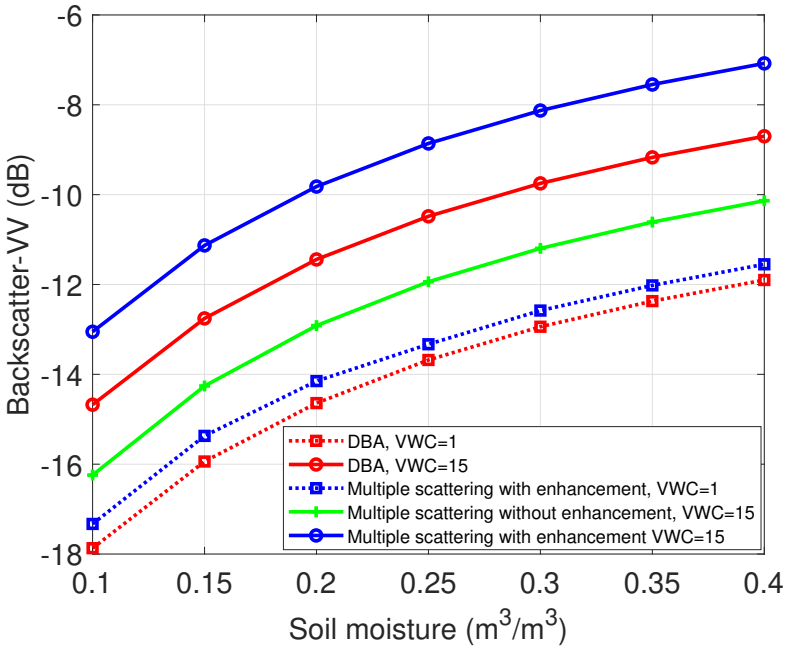

.5.1

(a) VV polarization

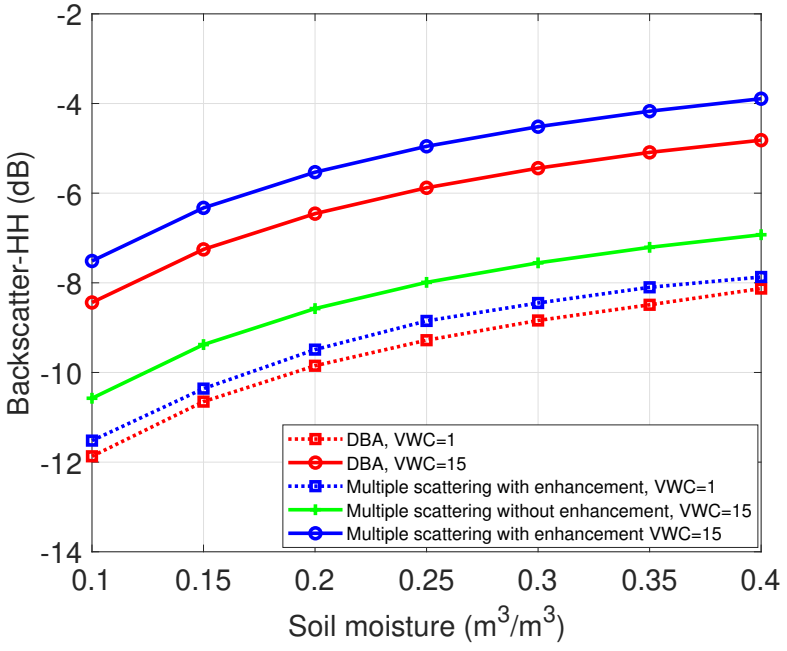

.5.2

(b) HH polarization

Figure A.5: Comparison of the L-band backscatter coefficients versus soil moisture, for DBA, active multiple scattering RTE without enhancement, and active multiple scattering RTE with enhancement for large and small VWCs at 40°.

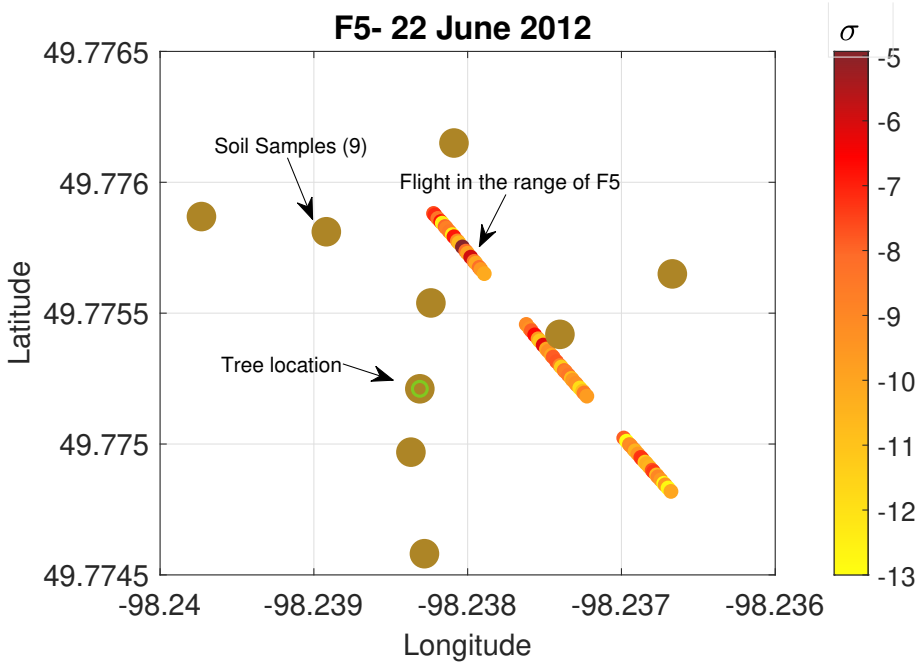

Figure A.6: Ground-based measurements and airborne measurements of the backscatter of 22nd June 2012.

Date	mv	T_s	σ^0_{VV}	σ^0_{HH}
7/3/12	0.207	294.5	-9.31	-9.704
7/5/12	0.1703	294.4	-9.413	-9.19
7/10/12	0.179	294.7	-9.65	-9.76
7/13/12	0.1603	294.6	-10	-9.47
6/12/12	0.3065	288.2	-8.63	-9.2
6/15/12	0.2795	288.6	-9	-8.85
6/17/12	0.3453	290.5	-8.45	-8.93
6/22/12	0.337	287.3	-8.73	-8.7
6/25/12	0.315	287.2	-8.73	-8.7
6/27/12	0.302	292.6	-9.53	-9.7

Table A.1: Averaged measured soil moisture (m^3/m^3), soil temperature (Kelvin), and backscatter coefficient (dB) for each day of measurement during the SMAPVEX12 campaign in 2012.

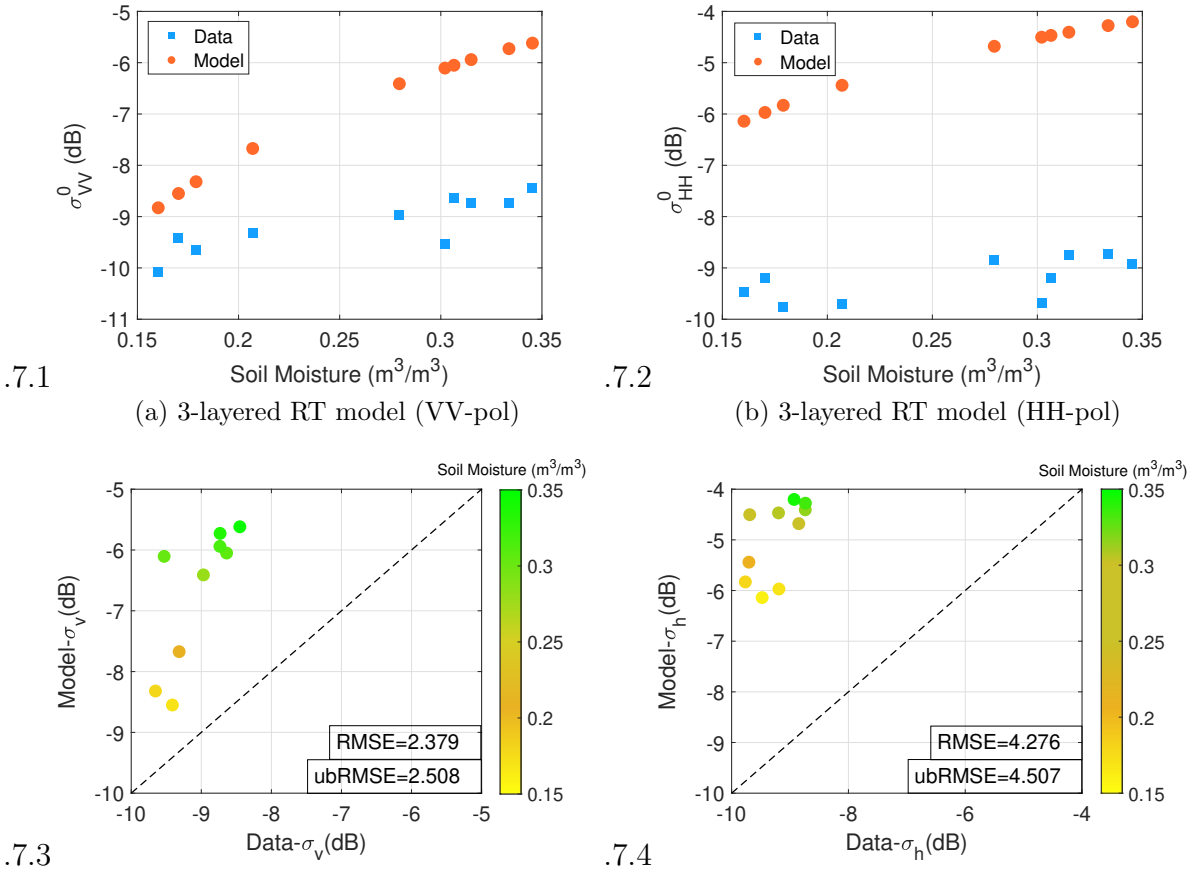

(a) 3-layered RT model (VV-pol)

(b) 3-layered RT model (HH-pol)

(c) 3-layered RT model (VV-pol)

(d) 3-layered RT model (HH-pol)

Figure A.7: Model Validation for backscatter coefficient using SMAPVEX12 measured data for a forest field of medium aspen trees for VV and HH polarizations. The vegetation parameters are given in Table 6.1.

mismatch is increasing by 2 dB and 4 dB for vertical and horizontal polarizations respectively.

The calculated RMSE, Fig. A.7 (c), (d), is 2.39 dB and 4.27 dB and by applying Q-H roughness model, it decreases to 0.832 dB and 1.6 dB, Fig. A.8 (c), (d), for vertical and horizontal polarizations respectively.

Nonetheless, even with a layer of leaf litter on the soil, the model exhibits greater dynamic range with respect to soil moisture than the measurements. A contributing factor to this may be the assumption of vertical tree trunks, which maximizes the first order ground-trunk interactions for a given set of geometric and moisture parameters.

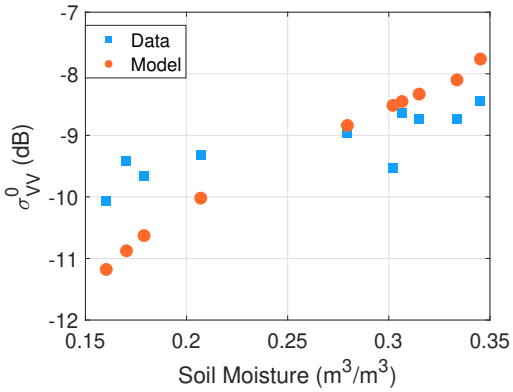

.8.1

(a) 3-layered RT with Q-H roughness model (V-pol)

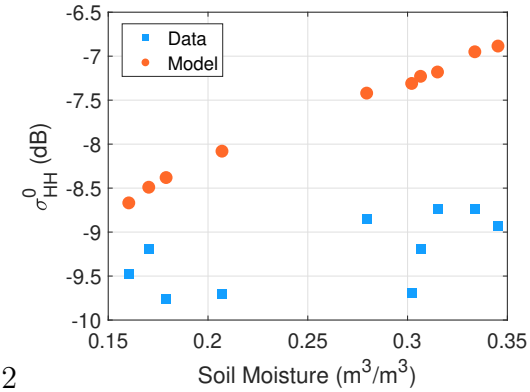

.8.2

(b) 3-layered RT with Q-H roughness model (H-pol)

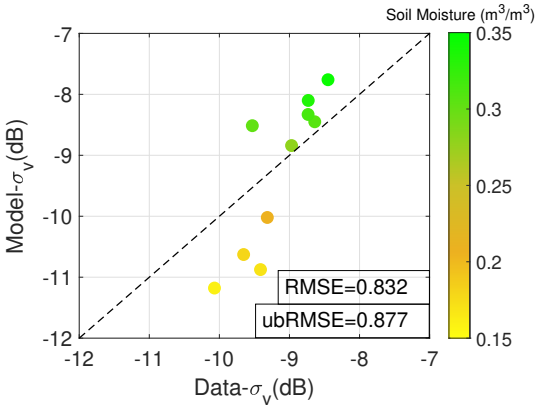

.8.3

(c) 3-layered RT with Q-H roughness model (V-pol)

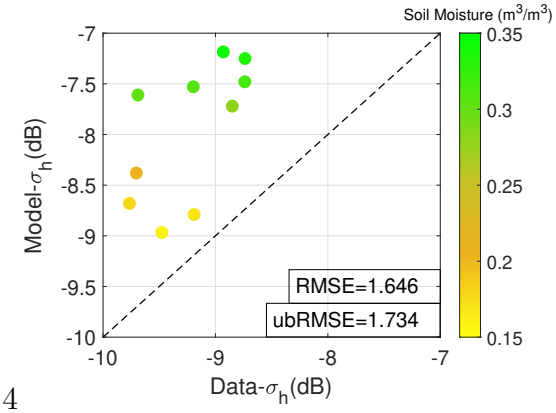

.8.4

(d) 3-layered RT with Q-H roughness model (H-pol)

Figure A.8: Model Validation for backscatter coefficient using SMAPVEX12 measured data for a forest field of medium aspen trees for vertical and horizontal polarizations. In this figure a layer of litter over the soil is considered. The Q-H roughness model is considered in this figure. The vegetation parameters are given in Table 6.1.

The trunks are not perfectly vertical, as can be seen in Fig. 6.10.

A.5 Conclusion

Effects of multiple scattering and backscattering enhancement on a layer of trees on top of a reflective boundary are incorporated by solving the vector radiative transfer equations with an iterative method to high orders numerically.

The multiple scattering solutions shows distinct features compared to the DBA. Cyclical corrections leading to backscattering enhancement are critical in solving active radiative transfer equations. The applicability of different physical models is compared and summarized in Table A.2.

The distorted Born approximation is a valid model only for small optical thicknesses. As the optical thickness become larger, DBA is inaccurate physically due to the missing of multiple scattering effects.

The active RT model without cyclical corrections is also invalid due to the lack of backscattering enhancement. The proposed framework, through solving RT equations iteratively and numerically, includes multiple scattering effects up to fourth order and backscattering enhancement effects by doubling contributions from the cyclical corrections. The proposed method is applicable to both small and large VWCs and optical thicknesses.

To validate the iterative RT approach, the proposed model's results are compared with the data acquired in SMAPVEX12 campaign and results show relatively good agreement. The mismatch is attributed to the layer of litter over the soil and the tilt angle of tree trunks, neither of which are reported in the measurement campaign. Our results highlight the importance of the data related to these parameters. Hence, we predict that their inclusion can further enhance the accuracy the model.

Physical model	Small τ	large τ
Distorted born approximation (DBA)	✓	×
Active multiple scattering RTE without enhancement	×	×
Active multiple scattering RTE with enhancement	✓	✓

Table A.2: Comparison of the proposed active iterative multiple scattering RTE method with existing models, for small and large optical thicknesses.

BIBLIOGRAPHY

BIBLIOGRAPHY

Akbar, R., and M. Moghaddam (2015), A combined active–passive soil moisture estimation algorithm with adaptive regularization in support of SMAP, *IEEE Transactions on Geoscience and Remote Sensing*, *53*(6), 3312–3324, doi:10.1109/TGRS.2014.2373972.

Andrews, M. J., et al. (2018), The ultrawideband software-defined microwave radiometer: Instrument description and initial campaign results, *IEEE Transactions on Geoscience and Remote Sensing*, *56*(10), 5923–5935, doi:10.1109/TGRS.2018.2828604.

Backus, G., and F. Gilbert (1970), Uniqueness in the inversion of inaccurate gross earth data, *Philosophical Transactions of the Royal Society of London. Series A, Mathematical and Physical Sciences*, *266*(1173), 123–192.

Bindlish, R., T. Jackson, R. Sun, M. Cosh, S. Yueh, and S. Dinardo (2009), Combined passive and active microwave observations of soil moisture during CLASIC, *IEEE Geoscience and Remote Sensing Letters*, *6*(4), 644–648, doi:10.1109/LGRS.2009.2028441.

Bolten, J. D., V. Lakshmi, and E. G. Njoku (2003), Soil moisture retrieval using the passive/active L- and S-band radar/radiometer, *IEEE Transactions on Geoscience and Remote Sensing*, *41*(12), 2792–2801, doi:10.1109/TGRS.2003.815401.

Chauhan, N. S., D. M. Le Vine, and R. H. Lang (1994), Discrete scatter model for microwave radar and radiometer response to corn: comparison of theory and data, *IEEE Transactions on Geoscience and Remote Sensing*, *32*(2), 416–426, doi:10.1109/36.295056.

Cheng, C.-C., and G. M. Rebeiz (2012), A three-pole 1.2–2.6-GHz RF mems tunable notch filter with 40-dB rejection and bandwidth control, *IEEE Transactions on Microwave Theory and Techniques*, *60*(8), 2431–2438.

Coale, F. S. (1956), A traveling-wave directional filter, *IRE Transactions on Microwave Theory and Techniques*, *4*(4), 256–260, doi:10.1109/TMTT.1956.1125073.

Colliander, A., et al. (2015), Comparison of airborne Passive and Active L-band System (PALS) brightness temperature measurements to SMOS observations

during the SMAP Validation Experiment 2012 (SMAPVEX12), *IEEE Geoscience and Remote Sensing Letters*, *12*(4), 801–805, doi:10.1109/LGRS.2014.2362889.

De Roo, R. D., M. Salim, M. Andrews, J. T. Johnson, and K. Sarabandi (2020), Snowpack remote sensing using ultra-wideband software-defined radiometer (uwbrad) and the wideband autocorrelation radiometer (wibar), in *AGU Fall Meeting 2020*, AGU.

Dente, L., P. Ferrazzoli, Z. Su, R. van der Velde, and L. Guerriero (2014), Combined use of active and passive microwave satellite data to constrain a discrete scattering model, *Remote Sensing of Environment*, *155*, 222–238.

England, A. W. (2013), Wideband autocorrelation radiometric sensing of microwave travel time in snowpacks and planetary ice layers, *IEEE Transactions on Geoscience and Remote Sensing*, *51*(4), 2316–2326, doi:10.1109/TGRS.2012.2210284.

Entekhabi, D., et al. (2010), The Soil Moisture Active Passive (SMAP) mission, *Proceedings of the IEEE*, *98*(5), 704–716, doi:10.1109/JPROC.2010.2043918.

Evans, S. (1965), Dielectric properties of ice and snow–a review, *Journal of Glaciology*, *5*(42), 773–792.

Ferrazzoli, P., and L. Guerriero (1995), Radar sensitivity to tree geometry and woody volume: A model analysis, *IEEE Transactions on Geoscience and Remote Sensing*, *33*(2), 360–371.

Frater, R. H., and D. R. Williams (1981), An active "cold" noise source, *IEEE Transactions on Microwave Theory and Techniques*, *29*(4), 344–347, doi:10.1109/TMTT.1981.1130355.

Grant, J. P., A. A. Van de Griend, M. Schwank, and J. Wigneron (2009), Observations and modeling of a pine forest floor at L-band, *IEEE Transactions on Geoscience and Remote Sensing*, *47*(7), 2024–2034, doi:10.1109/TGRS.2008.2010252.

Guerriero, L., P. Ferrazzoli, C. Vittucci, R. Rahmoune, M. Aurizzi, and A. Mattioni (2016), L-band passive and active signatures of vegetated soil: Simulations with a unified model, *IEEE Journal of Selected Topics in Applied Earth Observations and Remote Sensing*, *9*(6), 2520–2531, doi:10.1109/JSTARS.2016.2570424.

Guneriussen, T., K. A. Hogda, H. Johnsen, and I. Lauknes (2001), InSAR for estimation of changes in snow water equivalent of dry snow, *IEEE Transactions on Geoscience and Remote Sensing*, *39*(10), 2101–2108, doi:10.1109/36.957273.

Huang, H., T.-H. Liao, L. Tsang, E. G. Njoku, A. Colliander, T. J. Jackson, M. S. Burgin, and S. Yueh (2017), Modelling and validation of combined active and passive microwave remote sensing of agricultural vegetation at L-band, *Progress In Electromagnetics Research*, *78*, 91–124.

Huang, H., L. Tsang, E. G. Njoku, A. Colliander, K. Ding, and T. Liao (2017), Hybrid method combining generalized T matrix of single objects and Foldy-Lax equations in NMM3D microwave scattering in vegetation, in *2017 Progress in Electromagnetics Research Symposium - Fall (PIERS - FALL)*, pp. 3016–3023, doi:10.1109/PIERS-FALL.2017.8293651.

Jackson, T., and T. Schmugge (1991), Vegetation effects on the microwave emission of soils, *Remote Sensing of Environment*, *36*(3), 203 – 212.

Johnson, J. T., et al. (2021), Microwave radiometry at frequencies from 500 to 1400 MHz: An emerging technology for Earth observations, *IEEE Journal of Selected Topics in Applied Earth Observations and Remote Sensing*.

Kachi, M., K. Naoki, M. Hori, and K. Imaoka (2013), AMSR2 validation results, in *IEEE International Geoscience and Remote Sensing Symposium (IGARSS '13)*, pp. 831–834, doi:10.1109/IGARSS.2013.6721287.

Karam, M. A. (1997), A physical model for microwave radiometry of vegetation, *IEEE Transactions on Geoscience and Remote Sensing*, *35*(4), 1045–1058.

Kerr, Y. H., et al. (2012), The SMOS soil moisture retrieval algorithm, *IEEE Transactions on Geoscience and Remote Sensing*, *50*(5), 1384–1403.

Kinar, N. J., and J. W. Pomeroy (2009), Automated determination of snow water equivalent by acoustic reflectometry, *IEEE Transactions on Geoscience and Remote Sensing*, *47*(9), 3161–3167, doi:10.1109/TGRS.2009.2019730.

Ko, C.-H., A. Tran, and G. M. Rebeiz (2015), Tunable 500–1200-MHz dual-band and wide bandwidth notch filters using RF transformers, *IEEE Transactions on Microwave Theory and Techniques*, *63*(6), 1854–1862.

Kokhanovsky, A., T. Aoki, A. Hachikubo, M. Hori, and E. Zege (2005), Reflective properties of natural snow: approximate asymptotic theory versus in situ measurements, *IEEE Transactions on Geoscience and Remote Sensing*, *43*(7), 1529–1535, doi:10.1109/TGRS.2005.848414.

Kurum, M., R. H. Lang, P. E. O'Neill, A. T. Joseph, T. J. Jackson, and M. H. Cosh (2011), A first-order radiative transfer model for microwave radiometry of forest canopies at L-band, *IEEE Transactions on Geoscience and Remote Sensing*, *49*(9), 3167–3179.

Kurum, M., P. E. O'Neill, R. H. Lang, M. H. Cosh, A. T. Joseph, and T. J. Jackson (2012), Impact of conifer forest litter on microwave emission at L-band, *IEEE Transactions on Geoscience and Remote Sensing*, *50*(4), 1071–1084, doi:10.1109/TGRS.2011.2166272.

Kurum, M., P. E. O'Neill, R. H. Lang, A. T. Joseph, M. H. Cosh, and T. J. Jackson (2012), Effective tree scattering and opacity at L-band, *Remote Sensing of Environment*, *118*, 1–9.

Lang, R. H., and J. S. Sighu (1983), Electromagnetic backscattering from a layer of vegetation: A discrete approach, *IEEE Transactions on Geoscience and Remote Sensing*, *GE-21*(1), 62–71, doi:10.1109/TGRS.1983.350531.

Leinss, S., A. Wiesmann, J. Lemmetyinen, and I. Hajnsek (2015), Snow water equivalent of dry snow measured by differential interferometry, *IEEE Journal of Selected Topics in Applied Earth Observations and Remote Sensing*, *8*(8), 3773–3790, doi:10.1109/JSTARS.2015.2432031.

Lenti, F., F. Nunziata, C. Estatico, and M. Migliaccio (2015), Analysis of reconstructions obtained solving ℓp-penalized minimization problems, *IEEE Transactions on Geoscience and Remote Sensing*, *53*(9), 4876–4886.

Liao, T., S. Kim, S. Tan, L. Tsang, C. Su, and T. J. Jackson (2016), Multiple scattering effects with cyclical correction in active remote sensing of vegetated surface using vector radiative transfer theory, *IEEE Journal of Selected Topics in Applied Earth Observations and Remote Sensing*, *9*(4), 1414–1429, doi:10.1109/JSTARS.2015.2505638.

Lin, Y.-C., and K. Sarabandi (1999), A Monte Carlo coherent scattering model for forest canopies using fractal-generated trees, *IEEE Transactions on Geoscience and Remote Sensing*, *37*(1), 440–451, doi:10.1109/36.739083.

Long, D. G., and M. J. Brodzik (2015), Optimum image formation for spaceborne microwave radiometer products, *IEEE Transactions on Geoscience and remote sensing*, *54*(5), 2763–2779.

Long, D. G., and D. L. Daum (1998), Spatial resolution enhancement of SSM/I data, *IEEE Transactions on Geoscience and Remote Sensing*, *36*(2), 407–417.

Mahapatra, D., and S. Mattoo (1986), Exact evaluation of the transmitted amplitude for a Fabry-Perot interferometer with surface defects, *Applied optics*, *25*(10), 1646–1649.

Matzler, C. (1996), Microwave permittivity of dry snow, *IEEE Transactions on Geoscience and Remote Sensing*, *34*(2), 573–581, doi:10.1109/36.485133.

McNairn, H., et al. (2015), The Soil Moisture Active Passive Validation Experiment 2012 (SMAPVEX12): Prelaunch calibration and validation of the SMAP soil moisture algorithms, *IEEE Transactions on Geoscience and Remote Sensing*, *53*(5), 2784–2801.

McNairn, J. P., H., and G. Wiseman (2014), SMAPVEX12 Soil Texture Map, Version 1, Boulder, Colorado USA. Nasa National Snow and Ice Data Center Distributed Active Archive Center, `https://doi.org/10.5067/5694JSVXBA3A`.

Milly, P., J. Betancourt, M. Falkenmark, R. M. Hirsch, Z. W. Kundzewicz, D. P. Lettenmaier, and R. J. Stouffer (2008), Stationarity is dead: Whither water management?, *Earth*, *4*, 20.

Mironov, V. L., M. C. Dobson, V. H. Kaupp, S. A. Komarov, and V. N. Kleshchenko (2004), Generalized refractive mixing dielectric model for moist soils, *IEEE Transactions on Geoscience and Remote Sensing*, *42*(4), 773–785, doi:10.1109/TGRS.2003.823288.

Monerris, A., T. Schmugge, and G. Jedlovec (2009), Soil moisture estimation using L-band radiometry, *Advances in Geoscience and Remote Sensing*.

Mousavi, S., R. De Roo, K. Sarabandi, A. England, and H. Nejati (2016a), Remote sensing using coherent multipath interference of wideband planck radiation, in *2016 IEEE International Symposium on Antennas and Propagation (APSURSI)*, pp. 2051–2052, doi:10.1109/APS.2016.7696732.

Mousavi, S., R. D. De Roo, K. Sarabandi, A. England, and H. Nejati (2016b), Dry snowpack and freshwater icepack remote sensing using wideband autocorrelation radiometry, in *2016 IEEE International Geoscience and Remote Sensing Symposium (IGARSS)*, pp. 5288–5291, doi:10.1109/IGARSS.2016.7730377.

Mousavi, S., R. D. De Roo, K. Sarabandi, A. W. England, S. Y. E. Wong, and H. Nejati (2018), Lake icepack and dry snowpack thickness measurement using wideband autocorrelation radiometry, *IEEE Transactions on Geoscience and Remote Sensing*, *56*(3), 1637–1651, doi:10.1109/TGRS.2017.2765924.

Mousavi, S., R. De Roo, K. Sarabandi, and A. W. England (2019), Wideband autocorrelation radiometry for lake icepack thickness measurement with dry snow cover, *IEEE Geoscience and Remote Sensing Letters*, *16*(10), 1526–1530, doi:10.1109/LGRS.2019.2905840.

NASA Jet Propulsion Laboratory (2014), SMAPVEX12 Validation Experiment 2012, `https://smapvex12.espaceweb.usherbrooke.ca/home.php`.

Neill, O., P. S. Chan, E. G. Njoku, T. Jackson, and R. Bindlish (31 August 2020), Algorithm Theoretical Basis Document (ATBD): L2 and L3 Radiometer Soil Moisture (Passive) Data Products, *SMAP Project, Rev. F*.

Nejati, H. (2014), Passive remote sensing of lake ice and snow using wideband autocorrelation radiometer (WiBAR), University of Michigan, Ph.D. thesis.

NISAR (2019), NASA-ISRO SAR (NISAR) mission science user's handbook, *Tech. rep.*, NASA Jet Propulsion Laboratory, Pasadena, CA.

Njoku, E. G., and D. Entekhabi (1996), Passive microwave remote sensing of soil moisture, *Journal of Hydrology*, *184*(1-2), 101–129.

Olson, W. S., C.-L. Yeh, J. A. Weinman, and R. T. Chin (1986), Resolution enhancement of multichannel microwave imagery from the Nimbus-7 SMMR for maritime rainfall analysis, *Journal of Atmospheric and Oceanic Technology*, *3*(3), 422–432.

Peltoniemi, J., S. Kaasalainen, J. Naranen, L. Matikainen, and J. Piironen (2005), Measurement of directional and spectral signatures of light reflectance by snow, *IEEE Transactions on Geoscience and Remote Sensing*, *43*(10), 2294–2304, doi:10.1109/TGRS.2005.855131.

Piepmeier, J. R., et al. (2014), Radio-frequency interference mitigation for the soil moisture active passive microwave radiometer, *IEEE Transactions on Geoscience and Remote Sensing*, *52*(1), 761–775, doi:10.1109/TGRS.2013.2281266.

Poe, G. A. (1990), Optimum interpolation of imaging microwave radiometer data, *IEEE Transactions on Geoscience and Remote Sensing*, *28*(5), 800–810.

Polatin, P. F., K. Sarabandi, and F. T. Ulaby (1995), Monte-Carlo simulation of electromagnetic scattering from a heterogeneous two-component medium, *IEEE Transactions on Antennas and Propagation*, *43*(10), 1048–1057, doi:10.1109/8.467640.

Psychogiou, D., R. Mao, and D. Peroulis (2015), Series-cascaded absorptive notch-filters for 4G-LTE radios, in *2015 IEEE Radio and Wireless Symposium (RWS)*, pp. 177–179, IEEE.

Salim, M., S. Tan, and L. Tsang (2019a), Multiple scattering solution of radiative transfer equations of active and passive configuration for forests applications, in *2019 IEEE International Conference on Computational Electromagnetics (ICCEM)*, pp. 1–3, doi:10.1109/COMPEM.2019.8779055.

Salim, M., S. Tan, and L. Tsang (2019b), Multiple scattering solution of passive radiative transfer equations applied to forests, in *2019 IEEE International Symposium on Antennas and Propagation and USNC-URSI Radio Science Meeting*, pp. 161–162, doi:10.1109/APUSNCURSINRSM.2019.8889202.

Salim, M., S. Mousavi, R. De Roo, and K. Sarabandi (2020a), Calibration of wideband autocorrelation radiometer with a comb filter for RFI mitigation, in *2020 IEEE International Symposium on Antennas and Propagation and North American Radio Science Meeting*, pp. 1269–1270, doi:10.1109/IEEECONF35879.2020.9329570.

Salim, M., S. Mousavi, R. De Roo, and K. Sarabandi (2020b), RFI mitigation using a new comb filter for wideband autocorrelation radiometry, in *IGARSS 2020 - 2020 IEEE International Geoscience and Remote Sensing Symposium*, pp. 6369–6372, doi:10.1109/IGARSS39084.2020.9323684.

Salim, M., S. Mousavi, L. V. Nieuwstadt, R. De Roo, and K. Sarabandi (2020), A novel frequency tunable RF comb filter, *IEEE Microwave and Wireless Components Letters*, *30*(12), 1133–1136, doi:10.1109/LMWC.2020.3031287.

Salim, M., S. Tan, R. De Roo, A. Colliander, and K. Sarabandi (2020), A Multiple Scattering Model of Brightness Temperatures for Soil Moisture Retrieval in Forests and Comparison with SMAPVEX12 Data, in *AGU Fall Meeting Abstracts*, vol. 2020, pp. H187–02.

Salim, M., S. Tan, R. D. De Roo, A. Colliander, and K. Sarabandi (2021), Passive and Active Multiple Scattering of Forests Using Radiative Transfer Theory With an Iterative Approach and Cyclical Corrections, *IEEE Transactions on Geoscience and Remote Sensing*.

Sanamzadeh, M., L. Tsang, J. T. Johnson, R. J. Burkholder, and S. Tan (2017), Scattering of electromagnetic waves from 3D multilayer random rough surfaces based on the second-order small perturbation method: energy conservation, reflectivity, and emissivity, *JOSA A*, *34*(3), 395–409.

Sarabandi, K., and T. B. A. Senior (1990), Low-frequency scattering from cylindrical structures at oblique incidence, *IEEE Transactions on Geoscience and Remote Sensing*, *28*(5), 879–885, doi:10.1109/36.58977.

Sarabandi, K., and F. T. Ulaby (1991), High frequency scattering from corrugated stratified cylinders, *IEEE transactions on antennas and propagation*, *39*(4), 512–520.

Sarabandi, K., T. B. Senior, and F. Ulaby (1988), Effect of curvature on the backscattering from a leaf, *Journal of Electromagnetic Waves and Applications*, *2*(7), 653–670.

Sarabandi, K., P. F. Polatin, and F. T. Ulaby (1993), Monte Carlo simulation of scattering from a layer of vertical cylinders, *IEEE Transactions on Antennas and Propagation*, *41*(4), 465–475, doi:10.1109/8.220978.

Schwank, M., M. Guglielmetti, C. Matzler, and H. Fluhler (2008), Testing a new model for the L-band radiation of moist leaf litter, *IEEE Transactions on Geoscience and Remote Sensing*, *46*(7), 1982–1994, doi:10.1109/TGRS.2008.916983.

Senior, T. B. A., K. Sarabandi, and F. T. Ulaby (1987), Measuring and modeling the backscattering cross section of a leaf, *Radio Science*, *22*(06), 1109–1116, doi:10.1029/RS022i006p01109.

Serreze, M., et al. (2000), Observational evidence of recent change in the northern high-latitude environment, *Climatic change*, *46*(1-2), 159–207.

Smith-Berry, G. (2020), W. l. Gore Associates, Inc, `https://www.gore.com/resources/technical-information-changes-insertion-loss-and-phase`.

Sorocki, J., I. Piekarz, S. Gruszczynski, and K. Wincza (2016), Cascaded loops directional filter with transmission zeroes for multiplexing applications, in *2016 21st International Conference on Microwave, Radar and Wireless Communications (MIKON)*, pp. 1–4, IEEE.

Stogryn, A. (1978), Estimates of brightness temperatures from scanning radiometer data, *IEEE Transactions on Antennas and Propagation*, *26*(5), 720–726.

Tan, S., W. Chang, L. Tsang, J. Lemmetyinen, and M. Proksch (2015), Modeling both active and passive microwave remote sensing of snow using Dense Media Radiative Transfer (DMRT) theory with multiple scattering and backscattering enhancement, *IEEE Journal of Selected Topics in Applied Earth Observations and Remote Sensing*, *8*(9), 4418–4430, doi:10.1109/JSTARS.2015.2469290.

Tan, S., M. Salim, L. Tsang, J. T. Johnson, and R. D. De Roo (2019), Above snow vegetation effects on wideband autocorrelation radiometry, in *IGARSS 2019 - 2019 IEEE International Geoscience and Remote Sensing Symposium*, pp. 4896–4899.

Tan, S., et al. (2015), Physical models of layered polar firn brightness temperatures from 0.5 to 2 GHz, *IEEE Journal of Selected Topics in Applied Earth Observations and Remote Sensing*, *8*(7), 3681–3691, doi:10.1109/JSTARS.2015.2403286.

Tang, C.-W., and W.-C. Chen (2015), A compact tunable notch filter with wide constant absolute bandwidth, *IEEE Microwave and Wireless Components Letters*, *25*(3), 151–153.

Tsang, L., and A. Ishimaru (1984), Backscattering enhancement of random discrete scatterers, *JOSA A*, *1*(8), 836–839.

Tsang, L., and A. Ishimaru (1985), Theory of backscattering enhancement of random discrete isotropic scatterers based on the summation of all ladder and cyclical terms, *JOSA A*, *2*(8), 1331–1338.

Tsang, L., and J. A. Kong (2004), *Scattering of Electromagnetic Waves: Advanced Topics*, vol. 26, John Wiley & Sons.

Tsang, L., J. A. Kong, and R. T. Shin (1985), *Theory of microwave remote sensing*, Wiley-Interscience, New York.

Tsang, L., J. A. Kong, and K.-H. Ding (2004), *Scattering of electromagnetic waves: theories and applications*, vol. 27, John Wiley & Sons.

Tsang, L., J. Pan, D. Liang, Z. Li, D. W. Cline, and Y. Tan (2007), Modeling active microwave remote sensing of snow using Dense Media Radiative Transfer (DMRT) theory with multiple-scattering effects, *IEEE Transactions on Geoscience and Remote Sensing*, *45*(4), 990–1004, doi:10.1109/TGRS.2006.888854.

Twomey, S., H. Jacobowitz, and H. Howell (1966), Matrix methods for multiple-scattering problems, *Journal of Atmospheric Sciences*, *23*(3), 289–298.

Ulaby, F. T., and M. A. El-Rayes (1987), Microwave dielectric spectrum of vegetation - part II: Dual-dispersion model, *IEEE Transactions on Geoscience and Remote Sensing*, *GE-25*(5), 550–557, doi:10.1109/TGRS.1987.289833.

Ulaby, F. T., K. Sarabandi, K. McDonald, M. Whitt, and M. C. Dobson (1990), Michigan microwave canopy scattering model, *International Journal of Remote Sensing*, *11*(7), 1223–1253.

Vail, E. C., M. S. Wu, G. S. Li, L. Eng, and C. J. Chang-Hasnain (1995), GaAs micromachined widely tunable Fabry-Perot filters, *Electronics Letters*, *31*(3), 228–229, doi:10.1049/el:19950102.

Waitt, R., T. C. Pierson, N. MacLeod, R. Janda, B. Voight, and R. Holcomb (1983), Eruption-triggered avalanche, flood, and lahar at Mount St. Helens—effects of winter snowpack, *Science*, *221*(4618), 1394–1397.

Walker, J. L. B. (1978), Exact and approximate synthesis of TEM-Mode transmission-type directional filters, *IEEE Transactions on Microwave Theory and Techniques*, *26*(3), 186–192, doi:10.1109/TMTT.1978.1129342.

Wang, J., and B. Choudhury (1981), Remote sensing of soil moisture content, over bare field at 1.4 GHz frequency, *Journal of Geophysical Research: Oceans*, *86*(C6), 5277–5282.

Wigneron, J.-P., et al. (2017), Modelling the passive microwave signature from land surfaces: A review of recent results and application to the L-band SMOS & SMAP soil moisture retrieval algorithms, *Remote Sensing of Environment*, *192*, 238–262.

Wilson, W. J., S. H. Yueh, S. J. Dinardo, S. L. Chazanoff, A. Kitiyakara, F. K. Li, and Y. Rahmat-Samii (2001), Passive Active L- and S-band (PALS) microwave sensor for ocean salinity and soil moisture measurements, *IEEE Transactions on Geoscience and Remote Sensing*, *39*(5), 1039–1048.

Wing, O. (1959), Cascade directional filter, *IRE Transactions on Microwave Theory and Techniques*, *7*(2), 197–201.

Yi-Cheng Lin, and K. Sarabandi (1995), Electromagnetic scattering model for a tree trunk above a tilted ground plane, *IEEE Transactions on Geoscience and Remote Sensing*, *33*(4), 1063–1070, doi:10.1109/36.406692.